Interactions Between Ultrashort Pulses and Laser-Produced Tin Plasmas

Ph.D. thesis, Vrije Universiteit Amsterdam, 2023
Interactions between ultrashort pulses and laser-produced tin plasmas
Tiago Pinheiro de Faria Pinto

ISBN 978-94-6419-979-6
An electronic version of this dissertation is available at: research.vu.nl

VRIJE UNIVERSITEIT

INTERACTIONS BETWEEN ULTRASHORT PULSES AND LASER-PRODUCED TIN PLASMAS

ACADEMISCH PROEFSCHRIFT

ter verkrijging van de graad van Doctor of Philosophy
aan de Vrije Universiteit Amsterdam,
op gezag van de rector magnificus
prof.dr. J.J.G. Geurts,
in het openbaar te verdedigen
ten overstaan van de promotiecommissie
van de Faculteit der Bètawetenschappen
op maandag 27 november 2023 om 11.45 uur
in een bijeenkomst van de universiteit,
De Boelelaan 1105

door

Tiago Pinheiro de Faria Pinto

geboren te Vila Nova de Famalicão, Portugal

promotoren:	dr. S.M. Witte
	prof.dr. K.S.E. Eikema
promotiecommissie:	dr. N. Bhattacharya
	dr.ir. J. Nejdl
	prof.dr. P.C.M Planken
	prof.dr. N.F. Shahidzadeh
	dr. O.O. Versolato

CONTENTS

1 INTRODUCTION

1.1 EUV PHOTOLITHOGRAPHY

Just as ages in the past have been named after revolutionary materials such as Stone, Bronze, and Iron, we are undeniably living in the Silicon age [1]. These names come not from simply discovering or smelting these new materials, but from their widespread adoption as part of new technologies that fundamentally changed the fabric of contemporary civilizations. Unless the reader is currently holding a paper book in their hands, the act of reading this thesis is made possible by microchips and semiconductor technology, as was the process of writing it, the work carried out in its pursuit, and even the many hours of leisure and procrastination in between.

All these were made possible by the shrinking of computers from room-sized machines to small devices that can be cheaply integrated into every aspect of modern life. This reduction was in turn made possible by the shrinking of the transistor, the building block of integrated circuits and microchips. This trend of smaller transistors packed increasingly densely onto chips was famously captured by Gordon Moore in 1965 and later revised in 1975, stating that the number of transistors in a microchip would double every 2 years [2, 3]. That prediction has held true for more than 50 years, with current transistors containing features as small as 7 nm.

Currently, the main process used for the mass production of microchips is photolithography. Photolithography is the process of using light as part of a photochemical process to write fine structures onto a semiconductor substrate, as illustrated in Fig. 1.1. By repeating a cycle of chemical development, etching, ion implantation, deposition, and exposure steps multiple times, complex 3D structures can be printed layer by layer [5].

During the exposure step, when light is used to transfer a pattern from a mask onto a photo-sensitive material, the smallest feature size that can be printed is called the critical dimension (CD), and can be written as:

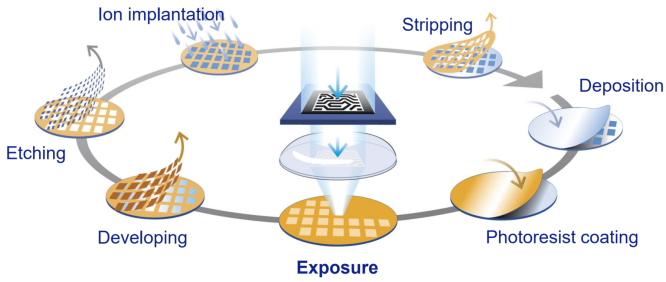

Figure 1.1: Overview of the main photolitographic processes involved in the production of semiconductor devices. Reproduced from [4].

$$\mathrm{CD} = k_1 \frac{\lambda}{\mathrm{NA}} \tag{1.1}$$

where k_1 is a constant determined by the characteristics of the lithography process used, λ is the wavelength of the light used, and NA is the numerical aperture of the exposure system.

Over the decades, the industry has followed a pattern of continuous improvements to increase the NA of the system and reduce k_1 through process optimization, interspaced with large leaps coming from the adoption of light sources with shorter wavelengths. Mercury arc lamps were the first light sources for photolithography, first at 436 nm and later at 365 nm. The industry then moved to excimer lasers producing 248 nm (KrF) and 193 nm (ArF), in the deep ultraviolet (DUV) [6]. The current generation of machines use 13.5 nm light, in the extreme ultraviolet (EUV) [7]. This large decrease in wavelength required a significant shift in how the light is produced.

A key factor in the choice of 13.5 nm was the availability of mirrors for wavelengths in the EUV range. Since most materials are opaque to EUV, high-NA lenses are not available, meaning the optical system between the EUV source and the lithography sample must be fully reflective. Currently, the state-of-the-art EUV mirrors are Mo/Si multilayer mirrors, with a reflectivity of 70% only within a narrow 2% bandwidth around 13.5 nm [8]. Since the optical system needed to deliver a high quality image of the plasma source onto the mask is composed of many mirrors (up to 10 in current machines), a 30% loss per mirror means only a small fraction of the EUV produced can be used for

lithography. Therefore, it was necessary to develop a source that could deliver significant EUV power, to compensate for the expected losses in the system.

Sources based on laser-produced plasmas (LPP) showed the most promise for delivering the necessary power [7, 9]. Tin was chosen as the LPP target material due to a strong emission peak at 13.5 nm coming from highly ionized Sn^{8+} to Sn^{14+} charge states [6, 10].

Several options for LPP sources were investigated, including solid tin targets and sprays or jets of liquid tin [9]. These configurations, however, presented issues with excessive tin debris ejected during laser-metal interaction or made it impossible for the laser to interact with all the tin injected in the chamber [11, 12]. This excess tin would then deposit on the inside of the machine, including the multilayer mirrors, reducing their reflectivity and operational lifetime. Microdroplet streams were found to be the best way to combat these issues by creating mass-limited targets. This setup consists of a stream of equally spaced droplets of liquid tin, each, ideally, contains just enough mass to be fully converted into plasma when irradiated by a high-energy laser pulse, maximizing the amount of EUV generated while minimizing the tin contamination in the system [13].

Inside current commercial EUV sources, microdroplets of liquid tin, with diameters of tens of μm, are irradiated by a high-power CO_2 laser [9, 13]. CO_2 lasers were chosen for their high-energy capabilities and proven industrial reliability, as well as the high conversion efficiencies (the in-band EUV power generated, as a percentage of input laser power) predicted by models [14] and observed experimentally [15–17]. This high conversion efficiency (CE) is mainly due to the long laser wavelength of 10.6 μm, which creates a plasma that is less opaque to 13.5 nm due to a lower electron and ion density, when compared to LPPs driven by lasers with shorter wavelengths such as 1064 nm Nd:YAG lasers [10, 18].

Initial microdroplet sources using single CO_2 laser pulses showed a CE of 1% [12]. Later, double-pulse schemes where proposed, with predicted CEs of up to 7% [14]. In this configuration, each droplet is irradiated by two laser pulses: a first low-energy pre-pulse irradiates the initially-spherical droplet, deforming it via hydrodynamic expansion into a more favorable shape; upon deformation, a time-delayed high-energy main pulse then irradiates this shaped droplet. As the CE is strongly dependent on the density distribution of the target, the process of shaping a spherical droplet into a more favorable shape is a topic of intense study.

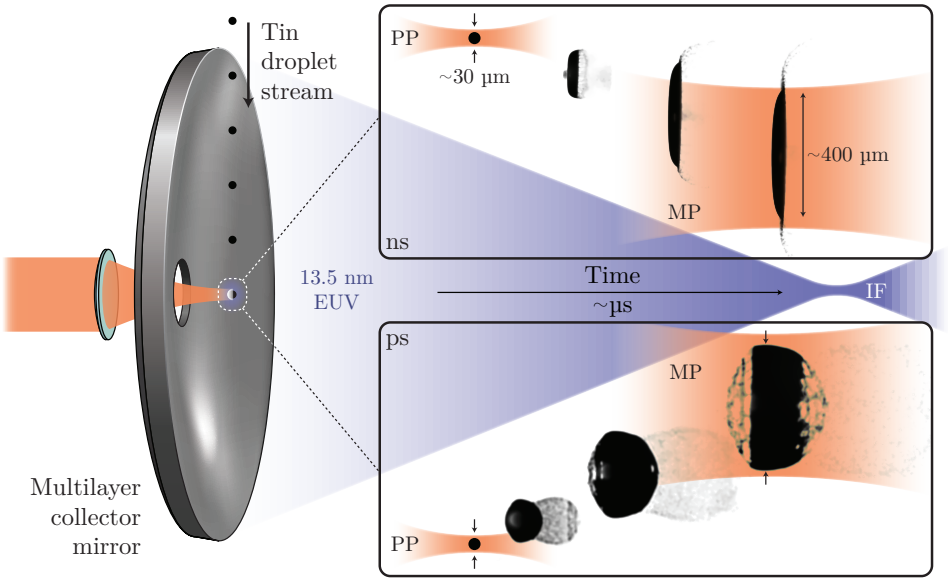

Figure 1.2: Schematic of the droplet-based EUV source operation principle. The collector mirror reflects the EUV emitted in a laser-facing hemisphere and focuses it at the intermediate focus (IF). The IF is then imaged by the illuminator onto the target sample. The top inset shows the temporal evolution of a droplet after irradiation by a pre-pulse with ns duration, resulting in a thin sheet target. The bottom inset shows the case of ps pre-pulse, resulting in a cloud target. Reproduced with permission from [19].

1.2 PRE-PULSE-DRIVEN DROPLET DYNAMICS

Fig. 1.2 shows an illustration of the droplet-based EUV source operation principle in a pre-pulse + main-pulse configuration, highlighting the different droplet expansion dynamics caused by pre-pulses with ps and ns durations.

Current EUV machines use pre-pulses with ns durations produced by the same 10.6 µm CO_2 laser as the main pulse [9, 20]. These long pre-pulses create a small amount of low density plasma on the laser-facing side of the target, giving rise to a pressure wave which deforms the target into a thin disk after a few microseconds [21–23].

While current double-pulse configurations which use a single CO_2 laser to generate both pulses are limited to pre-pulses longer than a few nanoseconds, a separate laser can be used to create the pre-pulses with picosecond and even

femtosecond durations. Pico- and sub-picosecond pulses create an intense shock wave at the laser-facing surface of the target. This shock wave propagates through the spherical droplet and focuses at its center, leading to a cavitation event, where a bubble forms which then collapses the droplet into a spherical shell. This shell then expands and breaks up, creating a so-called cloud target [12, 24]. Cloud targets have shown higher CE compared to disk targets, with the drawback of generating additional debris due to spallation [12, 24, 25].

1.3 ION EMISSION FROM LASER-PRODUCED PLASMAS

Along with the much desired EUV photons, there are many more particles emitted from plasma, namely: out-of-band photons, atomized tin neutrals, and tin ions. Ions, especially those of higher, keV-level energies, are problematic as they become implanted and damage the multi-layer mirror coatings. This leads to faster reflectivity degradation, resulting in increased machine downtime as the collector mirror needs to be maintained more often. There are various techniques that can mitigate the impact of ion debris, including using a buffer gas to stop or slow down the ions [26, 27], diverting the ions away from the collector mirror using a magnetic field [28], or a combination of both [29]. These approaches, however, are less effective for ions with kinetic energies above 1 keV, which are more likely to cause damage due to their high energy.

As discussed in the previous section, the characteristics of the pre-pulse greatly affect the expansion dynamics of the droplets, resulting in very different target shapes. The same can be said for the emitted ions, where we can expect large differences in the energies of ions emitted from plasmas created by ns pulses and ps/fs pulses, driven by different regimes in the ion acceleration in the plasma [30–32].

When the laser pulse interacts with target, energy is first transferred from the photons to the free electrons in the metal, and subsequently from the electrons to the lattice. Free-electron heating and thermalization occurs on electron-electron coupling timescales (few to tens of fs), while energy transfer from the electrons to the metal lattice occurs on electron-phonon coupling timescales (tens of ps) [32]. Nanosecond pulses have durations much longer than the timescales mentioned. As such, laser energy is still being transferred to the system after the ion emission is underway, with the majority of the ions interacting with a system that has reached a steady-state with a reasonable degree of thermalization. This results in a quasi-steady-state system, where ion energy is mostly determined by

hydrodynamics in the plasma [33, 34]. In the case of ps and fs pulses, which are comparable to or shorter than the electron-phonon coupling times, the system may not reach thermal equilibrium before the laser pulse ends. Therefore, a theoretical description of the resulting ion emission may become more complex.

While charge-state-resolved energy spectra of ions emitted by LPPs generated by ns laser pulses have been well studied [35–39], charge-state-resolved measurements of plasmas created by ultrashort laser pulses are not so well reported [40]. It is under debate whether steady-state approximations such as isothermal plasma expansion, which are valid for long ns pulses, will still be applicable for shorter pulses. These assumptions are often used to infer charge-state-specific energies from charge-state-insensitive results, such as those obtained with Faraday cups [41, 42]. Because of this, charge-state-resolved energy spectra (such as those presented in chapters 5 and 6) provide valuable information about the processes behind ion acceleration in LPPs that can be used to infer additional information from simpler measurement devices such as Faraday cups.

Taking this knowledge one step further, more complex laser irradiation schemes can be tailored with the specific purpose of controlling ion energy while producing a target shape favorable to EUV generation. The study presented in chapter 4 shows that the energy of ions emitted by a droplet-based LPP could possibly be reduced by a factor of up to 33, when the driving laser pulse is preceded by a weaker pulse with only a few percent of the energy of the driving pulse [43]. While those results were obtained with laser energies suitable for pre-pulses rather than main pulses, they show promise for the development of more sophisticated pre-pulse configurations, which could comprise tailored pulse sequences or temporally-shaped pulses [44], that could mitigate debris and ion issues while retaining the CE improvements of double-pulse configurations.

1.4 THESIS OUTLINE

In Chapter 2, we first discuss the two halves of the experimental setup that made this work possible: the laser systems responsible for creating the laser-produced plasmas, and the targets from which the plasmas are created. The laser source is a purpose-built system which delivers two beams with distinct characteristics: a 1064 nm Nd:YAG based system delivering pulses with durations between 15 and 100 ps in single pulse or pulse pair configuration, and an optical parametric chirped pulse amplifier (OPCPA) delivering pulses as short as 220 fs. Two different types of tin targets were used in this work: liquid tin microdroplets,

mirroring the commercial EUV nanolithography machines, and flat solid tin targets which, due to their simpler geometry, are a good comparison to many theoretical works on plasma expansion into vacuum.

In Chapter 3, we investigate the effects of pulse duration and polarization on the expansion of tin microdroplets illuminated by sub-ps laser pulses. Ultrashort pulses produce violent shockwave-driven cavitation and spallation dynamics in the droplet, compared to the plasma-push-driven deformations induced by ns pulses. We also show how utilizing linearly polarized pulses to break cylindrical symmetry results in new asymmetric target shapes which are in good agreement with smoothed-particle hydrodynamics simulations.

In Chapter 4, we show how using pulse pairs rather than single laser pulses to create LPPs from tin microdroplets results in a significant reduction of the energy of the emitted ions. Using pulse pairs rather than single pulses to deform the droplets results in a variety of novel target shapes, depending on the delay between the laser pulses and their energy ratio. For some parameters, cloud targets similar to those produced by a single ps pulse can be obtained, while still reducing the energy of the emitted ions.

In Chapter 5, we utilize an electrostatic analyzer to investigate the effects of laser pulse duration and energy on the ions emitted by LPPs created by fs pulses. The trends reported differ from the more often studied ns-driven LPPs, highlighting the limits of the traditional picture where the energy distribution of the ejected ions is dominated by the acceleration they experience in the electrostatic field created by the electrons ejected after laser irradiation.

Lastly, Chapter 6 builds on the work from the two prior chapters to paint a more complete charge-state-resolved picture of the ion energy reduction created by laser pulse pairs.

2

LASER SYSTEMS AND EXPERIMENTAL SETUPS FOR LASER-PRODUCED PLASMA STUDIES

We present an optical parametric chirped pulse amplifier (OPCPA) delivering 10.5 mJ pulses with durations down to 220 fs, at 100 Hz repetition rate, centered at 1550 nm. The system is pumped by a picosecond Nd:YAG amplifier at 1064 nm based on quasi-continuous-wave diode pumping, and seeded by a femtosecond mode-locked Er fiber laser at 1550 nm. This choice of wavelengths enables the use of well established technology and optical components for both pump and signal beams, resulting in a straightforward and robust system design and the ability for further power scaling to be used in high energy laser-produced plasma experiments.

We also describe the two target chambers used for the experiments presented in this thesis. The first is equipped with a microdroplet generator which produces a stream of liquid tin droplets, representative of the configuration used in commercial EUV nanolithography machines. The second one uses flat solid tin targets in normal incidence to the laser beam. Flat targets eliminate the geometric effects of irradiating a spherical surface and are more representative of a common starting-time condition for many theoretical works of plasma expansion in vacuum: an infinite 1-D target with a density step-change between vacuum and the target.

Sections 2.1 and 2.2 of this chapter have been published as [45].

2.1 LASER REQUIREMENTS

The state of the art extreme ultraviolet (EUV) sources for nanolithography use high-energy lasers which are focused on liquid microdroplets of tin inside a vacuum chamber, creating a laser-produced plasma (LPP) that emits 13.5 nm light [12]. Key plasma characteristics such as the temperature and density are heavily influenced by the input laser parameters [31, 32, 46]. These characteristics will in turn govern more practical effects such as the EUV emission spectrum and power, and the energy distribution of emitted ions. A great deal of insight on laser-plasma interaction can be obtained by studying the emission of photons and ions from LPPs for different input laser parameters [36, 47–49].

To study such laser-plasma interactions, we built a high-energy Nd:YAG system with tunable pulse duration in the picosecond range and showed that laser parameters play a key role in the deformation of the microdroplets [22, 24] and in the energy distribution of the ions emitted by the laser-produced plasma [43, 50]. We now aim to extend these studies by using femtosecond pulses to probe beyond electron-phonon interaction timescales, and study ion emission for the case where all the laser energy is deposited before ion dynamics take place. The pulse energies required for laser-plasma interaction studies are typically in the 10 mJ range and above. To generate femtosecond pulses with such high energy, we designed an optical parametric chirped-pulse amplifier (OPCPA) using the ps Nd:YAG amplifier mentioned above as the pump beam, and a commercial ultrashort fiber oscillator-amplifier system at 1.55 μm wavelength as the seed source.

Compared to 532 nm pumped OPCPA systems [51–57], direct pumping with 1064 nm offers a higher pump energy, and it yields a very useful 3.5 μm idler beam when the system is seeded at 1.55 μm. While this work focuses on the amplification of the 1.55 μm seed beam, there is a great deal of interest and work done in femtosecond sources in the mid-IR [58–60]. However, phase-matching schemes in available crystals are less optimal for ultra-broadband amplification, compared to systems pumped by frequency-doubled Nd:YAG at 532 nm and seeded by Ti:sapphire lasers. To circumvent this limitation, prior authors have used quasi-phase matching in periodically (and also aperiodically) -poled Lithium Niobate (PPLN) [58, 61–63]. However, due to the limited power handling capabilities of PPLN, pulse energies are typically limited to tens of μJ. KTA- and KTP-based optical parametric amplifiers (OPAs) have been used to produce mJ-level 1.5 μm and 3.5 μm pulses [59, 64, 65]. However, the broadest

phase-matching bandwidth for 1064 nm pumping is centered at 1470 nm, where direct seed generation is challenging due to the absence of broadband laser gain media, and additional nonlinear conversion steps are required [59]. Another configuration for ultrashort pulse generation near 1.5 μm is to change the pump wavelength to the Ti:sapphire range, enabling a white-light-seeded OPA working near degeneracy [66].

When choosing the seed wavelength at 1550 nm (telecom wavelength), fs sources and efficient optics are readily available [67]. This leads to a choice between more involved seeding schemes that produce shorter pulses or a more straightforward approach based on commercial components for higher efficiency and less complexity. Because LPP applications often have more stringent demands on pulse energy and stability rather than pulse duration, in this work we explore the latter option.

2.2 LASER SOURCE

In this section, we describe in detail the pump beam generation as well as the OPCPA system. The pump laser system consists of an Nd:YVO_4 oscillator and pre-amplifier, followed by an Nd:YAG power amplifier. The amplification stages are based on two separate systems [68, 69]. The OPCPA is 3-stage system using KTA crystals, where the first two stages have a non-collinear geometry, while the last stage is collinear to avoid generating a spatially dispersed idler beam.

2.2.1 *Picosecond pump laser system*

The pump laser system is seeded by a home-built Nd:YVO_4 master oscillator, operating at a wavelength of 1064 nm. The crystal is end-pumped by a fiber-coupled diode array which emits 18 W of continuous-wave (CW) radiation at 880 nm [70, 71]. Mode-locking is achieved with a saturable-absorption mirror, resulting in 50 nJ, 7 ps pulses at a repetition rate of 100 MHz. To enable amplification of these pump pulses to the >100 mJ level while avoiding optical damage, a slightly longer pulse duration is preferred. Therefore, a pulse duration adjustment system was implemented. In this system (Fig. 2.1), the beam passes through a grating in a 4-f system with an adjustable slit being placed in the Fourier plane, where the spectral content is spatially separated. By adjusting the opening of the slit, the spectrum of the laser is clipped, resulting in a tunable

pulse duration up to 120 ps. For OPA pumping, the pulse duration is set to 100 ps. The downside of wavelength selection to achieve longer pulses is the lower seed power available for subsequent amplifier stages. However, this is not a limitation as the pulse energy needs to be reduced to 0.75 nJ with a waveplate and thin-film polarizer (TFP) due to power limitations of the pulse-picking system that follows next.

The spectrally-clipped 100 ps pulses are coupled to a fiber-based pulse picking scheme comprising an acousto-optical modulator (AOM) and an electro-optical modulator (EOM). The AOM (Gooch & Housego Fiber-Q) has a high contrast of 50 dB and can withstand the average power of the oscillator at the full repetition rate, but its 30 ns rise time is not sufficient to select single pulses from the 100 MHz pulse train. We therefore use it to time gate a 400 ns window, containing 40 consecutive pulses, at a 100 Hz repetition rate. The subsequent EOM (Jenoptik AM 1064) has a specified rise time of 0.25 ns with a lower contrast of 30 dB, and is controlled by an arbitrary waveform generator. The EOM can pick, from the lower average power burst after the AOM, any number of isolated pulses. In normal operation for OPA pumping, a single pulse is picked. This pulse picking assembly combines the high contrast of the AOM with the speed and flexibility of the EOM. For the present OPCPA pumping application it is mainly used to reduce the repetition rate to 100 Hz, but it can also be used for more advanced schemes, such as pulse trains with adjustable time delays (in increments of 10 ns) between each pulse [43].

After the pulse picking, the pulses are first amplified by two grazing-incidence "bounce" pre-amplifier stages. The system comprises two Nd:YVO_4 crystals, doped at 1% and 0.5%, and with dimensions of $5 \times 2 \times 20$ mm and $6 \times 4 \times 20$ mm, for the first and second crystals, respectively. The design of this bounce amplifier closely follows the concept presented by Morgenweg et al. [68]. As shown in Fig.2.1, the crystals are pumped from the side by quasi-continuous-wave (QCW) pulsed laser diodes (DILAS MY-series) tuned to 880 nm through temperature control. These QCW diodes provide high pump fluence for 120 µs (slightly longer than the upper state lifetime of Nd:YVO_4) at a repetition rate of 100 Hz, resulting in a high gain with negligible thermal effects on the crystal or beam propagation. The significant doping level combined with strong single-sided pumping creates a region of very high gain confined close to the pumping surface. The beam travels through this high-gain region at an angle, and is aligned such that it undergoes a total internal reflection at the center of the pumped surface. This reflection averages away the inhomogeneity caused by

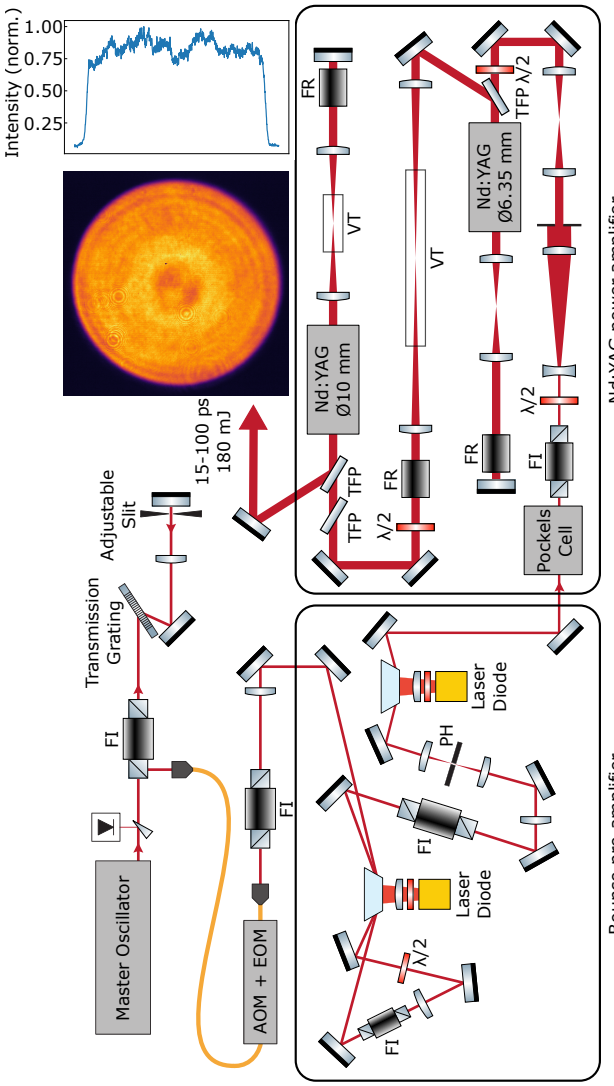

Figure 2.1: Schematic of the 1064 nm pump source, consisting of the oscillator and spectral clipping system, the bounce pre-amplifier and the power amplifier units. The final output beam profile is shown on the top right, imaged from the second YAG module to a CCD camera. FR: Faraday rotator; FI: Faraday isolator; PH: 200 µm pinhole; TFP: Thin-film polarizer; VT: Vacuum tube; $\lambda/2$: Half-wave plate.

the side-pumping geometry. Without this reflection, the beam would experience higher gain closer to the pumped crystal surface, leading to an uneven amplified beam profile.

The first crystal is traversed twice, using an optical isolator in between the passes to avoid parasitic lasing. After this double pass the pulse energy reaches 180 μJ. With an input energy of 120 pJ, that amounts to an average gain per pass exceeding 10^3. A consequence of the high gain is a significant amount of amplified fluorescence in addition to the amplified seed pulse. To improve pulse contrast before the second bounce amplifier stage, the amplified beam is focused through a 200 μm pinhole. Since the amplified beam and the fluorescence have slightly different a divergence and beam shape, this spatial filter can be set up such that the amplified pulse is transmitted more efficiently than the fluorescence background. After a single pass through the second crystal, we achieve a pulse energy of 1.4 mJ, which is sufficient to effectively seed a power amplifier based on large-aperture Nd:YAG rods. For optimum stability, the EOM selects a pulse from the center of the pulse train transmitted by the AOM, which results in a series of pre-pulses at 0.1% peak energy transmitted into the amplifier. In addition, after amplification we observe 0.6 mJ fluorescence in a 120 μs time window.

To prevent these parasitic pulses and most of the amplified fluorescence from the pre-amplifier from reaching the power-amplifier and extracting gain, two Pockels cells (PCs) and polarizers are placed between the pre- and power-amplifier stages. These PCs have rise and fall times of 5 ns, sufficiently fast to pick a single pulse, with a contrast greater than 2000:1, experimentally verified with a fast photodiode. An optical isolator is used as the last polarizer of this assembly, to protect the preceding systems against amplified back-reflections from the power-amplifier.

The power-amplifier comprises two Nd:YAG amplification modules (Northrop Grumman REA6308 and REA10008), which are both employed in a double-pass configuration [69]. These modules contain 146-mm-long cylindrical Nd:YAG rods with 6.35 and 10 mm diameter, respectively. The rods are transversely pumped by QCW diodes arranged in a five-fold symmetry. Especially in this amplifier stage, the QCW pumping enables high gain and stored energy while keeping thermal effects at a manageable level. For effective OPCPA pumping it is beneficial to have a flat-top spatial beam profile after the power amplifier. To this end, the Gaussian beam from the pre-amplifier is expanded to 12 mm ($1/e^2$-diameter) and passes through a 2 mm diameter aperture. The beam profile

at the aperture plane is imaged in the center of the first Nd:YAG module. This first module has a diameter of 6.35 mm and is under-filled by a 5.4 mm beam. Although more energy can be extracted by using a larger beam inside the rod, we found that this results in the five-fold pattern of the pump geometry being imprinted on the outer edges of the beam.

To mitigate the effects of thermally-induced lensing and birefringence, a double-pass amplifier configuration is utilized [69, 72, 73]. The plane inside the rod at which the aperture is imaged, is subsequently relay-imaged by a telescope with unit magnification, onto a mirror which reflects the beam back for the second pass through the rod. A Faraday rotator placed close to this end mirror rotates the polarization of the beam by 90° after a double pass. This combination of spatial imaging and polarization rotation results in a compensation of the thermally-induced birefringence in the Nd:YAG rod [73]. After the double-pass, the resulting polarization is linear and rotated over 90° with respect to the incident beam, allowing convenient beam extraction with a TFP.

The image plane in the first amplifier rod is then relay-imaged in the center of the second module, using a telescope that expands the beam diameter to 8.6 mm. A Faraday rotator is placed in this telescope between the modules, which in combination with the TFPs optically isolates the passes to prevent self-lasing and damage from high-energy back-reflections. To prevent optical breakdown in air, a vacuum tube is placed at the focus of each imaging telescope after the first double-pass amplifier. Similar to the first module, the beam from the first pass through the 10 mm diameter Nd:YAG module is imaged onto a mirror and back-reflected for a second pass, with a 90° rotated polarization.

The wavelength of the pump diodes can be controlled through temperature tuning, enabling adjustment of the overlap with the Nd:YAG absorption band. Optimization the pump wavelength leads to a higher energy output, but also results in a stronger absorption with a shorter absorption length close to the outer diameter of the rods, and therefore a spatial gain profile that peaks towards the rod edges. As a result, temperature tuning of the pump diodes also enables some control over the output beam profile, and we exploit this feature to optimize the flat-top profile at the end of the amplifier chain. The resulting beam profile is depicted as an inset to Fig. 2.1. We operate the modules at 240 V for 235 µs at a peak current of 70 A and 85 A to reach gain saturation for the first and second modules, respectively. For optimal beam profile the temperatures are set to 21.5 °C and 20 °C, respectively. The final amplified output energy is 180 mJ, for a pulse duration of 100 ps. This energy level is intensity-limited,

determined by the damage threshold of the optical coatings on the Nd:YAG rods and other components. At longer pulse durations, higher pulse energy can readily be extracted from the amplifier. The output energy can also be scaled further by utilizing amplifier rods with a larger diameter, allowing for larger beam diameters.

2.2.2 *Picosecond pulse pair configuration*

In its OPCPA pump configuration as described above, the fiber-coupled pulse picking is used to pick a single pulse at up to 100 Hz, but it can also be used in a more advanced configuration to produce a pair of pulses with near-independent energies and a tunable delay between them, adjustable in 10 ns increments (10 ns being the pulse separation of the 100 MHz pulse train produced by the master oscillator). That configuration is described below and shown in Fig. 2.2.

As is the case in the single pulse configuration, the AOM, due to its slow rise and fall times, first selects a pulse sequence (minimum of 40 pulses, but the sequence can be longer to deliver longer delays between the two pulses) from the 100 MHz oscillator pulse train, at up to 100 Hz. From this sequence, the EOM then selects two pulses with the desired delay, with the energy ratio between the pulses coarsely defined by the input waveform into the EOM. While the EOM has fast rise and fall times for single pulse picking, its contrast is insufficient to adequately suppress the pulses between the selected pulse pair, as the AOM is open between the first and second pulses. To fully suppress these in-between pulses, a second Pockels cell is added to the system, such that each pulse is gated by its own Pockels cell. This also allows us to use the timing on each Pockels cell to slightly clip the pulses and control their energies more accurately than by controlling the voltage applied to the EOM. This was especially useful in the cases where the energy of the first pulse is much lower than that of the second and precise energies were necessary.

2.2.3 *Ultrafast optical parametric chirped pulse amplifier at 1.5 μm*

The OPA is seeded by a commercial Erbium-doped fiber laser (C-Fiber Sync High Power by Menlo Systems), which delivers 3 nJ, 90 fs pulses at 100 MHz repetition rate. The laser is equipped with a fast response piezo-mounted cavity mirror, which is used to synchronize its repetition frequency to that of the oscillator in the pump system. For this purpose, the repetition rates of both oscil-

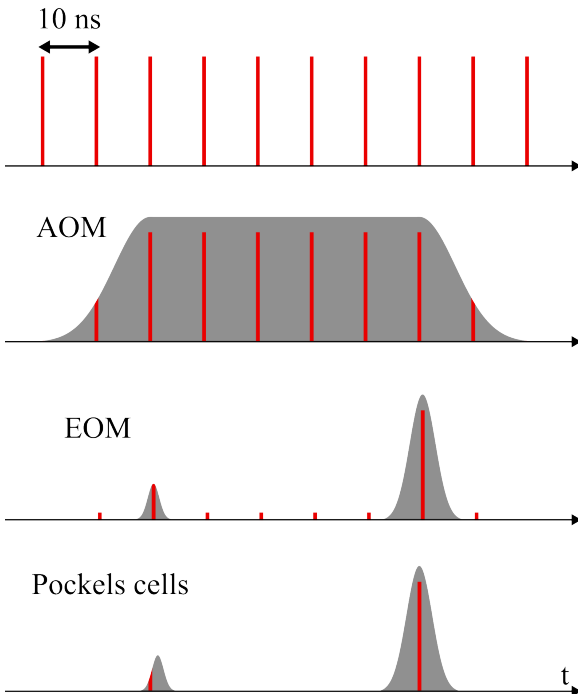

Figure 2.2: Schematic of the pulse picking process in pulse pairs configuration.

lators are monitored using fast photodiodes (EOT-3500, 12.5 GHz bandwidth). The photodiode outputs are fed into a 1.5 GHz-bandwidth frequency mixer to produce a difference frequency beat signal, which is then used as input for a PID loop which actuates on the piezo. As the difference frequency is sensitive to the relative phase between the two repetition rate signals, the relative time delay between the two laser pulse trains remains fixed each time the loop is closed. This locking scheme typically achieves timing stabilization at the 1 ps level. In addition to the piezo-mirror, the laser oscillator is also equipped with a stepper motor with a larger operating range, which enables coarse compensation of longer-term drifts and day-to-day differences in lab conditions.

The femtosecond pulses are stretched with positive group-velocity dispersion to a duration of around 30 ps in a Martinez-type 4-f grating system. The stretcher contains two equal 940 lines/mm transmission dielectric gratings with a manufacturer-specified diffraction efficiency of 95%, with an overall measured efficiency of 83%.

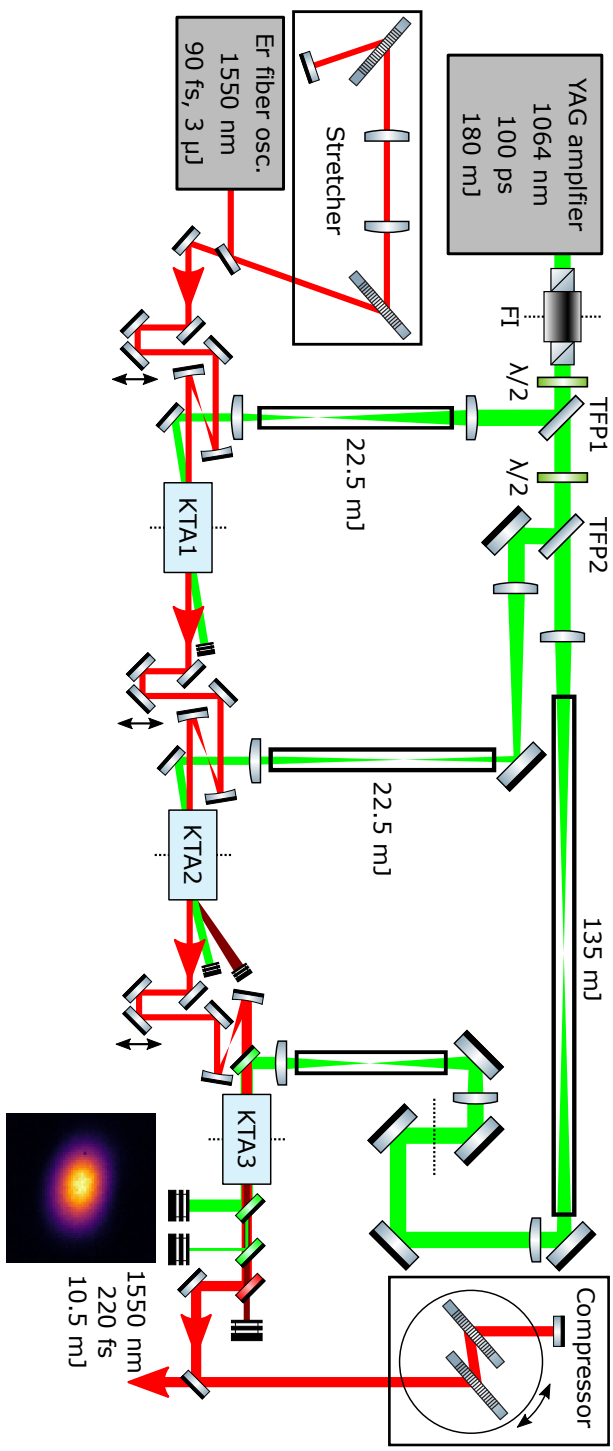

Figure 2.3: A detailed schematic of the OPCPA system. The dotted lines are points where the flat-top beam profile of the pump beam is imaged. On the bottom right we show the signal output of the OPCPA, focused by a 50 mm convex lens to a 75 µm spot ($1/e^2$-diameter). The same acronyms as in Fig. 2.1 are used.

A schematic of the OPA layout is shown in Fig. 2.3. The OPA consists of three single-passed 10 mm long, $\theta = 42.5°$ KTA crystals (Castech Inc.). The first two passes are set up in a noncollinear geometry, with noncollinear angles of 2° and 1.5°, respectively. This geometry allows for the pump and idler beams from the first two passes to be easily separated from the amplified signal beam. The noncollinear geometry also has a slightly broader gain bandwidth (Fig. 2.4, green trace). The pump beam is *s*-polarized, while the seed beam is *p*-polarized, for all three stages.

The pump beam is imaged on the first and second crystals, resulting in smooth flat-top spatial profiles with diameters of 1.7 mm and 1.9 mm, respectively. The seed beam has a $1/e^2$ diameter of 1.3 mm in both crystals. Both stages are pumped at 22.5 mJ and the seed is amplified to 1.4 mJ after the first two stages.

The third OPA stage is set up in a collinear geometry. While this results in a reduced gain bandwidth (Fig. 2.4, blue trace), it has the benefit of producing an idler beam that is not spatially dispersed so that it can be used in future experiments. The pump and seed beams have diameters of 4.0 mm and 3.4 mm ($1/e^2$), respectively. The last stage is pumped by up to 135 mJ and produces up to 12.5 mJ of uncompressed 1550 nm pulses. Fluorescence at the signal wavelength was characterized by blocking the seed to the first OPA stage while pumping all stages at full power. In this configuration, the fluorescence energy remains below the mW-level detection limit of the power meter.

After the final crystal, there is a significant imprint of the pump spatial profile onto the signal beam, resulting in a flat-top-Gaussian mix that diffracts as it propagates. Nevertheless, the beam can be focused into a smooth Gaussian-like profile with a $1/e^2$-diameter of 75 µm by a plano-convex lens, as shown in the inset of Fig. 2.3.

To separate the outgoing beams, we use a set of custom-designed dielectric dichroic mirrors (Layertec). The first of these mirrors reflects the pump beam while transmitting both signal and idler, and afterwards signal and idler are separated with another dichroic mirror. In practice, two pump-separating mirrors are used to remove the pump radiation from the amplified signal beam with sufficient contrast.

The amplified signal pulses are compressed by a pair of gratings identical to those in the stretcher. Using transmission gratings enables us to use an efficient Littrow configuration in the compressor, and have a compact layout that can be conveniently mounted on a rotation stage for fine-tuning the compression [52], as the input angle provides control over the ratio between second- and third-

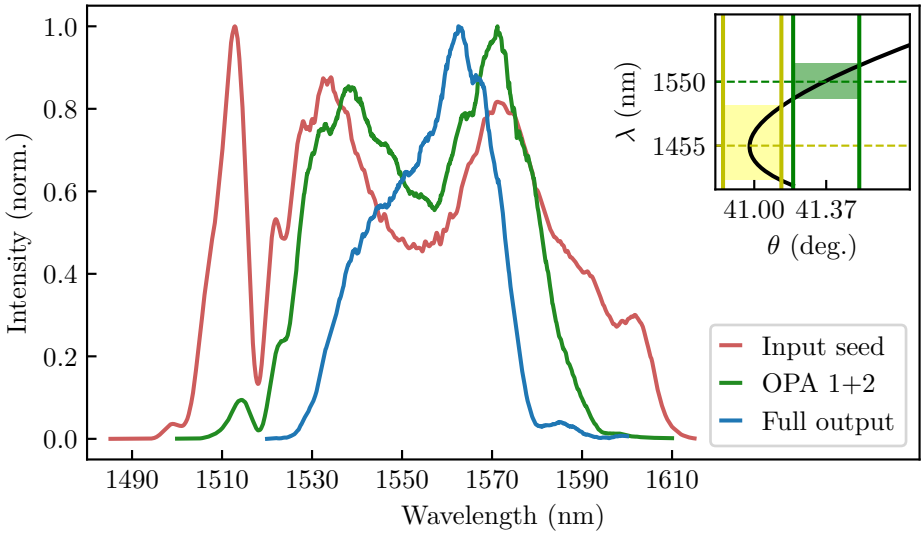

Figure 2.4: Spectra at various stages in the OPCPA system. The inset shows the phase-matching curve for KTA with 1064 nm pumping. The shaded areas highlight the phase-matching bandwidths for a 0.15° acceptance angle, centered at 1455 nm (yellow) and 1550 nm (green). λ: wavelength; θ: phase-matching angle.

order dispersion. Like the stretcher, the compressor boasts a high efficiency of 85%, resulting in compressed pulses of 10.5 mJ. Over timescales of minutes, an energy stability of 1.5% rms was typically measured.

2.2.4 *Pulse characterization*

As shown in Fig. 2.4, after two stages, the amplified spectrum is narrower than the initial seed spectrum. This is due to the limited phase matching bandwidth. The effect is further exacerbated after the third stage, due to the collinear geometry. To characterize the resulting pulse duration after the full amplifier system, we use a second-harmonic-generation frequency-resolved optical gating (SHG-FROG) device containing a 200 µm thick BBO crystal into which we send a small fraction of the amplified output beam. The measured and reconstructed SHG-FROG traces are shown in Fig. 2.5, along with the retrieved pulse shape. The Fourier-transform (FT) limited pulse durations corresponding to the input

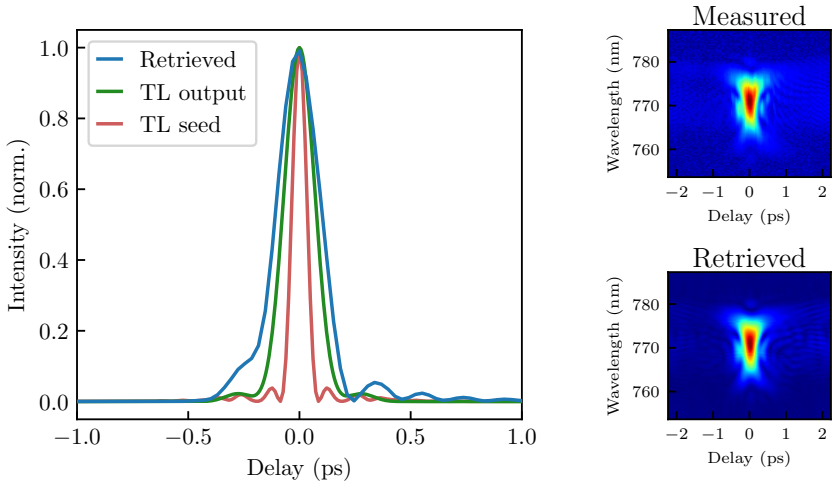

Figure 2.5: Pulse characterization of the OPCPA output at full amplification, using SHG-FROG. Transform limited pulses were calculated from the spectra shown in Fig. 2.4.

seed and amplified output spectra are also displayed for comparison. We find that the gain bandwidth in the collinear geometry increases the FT-limited pulse duration from 73 fs at the input of the OPA to 158 fs after all three crystals. The actual duration of the compressed pulse was measured to be 220 fs, as shown in Fig. 2.5. The discrepancy with the FT-limit likely comes from uncompensated residual higher-order dispersion, or possibly spectrally dependent gain saturation effects [74].

If a spatially dispersed idler is not an issue, then with a noncollinear geometry for the third OPA stage, one could also achieve a broader bandwidth and a subsequent reduction of the achievable pulse duration.

2.3 TARGET CHAMBERS FOR LASER-PRODUCED PLASMA EXPERIMENTS

Above, we described the two laser sources (a fs OPCPA, and a ps pump laser as a standalone system), that represent the "laser side" of our studies on laser-produced plasma. Just as important are the interaction chambers where the metal targets from which the plasma is created and its emissions studied.

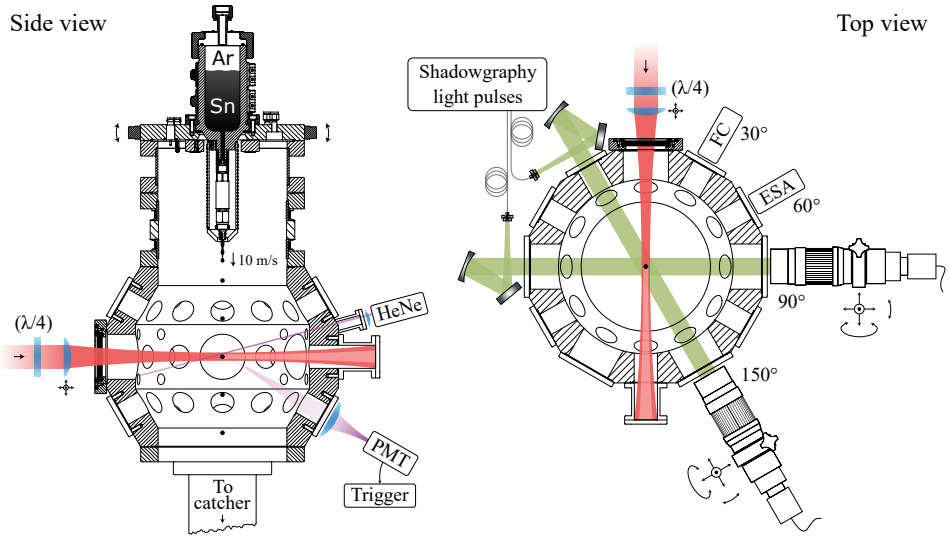

Figure 2.6: Side view (left) and top view (right) of the droplet generator chamber. Figure from [19].

Two interaction chambers with different target types were used for the experiments described in this thesis: one equipped with a tin microdroplet generator, another with flat solid tin targets. Both chambers were fitted with various ion diagnostics and target imaging setups for each experiment presented in this thesis, which will be described in detail in their corresponding chapters. In the sections below we describe the general designs and capabilities of each target chamber, common across the various experiments.

2.3.1 *Droplet generator setup*

This setup was developed and maintained by EUV Plasma Processes group at ARCNL, led by Dr. Oscar Versolato, and is described in great detail by D. Kurilovich [75] and R. Meijer [19]. Fig. 2.6 shows a schematic of the target chamber including all the diagnostics used in the experiments performed during the course of this thesis. Each diagnostic will be described in detail in the chapters where the experimental results are presented: Faraday cups and shadowgraphy imaging in chapters 3 and 4, electrostatic analyzer in chapters 5 and 6.

The chamber operates in high-vacuum ($\sim 10^{-7}$ mbar), with the droplet generator mounted above the main body of the vessel. The microdroplet generator comprises a reservoir, which holds and heats tin above its melting temperature, and a nozzle assembly (also heated to prevent tin from solidifying and clogging the nozzle). A tin catcher is mounted directly below the droplet generator. The catcher is also heated to ensure that the used tin remains liquid, such that the catcher fills evenly, rather than solidifying around the edges, which could lead to early clogging.

During operation, the tank is filled with high-purity (99.995%) tin, which is heated to 260 °C, above its melting point of 232 °C. Argon is then used to pressurise the tank to 10.5 mbar, starting the flow of tin through the nozzle. The transition from uncontrolled flow to a stream of equally-sized droplets is achieved by using a piezo element integrated into the nozzle. The frequency applied to this piezo element is the primary control knob to adjust the droplet diameter. To produce the droplet diameters of 30 μm and 45 μm used in this thesis, the piezo element was driven at 30 kHz and 10.2 kHz, respectively. Additionally, the pressure in the reservoir affects the droplet diameter as well as the separation between droplets. However, the effect is small in comparison to changes in piezo frequency and, for any given frequency, there is a narrow range of reservoir pressures that allow for a stable droplet stream.

To produce a trigger signal from the droplet stream, a He-Ne laser is used to create a horizontal light sheet positioned 3 mm above the center of the chamber. As the droplets cross the sheet, the scattered light is captured by a photo-multiplier tube, producing a signal with kHz frequency which is then down-converted to 10 Hz and distributed to the various diagnostics and laser sources used.

As described in the sections above, the master oscillator used for the Nd:YAG is unseeded and free-running, and as such cannot be triggered to produce pulses on demand. The pulse picking and the various amplifier modules following the oscillator can be triggered, but simply triggering them using the droplet trigger signal would result in significant energy jitter, as the pulse picking time window might only partially overlap with a laser pulse or even none at all. To solve this issue, the trigger signal from the droplet generator is used as a trigger-enable signal which prompts the laser triggering system to accept the first available trigger from the 100 MHz pulse train, correctly timing the pulse picking and amplifier chain. The downside of this approach is the introduction of a timing jitter between the laser and the droplet target, since the next available pulse after

the trigger-enable is received can arrive up to 10 ns later. This jitter however is small enough to not affect our experiments.

At a typical droplet speed of 10 m/s, this timing jitter translates to a vertical alignment jitter below 100 nm, which is small compared to the droplet diameter. This is further mitigated by the fact that the typical focus used for these experiments was an 80-μm-diameter (FWHM) Gaussian which significantly overfills both droplet sizes, meaning that this jitter only results in a minute change in the energy distribution at the droplet surface.

Time-of-flight (TOF) diagnostics, such as FCs and ESAs, are more sensitive to temporal jitter that could affect the TOF calculation. However, these diagnostics determine the laser impact time by detecting a small current spike due to electrons, rather than the trigger timing. As such, they are unaffected by this laser timing jitter.

2.3.2 *Solid target setup*

The second target chamber uses solid tin targets which complement the results obtained from the microdroplet targets. While droplet targets are more representative of commercial EUV lithography sources, solid targets offer a simpler geometry without effects such as the mismatch between the droplet and focus sizes, and the effect of the curved surface of the droplet on the absorption coefficient. Many theoretical works on laser-metal interactions make the assumption of a 1-D infinite target with a step-change in density as a starting condition [76–78], which are more representative of a solid flat target as opposed to the more complex geometry of the microdroplet targets. Solid targets also come with logistical advantages, allowing us to perform experiments on demand, without some of the planning and timing constraints associated with droplet target beamtimes.

The vacuum chamber and solid target assembly are shown in Fig. 2.7. The chamber operates in high-vacuum ($\sim 10^{-6}$ mbar), with the target mounted in the geometrical center of the spherical chamber, normal to the incident laser beam. Irradiating a flat normal surface rather than a spherical droplet results in ion emissions to be directed in a narrower cone facing the incoming beam direction. Because of this, a large port was added to the chamber to fit a custom-designed flange which features a small laser input port and three ports at 12° with respect to the input beam, where most diagnostics will be positioned.

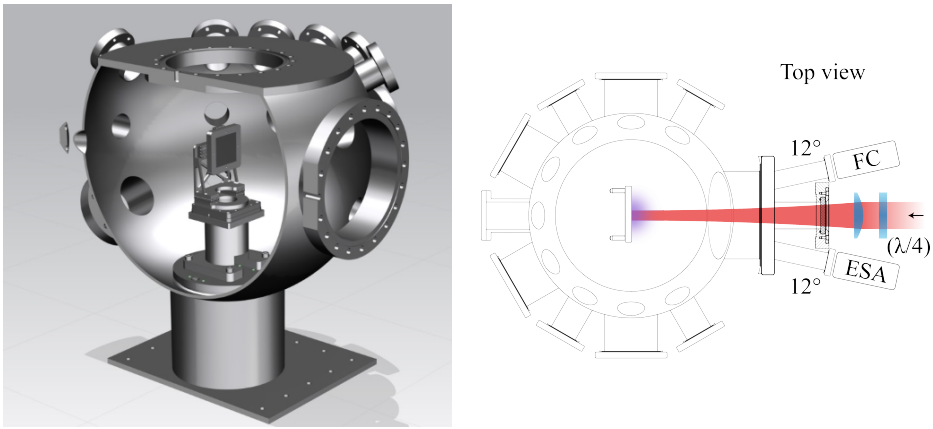

Figure 2.7: Left: 3D model of the chamber showing the target holder and positioning system. Right: Top view diagram of the chamber and diagnostics configuration.

The targets used were 1 mm-thick square plates of 99.99% purity tin. Each target is cut from a larger sheet, cleaned with acetone and placed mounted on the target holder. The target holder leaves a 41x41 mm clear aperture, which is divided in a 35x35 grid of shot positions, each separated by 1 mm in the vertical and horizontal directions. This separation ensures that each new position is unaffected by adjacent positions which have already been used. To ensure the holder does not influence the measurements by interacting with the plasma plume or physically block any emitted ions, 3 mm are left between the sample point grid and the edge of the target holder on all sides.

The target holder is mounted on a translation-rotation stage equipped with piezo-stack actuators (Smaract), allowing for 3D positioning of the target, as well as rotation in the horizontal plane. This stage rasters the target along the point grid previously mentioned, with each position being illuminated by the desired number of pulses, until the grid is complete and the target is spent. The target chamber is then vented and the target can be replaced.

During experiments, target positioning, triggering, and data acquisition are handled by *Spanish Inquisition*, an in-house designed control software. Triggering is similar to the droplet target case. To deliver a shot on target, the control system sends a trigger-enable signal to the pulse picking system of the laser, which is then triggered by the first available pulse from the 100 MHz.

The same 10 ns jitter as discussed for the droplet generator setup is present, though it is not problematic since the target is stationary in this case. The control system also handles trigger distribution for all the diagnostics. *Spanish Inquisition* also automatically positions the target during shot sequences. After the user specifies a number of grid positions to irradiate and the number of laser shots at each position, the software moves the target to a chosen position in the grid. The specified number of laser shots is fired on that position, with diagnostics triggering and data storage automatically handled, and the target moves automatically along the grid until all positions have been irradiated. This automation was crucial in acquiring the large number of laser shots required by the statistics of ion measurements such as Faraday cups and electrostatic analyzers. Additionally, the fact that each measurement run is averaged over many shots and many target positions mitigates any effects caused by localised surface defects or contamination on the target surface.

3

CYLINDRICALLY AND NON-CYLINDRICALLY SYMMETRIC EXPANSION DYNAMICS OF TIN MICRODROPLETS AFTER ULTRASHORT LASER PULSE IMPACT

In this work, the expansion dynamics of liquid tin microdroplets irradiated by femtosecond laser pulses were investigated. The effects of laser pulse duration, energy, and polarization on ablation, cavitation, and spallation dynamics were studied using laser pulse durations ranging from 220 fs to 10 ps, with energies ranging from 1 mJ to 5 mJ, for microdroplets with an initial radius of 15 μm and 23 μm.

Using linearly polarized laser pulses, cylindrically-asymmetric shock waves were produced, leading to novel non-symmetric target shapes, the asymmetry of which was studied as a function of laser pulse parameters and droplet size. A good qualitative agreement was obtained between smoothed-particle hydrodynamics simulations and high-resolution stroboscopic experimental data of the droplet deformation dynamics.

This chapter has been published as [79].

3.1 INTRODUCTION

The current generation of nanolithography machines uses extreme ultraviolet (EUV) light to enable the printing of ever smaller features. To generate EUV radiation, a laser-produced plasma (LPP) is created by focusing high energy laser pulses onto liquid microdroplets of tin, where line emission from highly charged ions in the plasma produces the desired 13.5 nm light [80–85]. Some such laser pulses also induce strong shock waves on the metal droplets, causing them to deform hydrodynamically and, for the most intense pulses, undergo explosive cavitation [22–24, 46].

In the most efficient EUV generation schemes, two incident pulses are typically used. The first pulse is used to deform the droplet in a controlled way, to produce a tin target with a desirable spatial density distribution for more efficient light coupling and plasma generation by a second pulse. That target shape is subsequently irradiated by the second, more energetic pulse, creating an EUV-emitting plasma. Understanding and controlling the expansion induced by the first pulse is an important step in producing an optimal target shape.

Prior works have studied the deformation of liquid tin droplets irradiated by femto- and picosecond laser pulses [24, 25, 46, 86, 87]. A general observation is that irradiation by such ultrashort pulses leads to the generation of intense pressure waves inside the droplet, resulting in shock-wave-driven phenomena such as cavitation and spallation, and associated explosive fragmentation. This behaviour is strikingly different from the dynamics induced by longer pulses with nanosecond duration, where the droplets mainly deform hydrodynamically into thin disks, driven by plasma pressure [22]. Recent evidence suggests that a droplet fragmented into a cloud of small particles, as one can obtain when using ps pulses, could be a favourable target for EUV generation [11, 12].

In the first part of this paper, prior studies by the authors on laser-induced cavitation of tin microdroplets are expanded to the case of irradiation by femtosecond pulses. The effects of laser pulse energy and duration on droplet deformation are examined, as it was established in [22, 24] that these parameters play an important role in various aspects of droplet deformation. In the second part, the effect of the polarization of the laser pulses on droplet deformation is studied. Results in literature have only addressed the case where the incident laser beam is circularly polarized. For that case, the absorption profile on the droplet surface is cylindrically symmetric. Using a linearly polarized incident beam instead leads to asymmetric shock waves in the droplets, creating

unique target shapes. These unique absorption profiles and consequent shock waves affect the spatial distribution of the material ablated from the front of the droplet as well as the shape of the spallation front, i.e. the liquid material ejected from the back of the droplet along the laser propagation direction. As this liquid debris poses risks to the delicate equipment inside the machine, accurate understanding on how to minimize and manage its presence is a key part of EUV nanolithography machine design. Understanding how to break the typical cylindrical symmetry in a controlled way could be a significant addition to current debris management solutions. To complement these studies, smoothed-particle hydrodynamics (SPH) simulations were used to calculate the propagation of cylindrically asymmetric shock waves in a liquid droplet, having shown qualitative agreement with the experimental results.

3.2 EXPERIMENTAL SETUP

The interaction chamber and the laser system used in this study have previously been described in detail [24, 45]. A schematic overview of the experiment is shown in Fig. 3.1. The droplet generator is operated in a vacuum chamber (10^{-7} mbar), holding a reservoir of tin above the center of the chamber at a temperature of 260 °C, well above its melting point of 232 °C. Liquid tin is pressured through a 6.5-µm nozzle, producing a multi-kilohertz train of 15- or 23-µm radius droplets of 99.995% purity tin. The droplets pass a horizontal light sheet produced by a helium-neon laser, while the scattered light is recorded by a photomultiplier tube. This signal is used to trigger the laser system at a reduced repetition rate of 10 Hz.

The laser pulses are generated in an optical parametric chirped pulse amplifier (OPCPA), comprising 3 KTA crystals pumped by a Nd:YAG amplifier at 1064 nm and seeded by a commercial fiber oscillator and amplifier at 1550 nm. The OPCPA system produces pulses with energies up to 10.5 mJ that can be compressed to a minimum pulse duration of 220 fs [45]. The pulse duration is varied by changing the distance between a pair of transmission gratings that make up the compressor. The laser energy is adjusted with a combination of a half-wave plate and polarizer. The polarization is then adjusted using an additional half-wave plate and a quarter-wave plate, allowing for circular as well as adjustable linear polarization. The beam is focused to a Gaussian spot with a diameter of 80 µm (FWHM), using a 500 mm focal length plano-convex lens. For a 5 mJ pulse, this results in laser fluences of 66 J/cm^2 and 62 J/cm^2

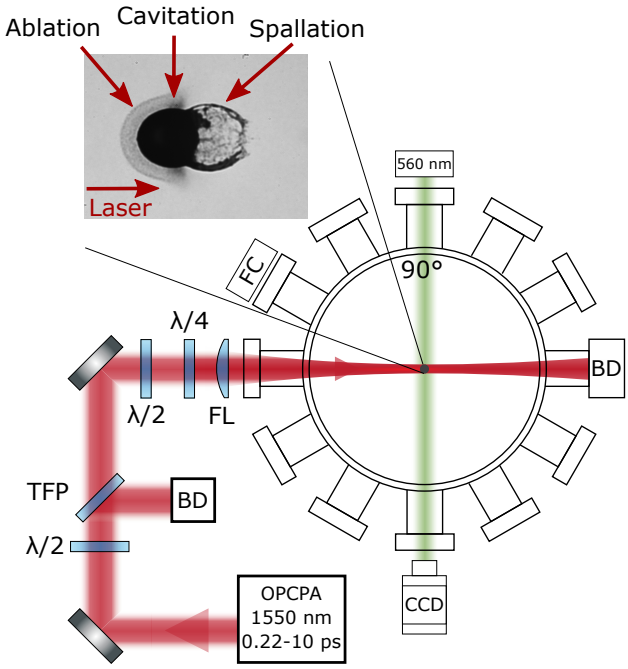

Figure 3.1: Simplified top-view diagram of the experimental setup. A combination of a thin-film polarizer (TFP) and half-wave plate ($\lambda/2$) is used to control pulse energy. BD: Beam dump; FC: Faraday Cup; FL: $f = +500$ mm focusing lens. Inset: shadowgraph of a tin droplet after laser irradiation (laser incident from the left side), highlighting the regions of interest of the different processes discussed in the text.

for droplets with radii of 15 µm and 23 µm, respectively. Although the surface cross-section and thus the total absorbed laser energy changes with droplet radius, having similar fluences on both droplet radii allows for comparisons between the data sets.

Time-resolved shadowgraphy was used to capture the temporal evolution of the droplet [24]. A single, temporally and spatially incoherent, 560 ± 10 nm wavelength, 5-ns-long light pulse illuminated the droplet at 90° from the input laser direction, in the plane of incidence of the laser. A long-distance microscope equipped with a CCD camera recorded the backlit droplet with a resolution of 4 µm. The temporal dynamics of the process were captured by recording shadowgraphy images at different time delays after laser incidence on the droplet.

3.3 RESULTS AND DISCUSSION

Upon irradiation by an ultrashort laser pulse, three main processes are induced in the tin droplet, which are ablation, cavitation and spallation. Each of these processes leads to characteristic deformations that can be tracked by shadowgraphy. The inset to Fig. 3.1 shows the response of an initially spherical tin droplet to irradiation by an ultrashort laser pulse. Upon laser impact, a thin layer of tin is rapidly ablated, and the ablated material can be seen travelling backwards in the direction of the laser source. When ultrashort pulses are used, the laser energy is deposited over a duration comparable to the electron-phonon coupling timescale ($\sim$ps), much shorter than hydrodynamical timescales ($\sim$ns). This fast energy deposition leads to a high-pressure shock wave that converges towards the center of the droplet. This shock wave consists of a strong compression wave, followed by a rarefaction wave. As the shock wave focuses near the droplet center, the increased negative pressure of the rarefaction wave may result in rupturing of the liquid structure and formation of a rapidly expanding cavity [24, 46, 86, 88]. This cavitation process leads to the expansion of the droplet into a spherical shell. The morphology and temporal dynamics of this expansion are dependent on laser parameters such as energy and pulse duration.

After passing through the center of the droplet, the shock wave propagates towards the back surface of the droplet. Upon reflection from this surface, the compression wave converts into a back-propagating rarefaction wave, which overlaps with the trailing rarefaction part of the incident shock wave close to the surface. The negative pressure caused by this combination of shock waves can exceed the tensile strength of the material, leading to spallation, i.e. the ejection of a sheet of liquid from the back surface [86].

The scope of the present work was to investigate the influence of laser parameters in the ultrashort pulse regime on the droplet deformation, focusing on the three phenomena described above. Firstly, the effects of energy and pulse duration were studied, using circularly polarized light. Circular polarization results in a cylindrically symmetric absorption profile on the irradiated surface, in turn leading to cylindrical symmetries for the processes described above. Following this, incident pulses with linear polarization were used, leading to a breaking of the absorption symmetry. This geometry gives rise to asymmetric shock waves and subsequent deformation processes, which were studied through experiments and simulations.

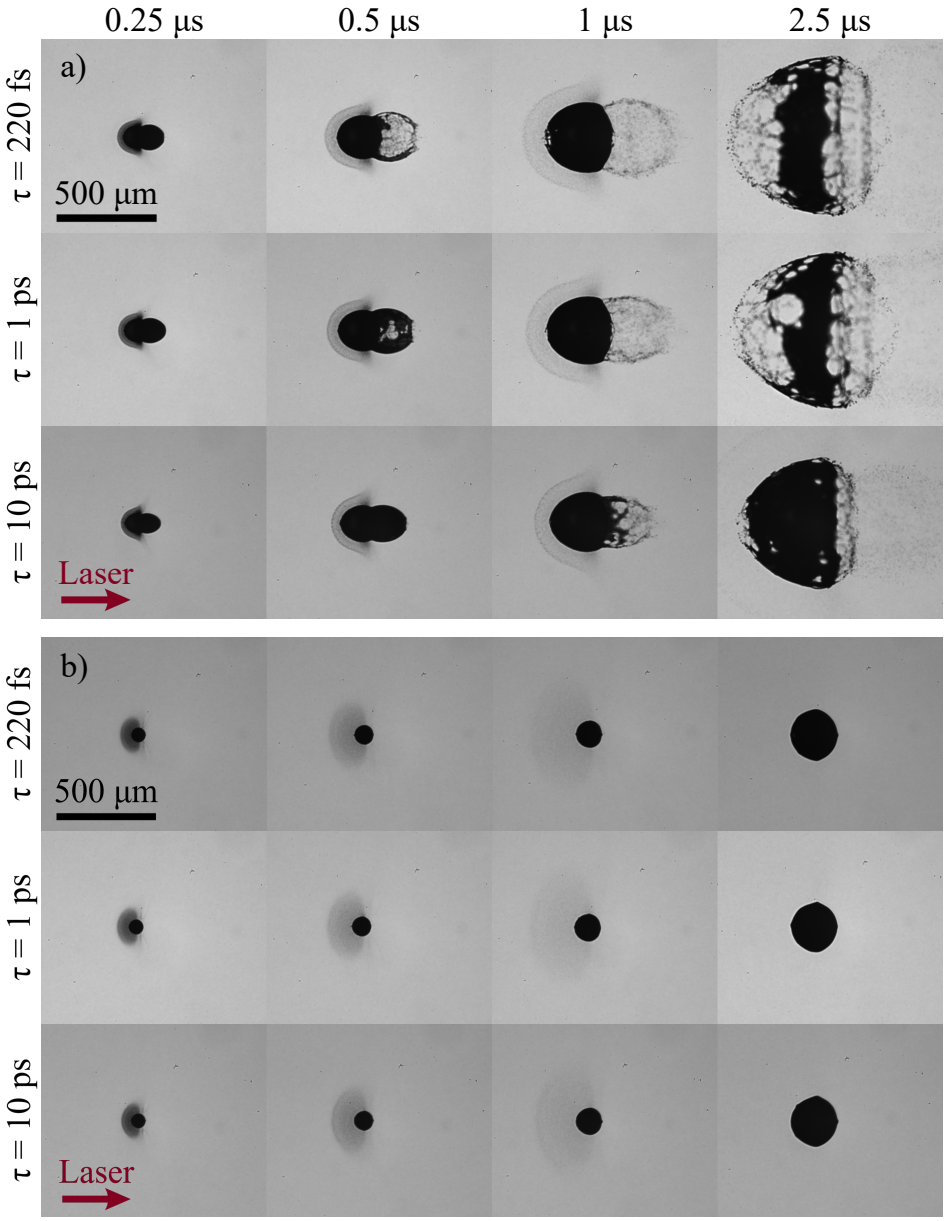

Figure 3.2: Shadowgraphy images of tin microdroplets (23 µm initial radius), taken at various time delays after laser irradiation (noted above the figure). Pulse energies of 5 mJ (a) and 1 mJ (b) are shown, for various pulse durations (indicated on the left of the figure). Laser spot size: 80 µm (FWHM).

3.3.1 *Effect of laser pulse energy and duration on droplet deformation*

Figure 3.2 shows the response of a tin droplet to irradiation by ultrashort laser pulses using circularly polarized light. The figure shows a time lapse series of images recorded at increasing time delays (ranging from 0.25 to 2.5 µs) after the laser pulse impacts at $t = 0$ seconds, for pulse energies of 5 and 1 mJ (Figs. 3.2a,b, respectively), and for pulse durations of 220 fs, 1 ps and 10 ps. In these images, clear droplet deformation as described above are observed. In all images, a shell of ablated material traveling back from the laser-facing side can be seen, as well as a spherical expansion of the liquid due to cavitation. For a pulse energy of 5 mJ, (Fig. 3.2a) clear spallation is also observed, initially forming a bubble-like shell on the back side of the droplet (i.e. the side opposite to where the laser impacts). At later times, this bubble breaks up into a large number of microparticles. For even later times, also the cavitation expansion leads to fragmentation of the thin shell. At the lower energy (Fig. 3.2b), the spallation is not observed, likely because the laser-generated shock wave is not sufficiently strong to exceed the material's tensile strength. One observation is that these deformations only weakly depend on the pulse duration in this regime. While at higher energies some differences are apparent, at lower energies the target shapes are strikingly similar even for a pulse duration variation by a factor $\sim$45. This is in line with predictions by prior authors [86].

3.3.1.1 *Cavitation dynamics*

To analyze the cavitation dynamics, a series of time-delayed shadowgraphy images was recorded. The radius $R(t)$ of the cavitation shell was tracked as a function of time using an image processing algorithm. Figure 3.3a shows an example of such radius tracking, indicating a linear time dependence of $R(t)$. The determination of $R(t)$ is complicated at early times ($t < 0.5$ µs) by the presence of the dense ablation front, and at late times ($t > 2$ µs) by fragmentation of the shell. Therefore, the expansion velocity $\dot{R}$ was determined by fitting a linear function to the intermediate times where the shell is clearly distinguishable and not yet fragmented.

Looking at the effects of pulse duration on the expansion velocity, it was found that for low energies (1 mJ in Fig. 3.3b), the expansion velocity is not clearly dependent on pulse duration, while for higher energies (5 mJ in

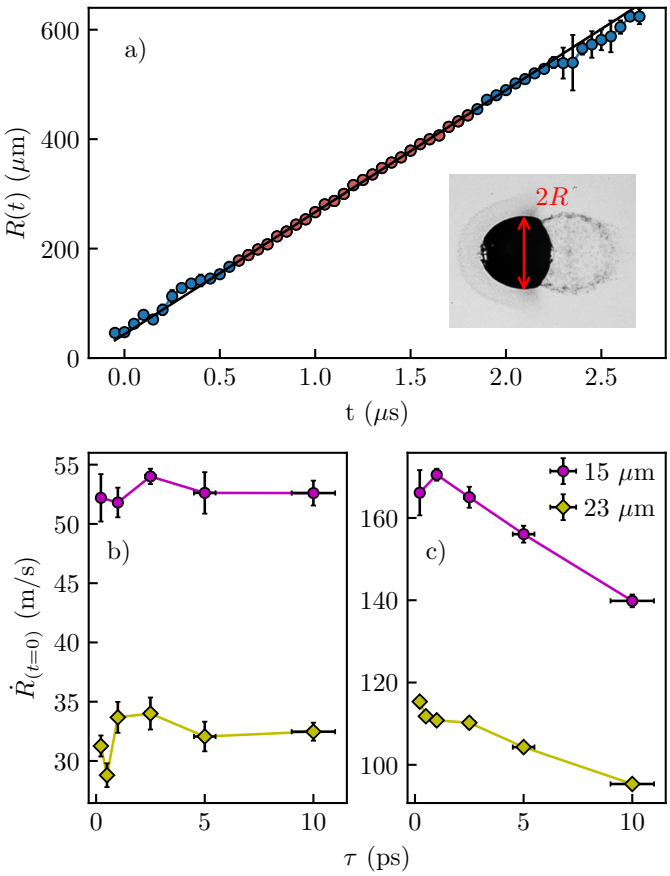

Figure 3.3: a) Temporal evolution of the cavitation shell a 23-µm-radius droplet, after irradiation by a 5 mJ, 200 fs pulse. The solid black line is the result of a linear fit to the data points highlighted in red. The slope of this fit is used to determine $\dot{R}(t=0)$; b) For 1 mJ pulses, $\dot{R}(t=0)$ is not dependent on pulse duration; c) For 5 mJ pulses, $\dot{R}(t=0)$ decreases for longer pulses. This is seen for both droplets sizes used: $R_0 = 15$ µm (pink circles) and $R_0 = 23$ µm (yellow diamonds).

Fig. 3.3c), there is a significant decrease in velocity towards longer duration pulses. These trends are seen for both initial droplet sizes.

The influence of incident laser energy on the expansion speed (at constant pulse duration) was also investigated, and shown in Fig. 3.4a. In previous work, such a measurement was already performed for a single pulse duration of

15 ps [24], and that study was now expanded to a range of shorter pulse durations. Similar to that previous work, by scaling each data sets by its corresponding initial droplet radius R_0, the data for different droplet sizes collapses onto a single power-law curve (Fig. 3.4b). This scaling behaviour originates from the relation between the magnitude of the induced shock wave and the irradiated droplet area, which is proportional to R^2, combined with the fact that the expansion is hindered by the mass of the droplet proportional to R^3, which results in a R^{-1} scaling.

The energy dependence of the scaled expansion velocity is well expressed by a power-law function $R_0 \times \dot{R}(t = 0) = A \times E^{\alpha}$, for all pulse durations used. This power-law description was previously observed for longer pulses [24], where a value $\alpha = 0.46$ was reported, using 15 ps pulses at 1064 nm wavelength. This power-law description is found to extend to ultrashort pulses below 1 ps. Notably, the power-law exponent α decreases as a function of pulse duration, as shown in Fig. 3.4c. In practical terms, this means that as the pulse duration increases, the shell expansion velocity scales less strongly with pulse energy.

When observing the spallation dynamics, at higher energies the process is again found to be less violent for longer pulses. At 1 mJ energy, no significant spallation is observed. At 5 mJ pulse energy, as the pulse duration increases, the spallation front expands more slowly and holes form in the shell at a later time (compare images at delay times 0.5 and 1 μs in Fig. 3.2a).

3.3.1.2 *Ablation dynamics*

The velocity of the ablation front is measured in a similar way to that described above for the cavitation, tracking the displacement of the ablation front as a function of time through image processing and fitting a linear function. This measurement was performed for a range of pulse durations at two different energies, of which the results are shown in Fig. 3.5. Similar to what was observed for the cavitation dynamics, at low energy the ablation front velocity is not clearly dependent on pulse duration, while for higher pulse energies there is a significant decrease in velocity for increasing pulse duration. Another observation that follows from Fig. 3.5 is that the ablation front velocity is the same for both droplet diameters used in the experiment, while at higher energies there is a significant increase for the smaller droplets.

Furthermore, in some measurements, a sharp higher-density edge in the ablation front is observed. This is best seen in Fig. 3.2, for 5 mJ pulses at 0.5 μs

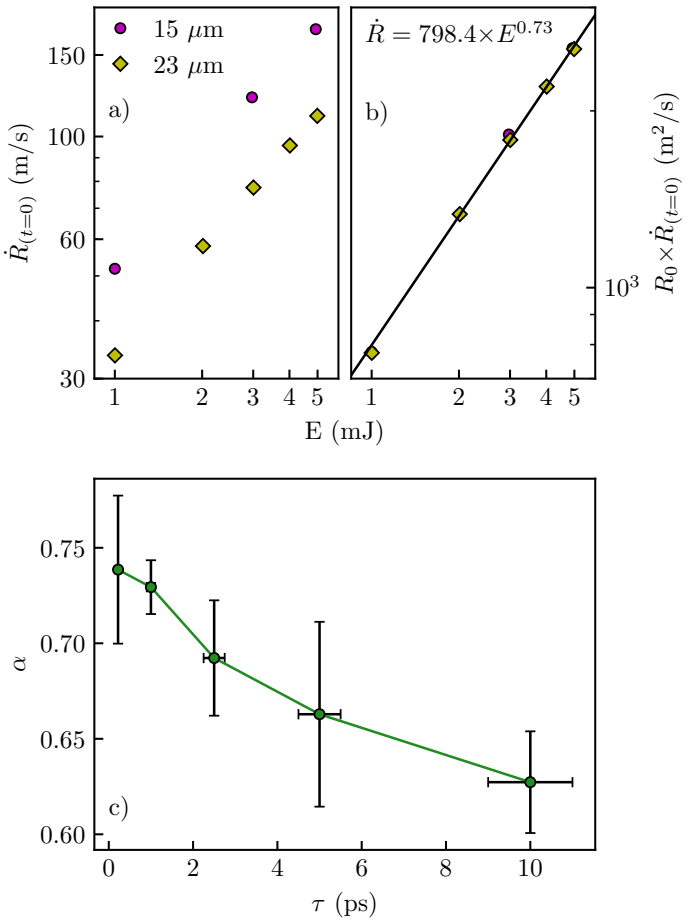

Figure 3.4: Top: Demonstration of the R_0 scaling for 1 ps pulses, as both data sets collapse neatly to a power law curve when multiplied by their corresponding initial droplet radius. Bottom: The power law exponent α decreases for longer pulses, indicating that cavitation dynamics are more sensitive to energy for shorter pulses.

and 1 μs delays. This sharp edge has been described as a two-phase liquid-gas mixture [89, 90]. The ablation front becomes increasingly visible as the pulse energy increases at fixed pulse duration, while at fixed laser energy the front becomes more apparent for longer pulses. This variation was not yet observed

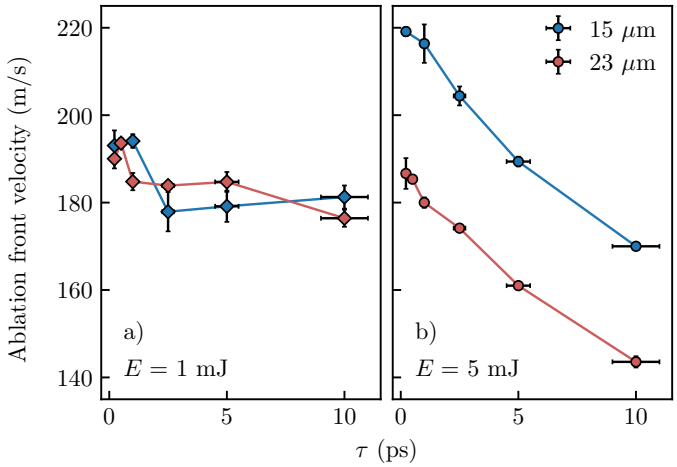

Figure 3.5: a) Velocity of the ablation front for a laser pulse energy of 1 mJ. The velocity is largely independent of pulse duration and droplet diameter. b) Ablation front velocity at laser pulse energy of 5 mJ. A significant dependence on both pulse duration and droplet diameter is found.

in measurements using longer 15 ps pulses at 1064 nm, where this edge was visible for all pulse energies [24].

3.3.1.3 *Discussion on deformation scalings*

These changes in ablation front and cavitation velocity with pulse duration can be explained by the increased influence of the generated plasma on the expanding material. As the incident energy per unit area on the droplet surface is almost identical for both droplet diameters, and ablation can be considered to be due to local heating, the droplet diameter should not influence the ablation front velocity in the absence of any other effect. However, the laser intensities used are sufficiently high to produce plasma, and the presence of a finite plasma density at the laser facing side would impact the observed deformation, since this plasma would exert a pressure on the deforming and ablated material passing through it.

Both the ablation front and the cavitation experience a drag when expanding into a plasma, which leads to a reduction in expansion velocity that scales with plasma density. To quantify the amount of plasma generated by the different

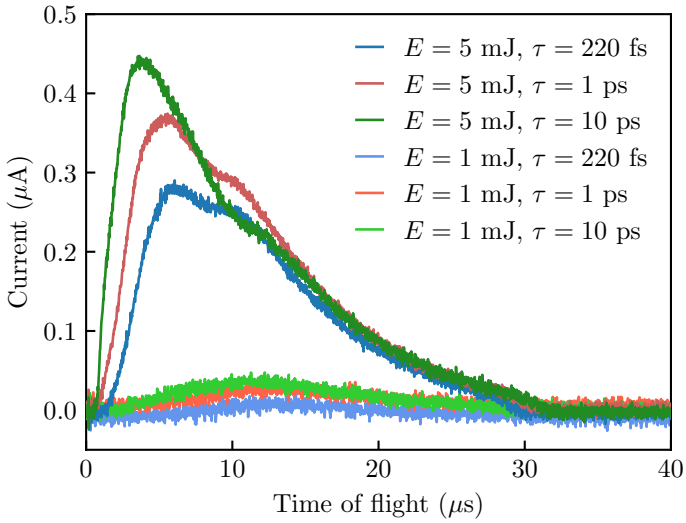

Figure 3.6: Ion time-of-flight traces recorded using a Faraday cup for different incident laser pulse parameters. An increase in ion flux is observed, at 30° from the incident beam, for increasing pulse duration at fixed energy.

laser pulses, a Faraday cup (FC) is placed on the target chamber at an angle of 30° with respect to the incident laser beam (in the backward direction). The FC records a time-of-flight trace of the ions emitted from the target after laser impact, as shown in Fig. 3.6. The charge detected by the FC allows a comparison of the amount of plasma generated for different laser parameters.

As expected, the FC data shows that the amount of plasma-related current produced by the laser sharply increases with pulse energy. But from these measurements it also becomes clear that the amount of produced plasma increases with incident pulse duration. The increased current and shift towards shorter time-of-flight seen in Fig. 3.6 for increasing pulse duration indicate that longer pulses lead to a higher-density and higher-temperature plasma upon impact. A possible reason for this scaling may be that on the timescale of the electron-phonon coupling, which is several picoseconds for most metals, lattice heating and subsequent evaporation and plasma formation start to occur, leading to a significant increase in absorption. As a result, longer pulses will be more effective in depositing energy into the material. This increased plasma density explains the formation of a more distinct front in the ablation plume for both higher energies and longer pulses. It also explains the reduction of ablation

and cavitation velocity for longer laser pulses: as such pulses produce more plasma, the drag on the expanding material increases. At low incident energy ($E = 1$ mJ) the FC data indicates that little plasma is formed, which would not produce a significant force on the expanding material, which explains the absence of an effect in Figs. 3.3b and 3.5a. The appearance of the dependence of droplet diameter is also explained from the plasma perspective. Larger droplets absorb a larger fraction of the incident beam simply by increased geometrical overlap with the laser focus, but also have lower local surface curvature. As ultrafast-laser-induced plasma expansion is strongly directional and oriented perpendicular to the surface [91, 92], a stronger surface curvature leads to a faster reduction in plasma density as a function of distance from the surface. Therefore, at constant laser energy and focal spot size, a larger droplet will experience more plasma pressure counteracting its deformation, both in expansion and ablation.

3.3.2 *Polarization-controlled droplet deformation*

Several papers have covered the topic of ultrafast laser-droplet interaction, including the role of laser-driven shock waves in the deformation dynamics [24, 46, 86]. To the best of our knowledge, all used circularly polarized light. The use of a circular incident laser polarization leads to an absorption profile that is cylindrically symmetric around the beam propagation axis. This symmetry can be broken by using linearly polarized light. That may result in a detectable effect on the generated shock wave dynamics, which is the scope of the present investigation.

Absorption and reflection profiles can be calculated with the Fresnel equations. For a curved surface, the incident polarization state must locally be decomposed into $s-$ and $p-$polarization with respect to the plane of incidence on each point of the curved surface. For clarity, the polarization of the incoming laser beam will be labelled as vertical or horizontal (perpendicular or parallel to the surface of the optical table, respectively) and s and p nomenclature will be used when referring to the droplet surface.

This decomposition into $s-$and $p-$polarization and the resulting absorption profiles can be analytically derived. Figure 3.7 shows the profiles of the absorbed energy on the droplet, for both linear and circular polarization. This calculation follows the procedure described above, assuming an 80 μm FWHM Gaussian beam incident on a droplet with a radius of 15 μm (left) and 23 μm (right).

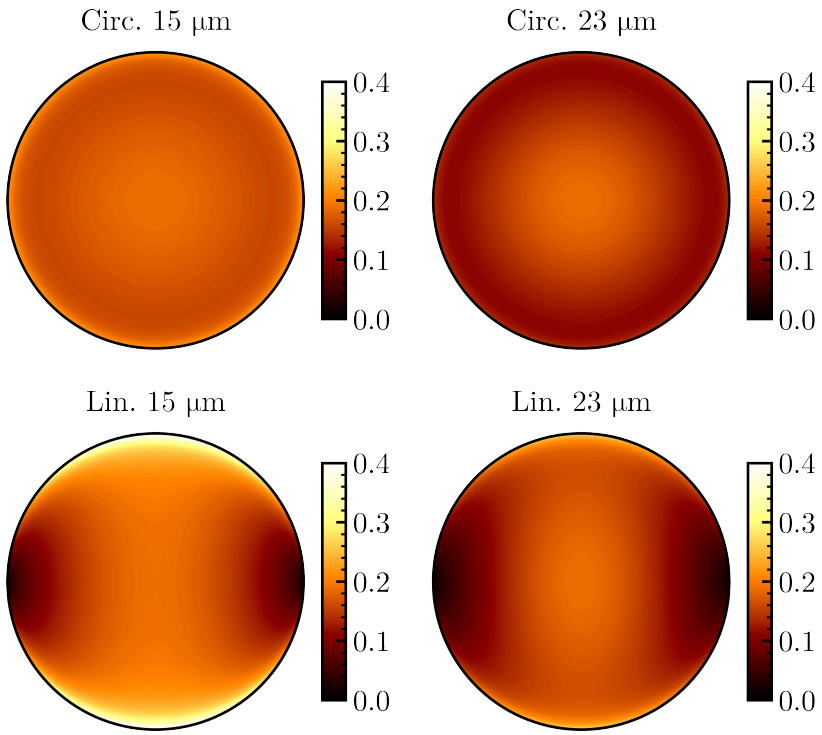

Figure 3.7: Absorption coefficient mapped onto the laser-facing surface of a spherical droplet, for linear and circular incident laser polarization. The beam is taken to have a 2D Gaussian spatial distribution with an 80 μm radius (FWHM) for all cases. The droplet radius is indicated above each profile.

The most noteworthy feature in the absorption profile for linear polarization is the clear cylindrical symmetry breaking, featuring zones of high and low absorption at edges along and opposite to the polarization axis, respectively.

When using linearly polarized pulses incident on tin droplets, the resulting absorption inhomogeneity produces drastic changes in the droplet expansion and in the shapes of the spall and ablation front, as shown in Fig. 3.8. In this figure, shadowgraphs at different time delays are shown for circular, horizontal and vertical polarizations, respectively. The pulse duration is 220 fs, and the incident energies are 5 mJ and 1 mJ (Fig. 3.8a,b, respectively). As rotating a linear polarization is analogous to rotating the angle of observation of our 90-degree shadowgraphy system, the shadowgraphs for vertical and horizontal

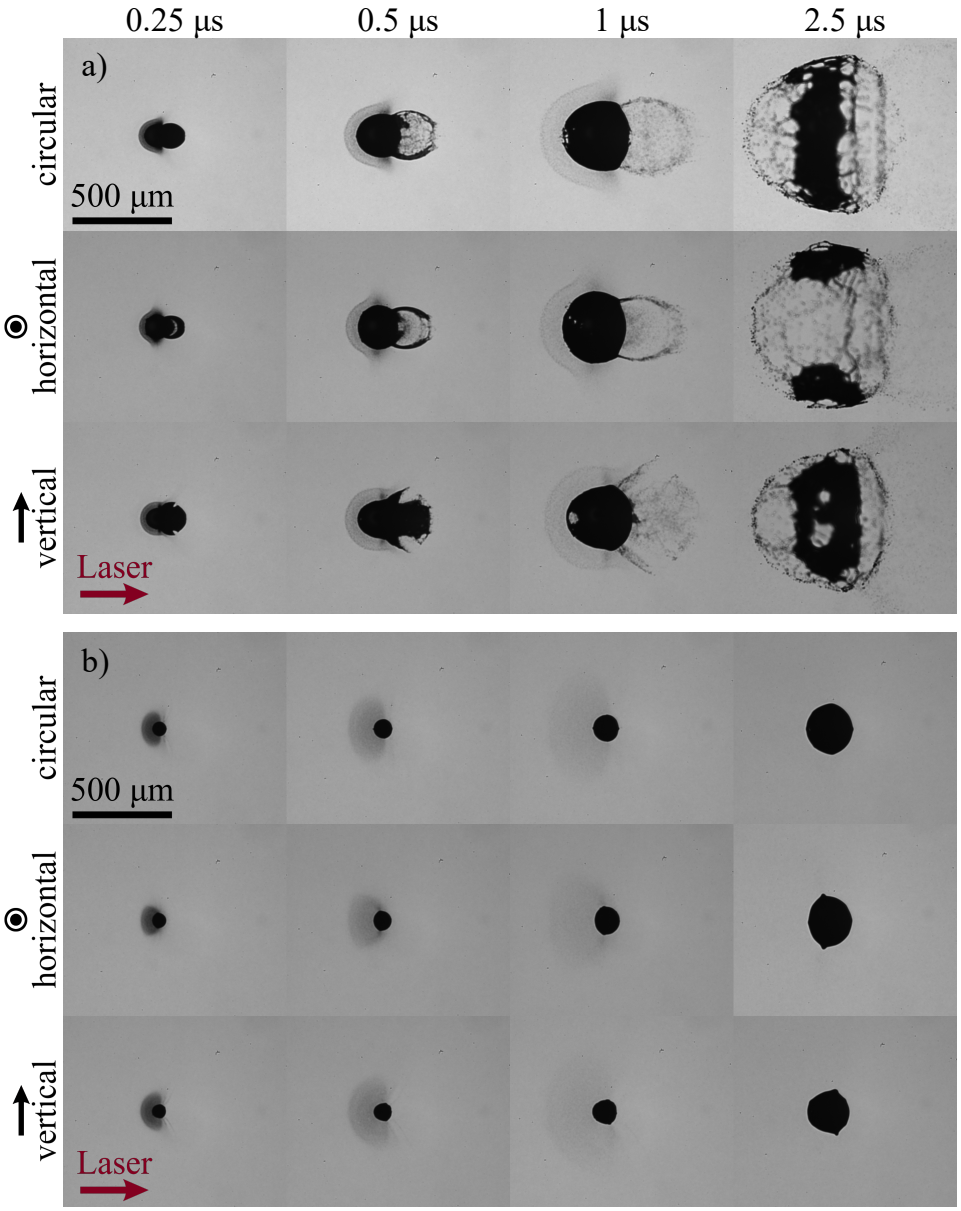

Figure 3.8: Effects of laser polarization on droplet expansion at various delays after laser irradiation, for laser energies of 5 mJ (a) and 1 mJ (b). Pulse duration of 220 fs for all cases. The polarization state is indicated on the left of each row. Initial droplet radius: 23 µm, laser spot size: 80 µm (FWHM).

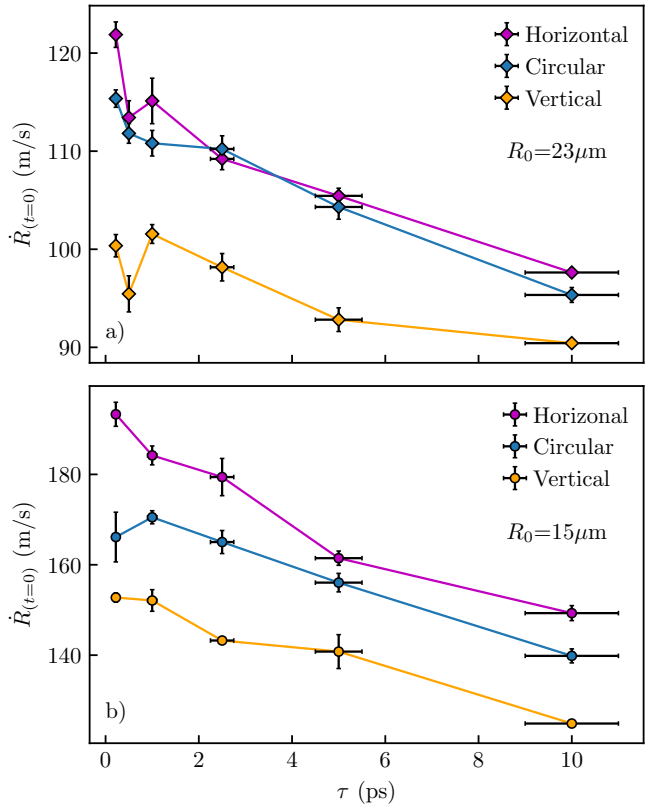

Figure 3.9: Cavitation expansion velocity for different polarizations for droplets with $R_0 = 23$ µm (a) and $R_0 = 15$ µm (b). Pulse energy of 5 mJ for all cases.

incident polarization can be visualized as the side- and top-view of the same structure.

In these shadowgraphs, differences were observed in the ablation front angle, expansion speed of the cavitation shell, as well as shape of the spall. These differences exist at both energies, but become more apparent in the higher-energy measurements. The low-energy data in Fig. 3.8b highlights the different opening angles of the ablation front, which clearly follow the expected absorption profiles (Fig. 3.7). For the vertical polarization, there is a Brewster's angle and thus maximum absorption near the top and bottom of the droplet as seen in the side-view shadowgram, which results in a nearly hemispherical ablation front. For the horizontal polarization, the absorption mostly decreases towards

higher angles, resulting in a more backward-directed ablation front. For circular polarization, the ablation front is cylindrically symmetric and shows an angle in between the different horizontal cases. At higher energy (Fig. 3.8a) these asymmetries become somewhat less apparent because of the increased influence of plasma pressure, but a clear difference in shape of the ablation front is still observed.

At high energy, a marked difference is also observed in the spallation front. As discussed above, spallation occurs when a laser-induced shock wave arrives at the back surface. The initial spatial profile of the shock wave is determined by the local light absorption. After being focused at the center of the droplet and diverging upon further propagation, its spatial profile at the back surface closely follows the initial absorption-driven distribution.

Similar to what is observed for ablation, linear polarization leads to a striking asymmetry in the spallation process. In the plane perpendicular to the polarization direction, the spallation occurs over a limited angular range and is largely forward-directed. In contrast, in the plane parallel to the polarization direction a much larger angular spread is observed, with sharp lobes near the poles where the light absorption profile was highest.

The expansion speed of the cavitation shows the opposite trend, as the shell expands faster in the plane perpendicular to the input polarization and slower in the parallel plane. Nevertheless, at longer delay time (2.5 μs) it can be seen that there is more material expanding perpendicularly to the polarization plane. When a pressure wave propagates from the surface of a sphere towards its center, a larger angle at the surface leads to a tighter focus at the center of the sphere [23]. When the initial pressure profile is elongated along a given axis, the resulting focus will be elongated in an orthogonal direction, leading to an asymmetric initiation of the cavitation process.

Despite the asymmetric conditions, the expansion speed of the cavitation shell continues to be well represented by a power-law of the form $\dot{R}(t = 0) \times R_0 = A \times E^{\alpha}$, both in the direction parallel and perpendicular to the laser polarization.

Fig. 3.9 compares the cavitation expansion for all polarizations studied, for both droplet radii, as a function of pulse duration for a 5 mJ pulse. The observed asymmetry is found to show a significant decrease with increasing pulse durations. Comparing the expansion velocity of the cavitation shell in the parallel and perpendicular planes for 23 μm droplets, an asymmetry of 19.4% was measured for 220 fs pulses, which decreases to 7.6% for 10 ps. For 15 μm

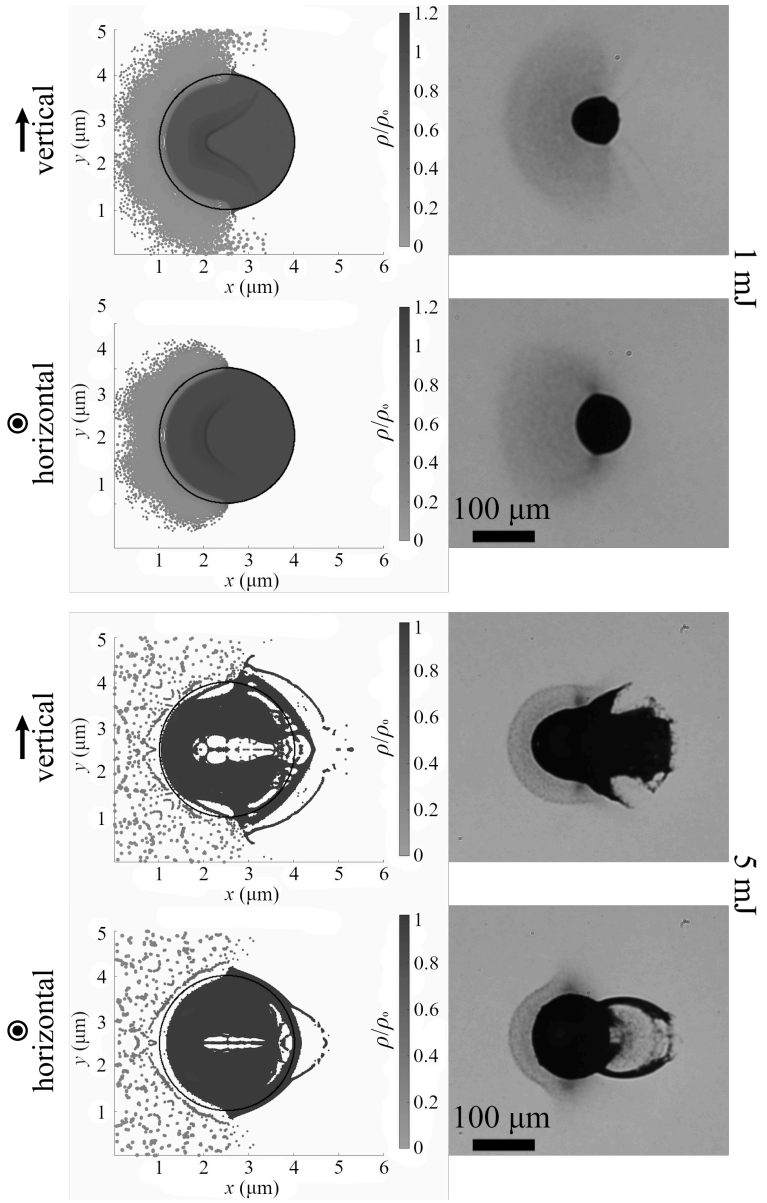

Figure 3.10: Comparison between SPH simulations (left) and experimental shadowgraphy images (right). There is a good agreement between the predicted and observed angular extension of the ablation area. A more confined spall is observed for horizontal polarization, as well as structures that resemble the "winglets" for vertical polarization. These simulations cannot account for an expanding cavitation shell (see text). Note the change in scale.

droplets, this decrease is lower, going from 23.4% for 220 fs pulses, to 17.8% for 10 ps.

This effect can again be explained through the increased influence of plasma formation towards longer pulse durations. As soon as a dense plasma is present in front of the droplet, the absorption increases strongly and is much less sensitive to polarization and angle of incidence compared to liquid tin droplets [93, 94]. So once this plasma layer is formed, its absorption profile will thus be cylindrically symmetric. Energy transfer into shock waves can still occur, as strong cavitation and spallation are still observed even for much longer pulses, but the resulting shock wave and subsequent deformation dynamics will become much more symmetric compared to the case where plasma absorption is not yet dominant. The asymmetry is more pronounced for smaller droplets, which can readily be explained by the increased influence of the asymmetric absorption as shown in Fig. 3.7.

To aid in the understanding of the observed dynamics, smoothed-particle hydrodynamics (SPH) simulations were employed, using an in-house developed two dimensional SPH code following established methods [95, 96]. In SPH, three conservation laws are solved, namely, the continuity equation (conservation of mass), the conservation of particle momentum and the conservation of energy:

$$\frac{D\rho}{Dt} = -\rho\nabla\cdot\mathbf{v} \tag{3.1}$$

$$\rho\frac{D\mathbf{v}}{Dt} = -\nabla p \tag{3.2}$$

$$\rho\frac{De}{Dt} + p\nabla\cdot\mathbf{v} = Q, \tag{3.3}$$

where D is the convective derivative, ρ is the mass density, $\mathbf{v}$ is particle velocity, p is the pressure, e is thermal energy density of the particles, and Q is the source term. The source term describes the increase in the total energy of the system due to the spatially dependent absorption profile of the laser pulse, calculated using the Fresnel equations, as well as the known spatial profile of the laser (Fig. 3.7). The temporal shape of the source term is further supplemented with the modeling of energy transfer from electron to lattice via the two-temperature model [97, 98]. In the simulations, the Mie-Grüneisen equation of state for liquid tin is used, following Ref. [86]. The simulations are performed with a circular tin droplet of 3 µm diameter. Due to the limited computational resources, simulation of the same droplet size as the experiment is impractical. However,

hydrodynamic similarity [86] indicates that the dynamics for different droplet sizes are qualitatively similar. Thus, for a qualitative comparison, a smaller droplet size is sufficient.

Fig. 3.10 shows the experimental simulation results in comparison with the experimental data. While the simulations are performed in a 2D geometry and do not account for the influence of plasma, similar trends are observed as seen in the experiment. This agreement provides additional evidence that the spatial distribution of the initial shock wave is the defining parameter for the non-cylindrically-symmetric dynamics. Both the ablation front and spall are more confined in the direction perpendicular to the input polarization and wider along the polarization direction, when compared to circular polarization case. It should be noted that in a 2D geometry, cavitation effects are expected to be underestimated due to the lower ratio between surface area and focal volume in a 2D geometry compared to a more realistic 3D case. However, ablation and spallation are mainly determined by the local shock wave at the droplet surface, which can be expected to show similar behaviour in 2D and 3D models. Therefore, only qualitative agreement is sought in this simulation effort, and especially the shape of ablation and spallation fronts are to be compared here.

3.4 CONCLUSIONS

The effects of pulse energy and duration on the shock-wave-driven expansion dynamics of liquid tin microdroplets irradiated by ultrashort laser pulses have been reported in this work. The initial cavitation expansion velocity as well the velocity of the ablated material are found to decrease as a function of pulse durations, in situations where the pulses are sufficiently intense to produce significant plasma density. Using linearly polarized laser pulses, non-symmetric shock waves were produced in the droplets, leading to non-symmetric droplet deformation dynamics and uniquely shaped targets. Lastly, 2D SPH simulations show a qualitative agreement with the experimental results, highlighting the role of shock waves in the laser-driven deformation dynamics, and indicating that the non-cylindrically-symmetric pressure wave launched from the surface is the main factor for the observed behaviour. The present work further clarifies the influence of ultrashort laser pulses on liquid droplet deformation, and demonstrates a route towards improved control over target pre-shaping in next-generation LPP sources for EUV generation.

4

CONTROLLING ION KINETIC ENERGY DISTRIBUTIONS IN LASER PRODUCED PLASMA SOURCES BY MEANS OF A PICOSECOND PULSE PAIR

The effect of a pair of picosecond pulses on the ionization and deformation of a liquid tin microdroplet is studied for a range of incident pulse parameters. Faraday cups are used to measure ion kinetic energy distributions, together with high-resolution shadowgraphy to monitor target deformation and expansion. It is found that the introduction of a relatively weak first pulse results in an order-of-magnitude reduction of the number of ions with kinetic energies above 1 keV, and a strong shift of the kinetic energy distribution towards lower energies, while the expansion dynamics of the droplet can be kept similar to the single-pulse case. By controlling the relative intensity and the time delay between pairs of pulses with 52 ps duration, regimes are identified in which spherical final target shapes are combined with a reduced high-energy ion yield. The high-energy part of the observed ion distributions has been fitted with a self-similar expansion model, showing a 30-fold decrease in characteristic ion energy for pulse pairs. This combination of results is of particular importance for plasma sources of EUV radiation for nanolithography applications, in which picosecond laser-produced target shapes can lead to significant improvements in source conversion efficiency, while a low high-energy ion yield is desirable from a source lifetime perspective.

This chapter has been published as [43].

4.1 INTRODUCTION

The next generation of lithography machines uses extreme ultraviolet (EUV) light at a wavelength of 13.5 nm. In the past two decades, many theoretical and experimental studies have been conducted on possible light sources for EUV lithography [12], including synchrotron radiation [99, 100], free-electron lasers [101, 102], plasma sources [103–107], and high-harmonic generation [108].

From the aforementioned solutions, a tin-based laser-produced plasma (LPP) source received the most attention due to its high conversion efficiency, robustness, and scalability [109, 110], resulting in a first commercial machine launched in 2010. In such an LPP source, a small tin droplet is ionised by an intense laser pulse to emit the requested light at 13.5 nm. Narrowband radiation around 13.5 nm comes from multiple ionic states [111, 112], Sn^{8+} to Sn^{14+}, collisionally excited by plasma electrons heated through interaction with a powerful CO_2 laser. An effective coupling between laser light and plasma occurs near the critical density, which for the CO_2-laser-driven plasma is around 10^{19} cm^{-3}. At the same time, the size of the EUV source cannot be too large to match the requirements toe the maximum etendue [9]. Precise control of the target shape is thus crucial for the production of EUV light in an industrial setting, and numerous irradiation schemes have been explored with the aim of optimizing conversion efficiency (CE).

Expansion of the target can be achieved by deforming the tin droplet with a pre-pulse generated either by the same CO_2 laser system [14, 113] or by a separate laser, typically Nd:YAG [22, 25, 46, 114–116]. The latter solution reduces the amount of backscattered light and, by decoupling both laser systems, prevents instabilities and potential damage to the lasers, at the expense of added complexity in the EUV lithography machine. The interaction between a tin droplet and a nanosecond pre-pulse leads to the generation of a high-density disk target and results in a reported conversion efficiency of 4.7% [117]. Alternatively, a picosecond pre-pulse could be employed that expands the droplet to a low-density diffuse target resembling an acorn [11, 118], and is associated with higher CE up to a maximum reported value of 6% [12].

Due to the interaction with intense laser pulses, the source emits large amounts of energetic particles. From these debris, the ions with kinetic energies of several keV are particularly undesirable, as they may damage the nearby multilayer mirror that collects the light emitted by the plasma, reducing its reflectivity and thus limiting its lifetime [108]. This issue is particularly

relevant when using picosecond-duration pre-pulses, which are associated with an increase in the emission of ions with multi-keV energy [119]. To mitigate the impact of ion debris, several techniques have been introduced including: stopping fast ions using a buffer gas [26, 27], guiding them away to a "dump" using a magnetic field [28], or a combination of both [29].

Alternatively, it may be possible to control the physical mechanism responsible for the acceleration of the produced ions to the observed high velocities. Some prior studies hint towards the feasibility of such an approach. For example, in experiments on solid tin and gadolinium targets [120, 121], the ion energy distributions were shifted significantly towards lower energy values. This substantial reduction of ions kinetic energy was achieved by using a pulse pair comprising a weak picosecond pulse at different wavelengths (1064 nm, 532 nm, or 355 nm) followed by a strong nanosecond pulse at 1064 nm. Recently, a similar observation has been made on droplets in a double pulse irradiation scheme comprising a 7.5 ns Nd:YAG pulse with an energy of 48 mJ followed by a 600 mJ CO_2 pulse [122]. A maximum reduction in the ion average kinetic energy by a factor of 3 was observed by delaying pulses by 164 ns.

The aforementioned experiments addressed on the influence of a plasma generated by the first pulse (pre-pulse) on the ion energy distribution originated by the second pulse (main pulse). However, in the industrially relevant case, the pre-pulse is employed to fluid-dinamically transform the droplet into an optimal target shape for high-CE LPP sources. It is an open question if multi-pulse schemes can be developed that reduce the amount of high-energy ions while still producing the optimum target shape. In this chapter, we address the use of a carefully designed picosecond pulse pair as a pre-pulse to reduce the amount of fast ions and additionally to transform the droplet into the preferred acorn-shaped target.

4.2 EXPERIMENTAL SETUP

The experimental setup, shown in Fig. 4.1, comprised a tin droplet generator operated at approximately 37 kHz repetition rate resulting in 30 *micro*m diameter droplets, as described in further detail in Chapter 2. The droplets were irradiated with a picosecond pulse pair, produce by the Nd:YAG system also described in Chapter 2. The pulse duration was measured using a home-built autocorrelator and set to 52 ps. The energy of the pulse pair was controlled by a half-wave plate and thin film polarizer (TFP) combination. The energy of the

second, stronger pulse was kept constant at 5 mJ while the energy of the first pulse was varied between 0 and 500 μJ. Before entering the target chamber, a quarter-wave plate sets a circular polarization and a 600 mm plano-convex lens focuses the beam to 135 μm ($1/e^2$) at the position of the droplet. To measure the ion kinetic energy distribution, two commercial Faraday cups (FCs) (Kimball Physics, model FC-73A) were mounted at 30° and 62° with respect to the incident laser beam [50, 123], allowing for charge yields down to 10^{-4} $\mu C keV^{-1} sr^{-1}$ can be detected for 10 keV ions.

The evolution of tin droplets after the interaction with the pulse pair was recorded using time-resolved shadowgraphy. Two temporally and spatially incoherent, 5-ns-long pulses at 560 ± 10 nm wavelength illuminate the droplet in the horizontal plane at 30° and 90° along the laser propagation axis. The backlit droplets are imaged by CCD cameras equipped long-distance microscopes positioned opposite to the light sources at 150° and 270°, allowing for a side and back view respectively.

4.3 RESULTS AND DISCUSSION

Fig. 4.2 shows a series of shadowgraphs, demonstrating the effect of picosecond pulses on droplet deformation and expansion, 550 ns after the second laser pulse incides on the droplet. Fig. 4.2(a) shows a typical acorn-like shape of a droplet deformed with a single 52 ps pulse (5 mJ), composed of two unequal conjunct spheroids results from shock wave propagation [25, 46].

When an ultrashort laser pulse (<1 ns) irradiates a tin droplet, the energy is absorbed in a thin layer near the surface. This rapid energy deposition gives rise to a hemispherical shock wave which focuses inside the droplet, leading to cavitation and the creation of the shell on the front side (right side of the images). The second shell on the rear (left on the images) side results from the spallation effect caused by the shock wave reflected at the back surface.

When the same 5 mJ picosecond pulse is preceded by a weak pulse, the droplet shape changes noticeably. Even a low energy 25 μJ pulse (only 0.5% of the energy of the second pulse), preceding the second pulse by 10 ns produces a noticeable effect due to plasma push, reducing the target expansion by 20% along the laser axis (Fig. 4.2(h)). By doubling the energy in the first pulse to 50 μJ and keeping the time delay at 10 ns, more plasma is being generated, which surrounds the droplet and appears to limit its expansion at the backside as well as in the vertical direction (Fig. 4.2(b)). For this compressed target, a significant

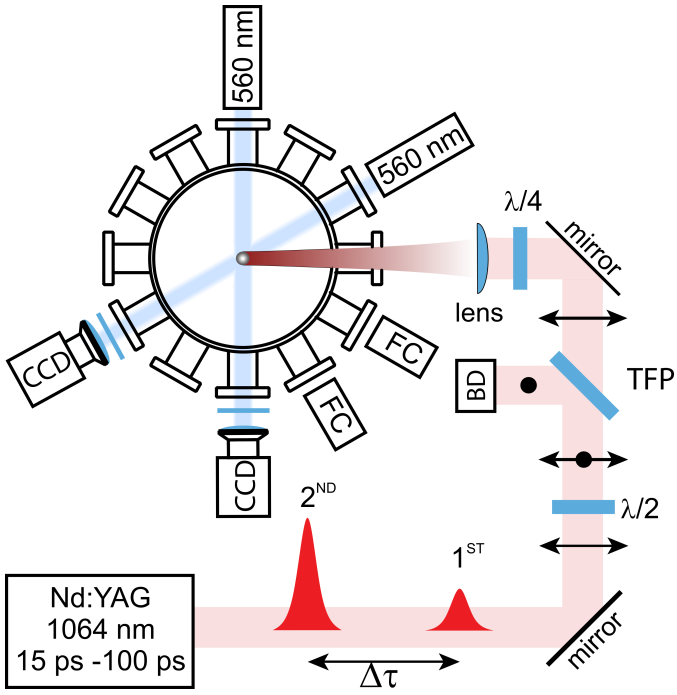

Figure 4.1: A schematic representation of the experimental setup. A ps pulse pair is generated in a home-build Nd:YAG laser system with a controllable pulse duration (15 ps-100 ps) and a delay time $\Delta\tau$ between two pulses tunable from 0 to 1000 ns in increments of 10 ns. The pulse pair energy is set by means of a half-wave plate ($\lambda/2$) in combination with a thin film polarizer (TFP) and a beam dump (BD). Prior to entering the vacuum chamber, the polarization of the pulses is changed into circular with a quarter-wave plate ($\lambda/4$) and a convex lens (f = 600 mm) focuses pulses on a 30 µm tin droplet leading to the generation of plasma. The resulting ions are detected in time-of-flight measurements with Faraday cups (FC) positioned at 30° and 62° with respect to the laser plane. The time evolution of the droplet is captured on shadowgraphs obtained with two CCD cameras (at 90° and 150°) illumined by 560 nm light.

reduction in spallation is observed. This may be particularly beneficial for use in LPP sources as such spalling is detrimental for machine lifetime. For longer time delays, the plasma expands and its density reduces, enabling it to again spread more in the vertical direction (Figs.4.2(c) and 4.2(d)). Assuming a spherical plasma expansion at constant velocity, the reduction of density for an

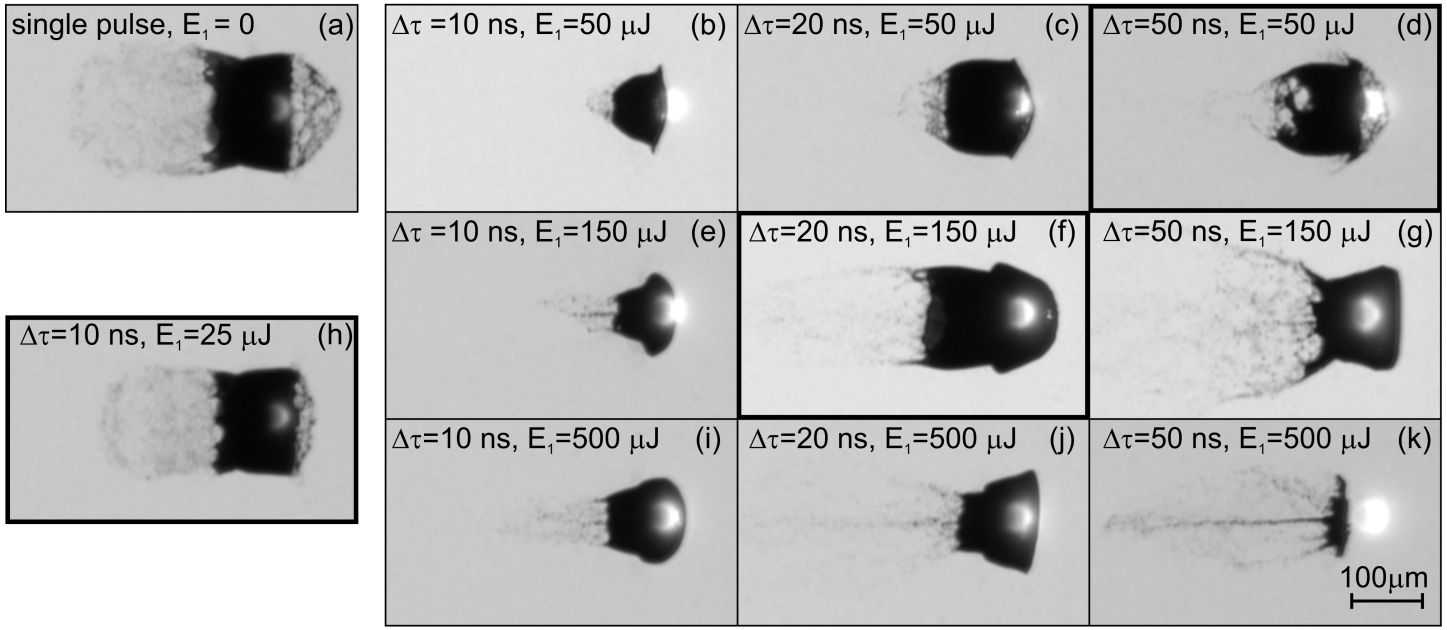

Figure 4.2: Shadowgraphs showing the evolution of a 30 μm-diameter tin droplet 550 ns after the interaction with a single pulse or a pulse pair for several typical parameter settings. The laser light hits the droplet from the right side and the bright spot is plasma light is captured by a camera due to the long exposure time. (a) A 52 ps single pulse with an energy of E_2=5 mJ. (b)-(d) A 52 ps pulse pair at various delay times $\Delta\tau$ with the 1st pulse energy set at E_1=50 μJ and the 2nd pulse energy fixed at E_2=5 mJ. (e)-(g) The same as (b)-(d), but with E_1=150 μJ. (h) A 52 ps pulse pair with a minimum energy in the 1st pulse of E_1=25 μJ, delayed by 10 ns with respect to the second pulse with an energy of E_2=5 mJ. (i)-(k) The same as (b)-(d), but with E_1=500 μJ. The images highlighted with a thick frame [(d), (f), and (h)] resemble a typical acorn-like shape for which the highest CE has been reported [12]. The scale bar on the bottom right holds for all panels in this figure.

increase in time delay from 10 ns to 50 ns is about two orders of magnitude. For time delays longer than 200 ns, the target shape reverts back to the acorn-like shape, except at the front side which stays flat as a result of a plasma generated by parasitic pulses present in the pulse train due to limited contrast of the laser setup for time delays $\Delta\tau > 100$ ns.

When the energy in the first pulse is further increased, no additional compression of the target is observed. In contrast, shadowgraphs taken after a 10 ns delay show expansion in the direction of the laser light (Figs. 4.2(e) and 4.2(i)). A possible explanation to this observation is an increasing shift of the position of critical density away from the droplet in the direction of the laser pulse, as the energy of the first pulse increases. Consequently, the laser light from the second pulse generates plasma further away from the target, leading to a larger expansion of the droplet in the laser direction. A similar explanation may be used to describe the flattening of the target's front, which is visible in Figs. 4.2(g) and 4.2(j). By increasing the time delay beyond 10 ns, the plasma generated by the first pulse has more time to fade away and the position of critical density shifts back to the vicinity of the droplet. Thus, the second pulse produces plasma closer to the droplet, which experiences a stronger push at the front.

Different combinations of the first pulse energy (E_1) and time delay between the pulses ($\Delta\tau$) result in diverse target shapes. Nevertheless, shadowgraphs in Fig. 4.2 marked with a thick frame [i.e., images (d), (f), and (h)] reveal the close resemblance of some of these target shapes to the original acorn-like shape. However, as will be discussed below, the ions produced by these pulse pairs have significantly lower kinetic energies.

Figure 4.3(a) shows the total charge collected by the 30° FC for different pulse pair combinations, calculated according to

$$\frac{dQ}{d\epsilon} = \frac{t^3}{mL^2} \cdot \frac{I(t)}{\Omega X} \tag{4.1}$$

where t is the time-of-flight, $I(t)$ is the ion current obtained by correcting the measured voltage signals for the response function of the read-out network [50], m is the mass of tin, L is the time-of-flight distance, Ω is the solid angle, and X is the FC grid transmission. As a reference, measurements were taken using a single 5 mJ, 52 ps pulse (black symbols). The colored symbols correspond to measurements with pulse pairs for varying energy in the first pulse and a fixed delay of 10 ns. Remarkably, in the case of a pulse pair in which a first pulse

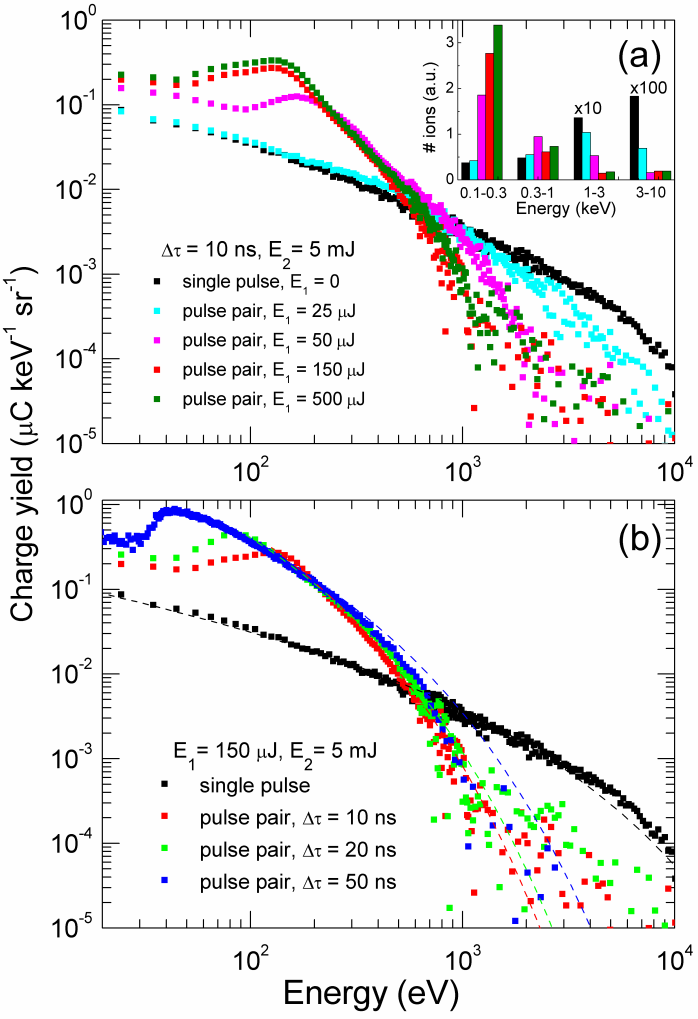

Figure 4.3: (a) Charge energy distributions measured by the 30° FC resulting from the ablation of a tin droplet by a single 5 mJ, 52 ps pulse (black symbols), and by 52-ps-duration pulse pairs delayed by 10 ns for various energies in the first pulse (E_1) and fixed second pulse energy E_2 = 5 mJ (colored symbols). The inset shows the total ion charge obtained by integrating the energy distributions shown in (a) in four energy ranges. (b) The effect of different time delays $\Delta\tau$ between the two pulses on ion energy distributions (colored symbols) compared to the single pulse case (black symbols). The dashed lines are analytical fits to the distributions according to Eq. 4.1.

with only 25 μJ precedes the stronger 5 mJ pulse (cyan symbols), the ion energy spectrum already shifts towards lower energies and the measured ion current in the 3-10 keV range decreases by roughly 35% compared to the single pulse case. For E_1 = 500 μJ (green symbols), the spectrum changes even more and the measurements show a one order of magnitude reduction in the ion current for kinetic energies above 3 keV. However, the effect seems to saturate for values of E_1 greater than 150 μJ (red symbols), where the maximum reduction in ion current for kinetic energies above 1 keV is observed. In contrast, the ion current at low energies in the 100-300 eV range increases by one order of magnitude, and by a factor of 1.3 in the 0.3-1 keV range. This growth can be explained by a geometric effect due to the mismatch between the laser beam diameter (135μm) and the tin droplet diameter (30 μm). The first pulse interacts with the droplet and generates a plasma which expands well beyond 30 μm within 10 ns, resulting in a larger target interaction area for the second pulse. Therefore, to induce a significant shift to the ion kinetic energy distribution, the first pulse needs to create a sufficiently dense plasma. Fig. 4.3(b) shows that keeping constant energies in both pulses, here E_1 = 150 μJ and E_2 = 5 mJ, and increasing the second pulse delay does not lead to further reduction in ion kinetic energy. Instead, it results in an increased current at lower kinetic energies.

In the single pulse case, the ion energy distribution can be explained by a self-similar model of free plasma expansion into a vacuum based on a hydrodynamic approach [77, 124]. The applicability of this model for ion spectra resulting from an adiabatiacally expanding plasma has been verified by Bayerle *et al.* [50]. The model assumes that initially a plasma occupies the half-space x<0, and that the ions are cold and at rest with a step density function, whereas the electrons obey a Boltzmann distribution. Once the plasma starts to expand, the ions are accelerated in the electrostatic potential and the number of ions per unit energy and unit surface is given by [77]

$$\frac{dN}{dE} = (n_{i0} C_s t / \sqrt{2\epsilon\epsilon_0}) \exp(-\sqrt{2\epsilon/\epsilon_0}) \tag{4.2}$$

with n_{i0} being the initial ion density, C_s the ion-acoustic velocity, and ϵ_0 the characteristic ion energy related to the electron temperature T_e via $\epsilon_0 = Z k_B T_e$, where Z is the ion charge number and k_B the Boltzmann constant. As already found in previous work [50], a fit to a self-similar expansion model that takes into account the dimensionality of the target [78] did not lead to significant improvements in the fit quality.

The dashed black line in Fig. 4.3(b) shows the fit of the kinetic energy spectrum to Eq. 4.2 for the single pulse case. According to the model, the plasma produced by a 52 ps single pulse at 5 mJ leads to the generation of ions with a characteristic energy ϵ_0 = 990 (50) eV. The energy spectra recorded for pulse pairs show a non-monotonic decay for the low-energy part of the spectrum with a maximum which shifts towards lower energies when increasing the time delay between two pulses. This clearly points towards a more complex physical picture than the self-similar model provides. Nevertheless, this simplified approach can still be successfully used to describe the high-energy part of the spectrum, beyond the observed maxima. These fits, shown as coloured dashed lines in Fig. 4.3(b), reveal that the characteristic energy is the lowest for a delay of 10 ns and has a value of ϵ_0 = 34.5 (0.9) eV, which is 30 times smaller than the single pulse measurement. Lower characteristic energy values for pulse pairs hint at lower electrons temperatures or ion charge state, compared to the single pulse case. As will be shown in Chapter 6, irradiation by a pulse pair results in a significantly different charge state distribution compared to the single pulse case. The most significant differences being an increase of the relative abundance of lower charge states (1+ and 2+) and a decrease for higher charge states, as well as lower most probable kinetic energies (MPKE) across all charge states.

With a single pulse, the laser light mainly interacts with the droplet and, due to its high density, is absorbed within a thin layer, leading to the generation of a hot plasma and consequently the ejection of fast ions. For a pulse pair, the first weak pulse ablates material from the droplet and the second pulse will therefore interact with this plasma as well as with the droplet. This second pulse will then be absorbed across a thicker layer, resulting in a colder plasma in which the ion kinetic energies are lower than in the single pulse case.

The reduction in kinetic energy and average charge state are both favourable factors for ion mitigation using a static buffer gas, which is more effect for lower charge states [125], and any potential shift in the charge state composition for pulse pair interaction is expected to be towards such lower charge states [126].

4.4 CONCLUSIONS

The presented experimental results on laser-produced tin plasmas demonstrate that by employing a picosecond pulse pair instead of a single pulse, it is possible to greatly shift the ion kinetic energy distribution towards lower energies. Re-

duced kinetic energies make mitigation of the generated ions in LPPs by means of collisions with an ambient gas much more efficient [125, 127]. By matching the laser beam size with the droplet size, further reduction in the number of fast ions should be achievable. Simultaneously, the recorded shadowgraphs showed that a picosecond pulse pair enables the tailoring of the target shape. Depending on the combination between the energy in the first pulse and a time delay between both pulses, it is possible to obtain shapes similar to an acorn-like target, which in the interaction with a CO_2 main pulse may lead to a higher conversion efficiency into EUV light through the opening up of a larger parameter space for optimization.

5

ENERGY- AND CHARGE-STATE-RESOLVED ION SPECTROMETRY OF FS- AND PS-LASER-PRODUCED TIN PLASMA

In this chapter, we report on the charge-state distributions of ions emitted from tin LPPs created by ultrashort pulses with durations between 220 fs and 10 ps, both in flat solid targets and liquid microdroplets.

The charge-state-resolved energy spectra are largely independent of the laser pulse duration in the range reported, indicating that the timescales of ion acceleration in the observed regime are either shorter than 220 fs or longer than 10 ps. The reported energy spectra hint at processes beyond a simple model of ion acceleration driven solely by an electrostatic field created by electrons ejected by the laser pulse.

It was also found that, for droplet targets, longer pulses lead to higher yields of higher charge-state ions and a higher average charge state. For solid targets, the ion abundance distributions and average charge state were found to be independent of pulse duration. This difference may be attributed to differences in the plasma expansion dynamics between the solid and droplet targets.

5.1 INTRODUCTION

As was discussed in Chapter 3, irradiating tin microdroplets with laser pulses with durations between 0.2 and 10 ps results in violent shock-wave-driven cavitation and spallation dynamics, very different to what is observed when droplets are illuminated with ns pulses [79]. These violent processes lead to highly dispersed, cloud-like density distributions which recent works suggest could be favourable for EUV generation, when used as a target for a second more energetic ns pulse that drives the subsequent plasma generation and EUV emission [11, 12].

The differences between LPPs created by ns and fs-to-ps pulses extend into other aspects of the system, with the kinetic energy and charge state distributions of the ion emissions expected to be different between the two regimes [31]. As was mentioned in Chapter 4, in LPP-based EUV light sources it is important to minimize the amount and energy of these emitted ions, as they may damage the nearby collector mirror, reducing its reflectivity and limiting its lifetime [108]. While some of these ions can be mitigated with active techniques, such as buffer gases or magnetic diverters, these approaches become less efficient for more energetic ions. As such, studies on the ion energy and charge-state distributions are a key complement to the studies on target deformation to offer a more complete picture of the laser-droplet interaction as a whole.

5.2 CHARGE-STATE-RESOLVED ENERGY DISTRIBUTIONS

Various studies of ion emission from LPPs utilise ns pulses and observe that the average kinetic energy of ions of each charge state is proportional to the charge state [36, 39, 128]. This is explained as the consequence of charge separation, as electrons are ejected from the target material after absorbing laser photons. In this picture, an electrostatic field is created between the electron front and the net-positively-charged target. This field is proposed as the dominating factor defining the energy distribution of keV-level ions emitted by LPPs. However, recent experiments have shown results different from the simple linear dependence of the ion energy on charge state, hinting at more complex processes [33, 34, 40].

Ion emission from laser-produced plasmas driven by lower energy pulses relevant to EUV generation has not been thoroughly studied using charge-state-resolved measurements. There have been few charge-state-resolved studies

using femto- and picosecond pulses [40], with some authors applying the assumption of linear relation between energy and charge state from experiments with ns pulses to experiments with ultrashort pulses [41, 42].

While the energy transfer between the laser pulse and subsequent electron thermalization happen at electron-electron coupling timescales (on the order of several femtoseconds), the energy transfer from the electrons to the ions happens at electron-phonon coupling timescales, which for tin are in the range of few to tens of picoseconds [32]. For this reason, one would expect differences in the charge-state distributions between the case where the pulse duration is much longer than the electron-phonon coupling timescale, and the case where they are comparable. This is because in the former case, the laser pulse is still depositing energy in the system after the ion emission is underway, resulting in the laser energy being partially absorbed by the plasma (ions), rather than interacting with neutral, liquid tin. In the latter case, the laser energy deposition rate into the target varies greatly on timescales comparable to the processes that shape the energy distribution of the emitted ions and, for short enough pulse durations, the laser pulse could have ended by the time a significant amount of plasma is formed.

5.3 EXPERIMENTAL SETUP

Fig. 5.1 shows the experimental setups. In both cases the laser pulses are produced by the fs OPCPA described in Chapter 2. The pulse duration is varied between 220 fs and 10 ps by changing the grating separation in the pulse compressor, while the pulse energy is adjusted using a half-wave plate and thin-film polarizer combination. Lastly, a quarter-wave plate is used to set a circular polarization and, in both cases, the beam is focused to a Gaussian spot with a diameter of 80 μm (FWHM), using a 500 mm focal length plano-convex lens.

In the case of the liquid target, the droplet generator was configured as described in Chapter 3, as these results were obtained as part of the same experimental campaign. Tin (99.995% purity) is heated to 260 °C, above its melting point of 232 °C, inside a tank mounted above the vacuum chamber. The tank is pressurized with argon and the liquid tin is expelled through a 6.5-μm nozzle containing a piezo element driven at 10.2 kHz, producing a steady stream of 23-μm radius droplets. The droplets pass a horizontal light sheet produced by a helium-neon laser, with the scattered light being recorded

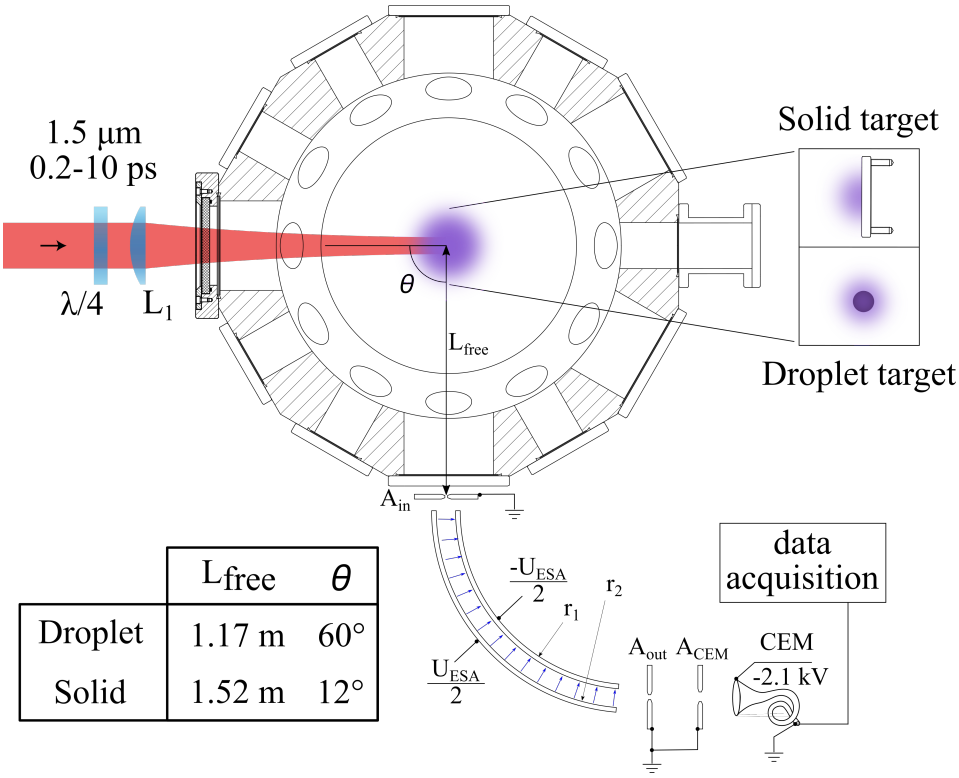

	L_{free}	θ
Droplet	1.17 m	60°
Solid	1.52 m	12°

Figure 5.1: Diagram of the experimental setups. The insets show the different target configurations. The ESA is shown mounted at 90° for clarity, but values of θ are indicated in the inset table, as are the values of L_{free}.

by a photomultiplier tube. This signal is used to trigger the laser system and the ion energy diagnostics at a reduced repetition rate of 10 Hz, timing it with the correct droplet in the stream to create a laser-produced plasma at the center of the vacuum chamber.

For the solid target setup, an introductory overview was presented in Chapter 2. Solid 1 mm-thick targets of 99.99%-purity tin are placed at the center of the vacuum chamber. Each target is divided in a grid of shot positions, spaced horizontally and vertically by 1 mm, such that each position is unaffected by the laser interaction with adjacent positions. The target holder is mounted on a translation-rotation stage, with target position being automatically controlled by an in-house designed control software: *Spanish Inquisition*. The software further controls trigger signals and data acquisition.

For the measurements presented in this chapter, each target position was irradiated 15 times. As each position is repeatedly irradiated, material is ablated from the sample, creating an increasingly large crater which changes the geometry of the target. The number of shots was chosen in order to maximize the amount of data points collectable from each sample and minimize experimental downtime due to sample swapping, while ensuring that the data is not significantly affected by the geometry change.

Not previously mentioned is the electrostatic analyzer (ESA), the device used to obtain the charge-state-resolved spectra presented in this chapter. A thorough description of this device, along with a detailed calibration can be found in [129]. Here we summarize the ESA, its operation principle and the configurations used in the work presented. Fig. 5.1 shows a schematic for the ESA used in both target chambers. The ions emitted by the plasma travel in vacuum to the input aperture A_{in} (50 μm diameter in both setups used in this chapter) and then proceed between a pair of curved deflector electrodes. The inner electrode has a radius $r_1 = 190$ mm and the outer one a radius $r_2 = 210$ mm. Opposite bias voltages of $\pm U_{ESA}/2$ are applied to the electrodes (negative at the inner electrode, positive at the outer), resulting in a radial electric field which deflects the ions travelling between the electrodes. Only ions with a specific energy-to-charge ratio are deflected such that they fully traverse the curved path, pass through the output apertures A_{out} and A_{CEM}, and reach the channel electron multiplier (CEM). Ions with higher ratios collide with the outer plate and those with a lower ratio with the inner plate. The energy-to-charge ratio needed for this deflection is given by

$$\frac{E_0}{Z} = \frac{eU_{ESA}}{2\ln(r_2/r_1)} \tag{5.1}$$

Seeing as ions will be deflected only according to their energy-charge ratio, there is still ambiguity. For example, 1 keV Sn^{1+}, 2 keV Sn^{2+}, and 3 keV Sn^{3+} would experience the same deflection and pass through the ESA at the same U_{ESA}. To clear this ambiguity, the time-of-flight of the ions passing through the ESA is recorded with a 600 MHz oscilloscope (Keysight Infiniium). As shown in Fig. 5.2, the faster ions of higher charges have a shorter TOF and the various charge states are clearly separated in a time-resolved count trace. To obtain the full charge-state-resolved ion energy spectrum, U_{ESA} is scanned over the desired range, with the time-resolved count trace measured at every step, each accumulated from 180 laser shots.

The two output apertures, A_{out} and A_{CEM}, are grounded and placed between the electrodes and the CEM to shield each section from the electric field produced in the other. These apertures are much larger than A_{in} such that the geometrical transmission of the ESA is close to unity, as long as space-charge effects do not lead to significant beam expansion during the travel between the electrodes.

In the case of the droplet target, the ESA was mounted at 60° with respect to the incident laser beam. In the case of the solid target, it was observed in prior experiments that as pulse durations became shorter, the majority of the emitted particles is ejected in a narrow cone centered around the laser axis. Therefore, the ESA was mounted at 12° from normal incidence in order to maximize the amount of ions recorded. The distances between the target and the input aperture were 1.16 m and 1.52 m for the droplet target and solid target, respectively.

Lastly, as mentioned in Chapter 2, although the solid targets are cleaned before use, the top layer is subject to oxidation and trace contaminations which result in the first 2-3 shots at each position being contaminated with lighter elements. To identify any contaminated data points, the ESA algorithm first checks for the presence of oxygen and carbon ions at each shot, which indicate the presence of tin oxide and surface contaminations. If any such ions are detected, the data from that shot is discarded.

5.4 RESULTS AND DISCUSSION

Fig. 5.3 shows a selection of charge-state distributions obtained using the ESA, for various laser parameters as indicated. The energy distribution of each charge state is in general well described by a shifted Maxwell-Boltzmann distribution. Some qualitative remarks can be made by comparing the traces. Charge-state distributions created using higher-energy ns pulses reported in literature observe comparable ion yields across the charge states produced [33, 34, 38, 49]. For the shorter pulses used here, we observe a strong drop-off in ion yield as charge state increases, resulting in ion spectra with average charge state $\overline{Z}$ between 1 and 1.5.

We also observe that laser energy has a strong effect both on the maximum Z recorded as well as the energy of each charge state. The effects of laser pulse duration are more subtle, with longer pulses at a given energy producing slightly larger yields of high Z ions. These points will be examined in detail below.

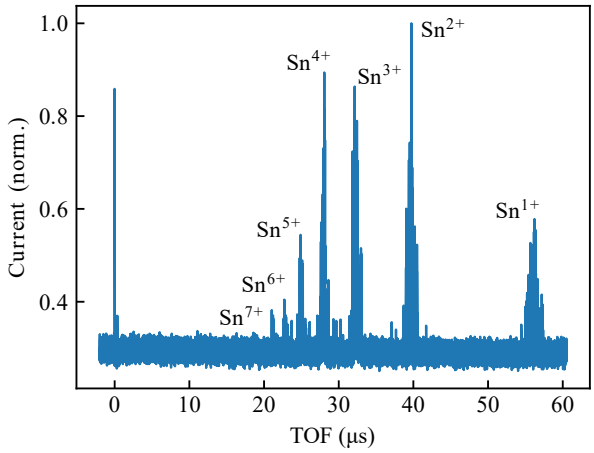

Figure 5.2: ESA TOF trace averaged over 180 laser shots. Each peak corresponds to a single charge state, with lower charge states having longer TOF. The structure of each peak matches well with the relative abundance of tin isotopes, whose slight mass difference leads to peak broadening. The narrow peak at $t = 0$ is created by fast photoelectrons and is used as a reference for the time of target irradiation.

5.4.1 *Effects on charge-state-resolved energy distribution*

Fig. 5.4 shows the mean energy of the ions of each charge state, for a 5 mJ laser pulse at all pulse durations. Two observations stand in contrast with remarks made at this chapter's introduction. Firstly, contrary to what is reported for LPPs created from ns pulses [38, 128], the average kinetic energy of each charge state is not linearly proportional to Z. Second, the duration of the laser pulse has very little effect on the charge-state-resolved energy distribution, not showing obvious effects of a change in dynamics related to the electron-phonon coupling timescales. Therefore, we can conclude that the processes that determine ion kinetic energy in the measurements shown are largely independent of pulse duration in the 0.2-10 ps range covered here.

In contrast to pulse duration, pulse energy does have a significant effect on the mean energy of each charge, as seen in Fig. 5.5. The curves for each energy are averaged over all pulse durations, which is justified given the insensitivity of the ion energy distributions to the pulse duration (Fig. 5.4).

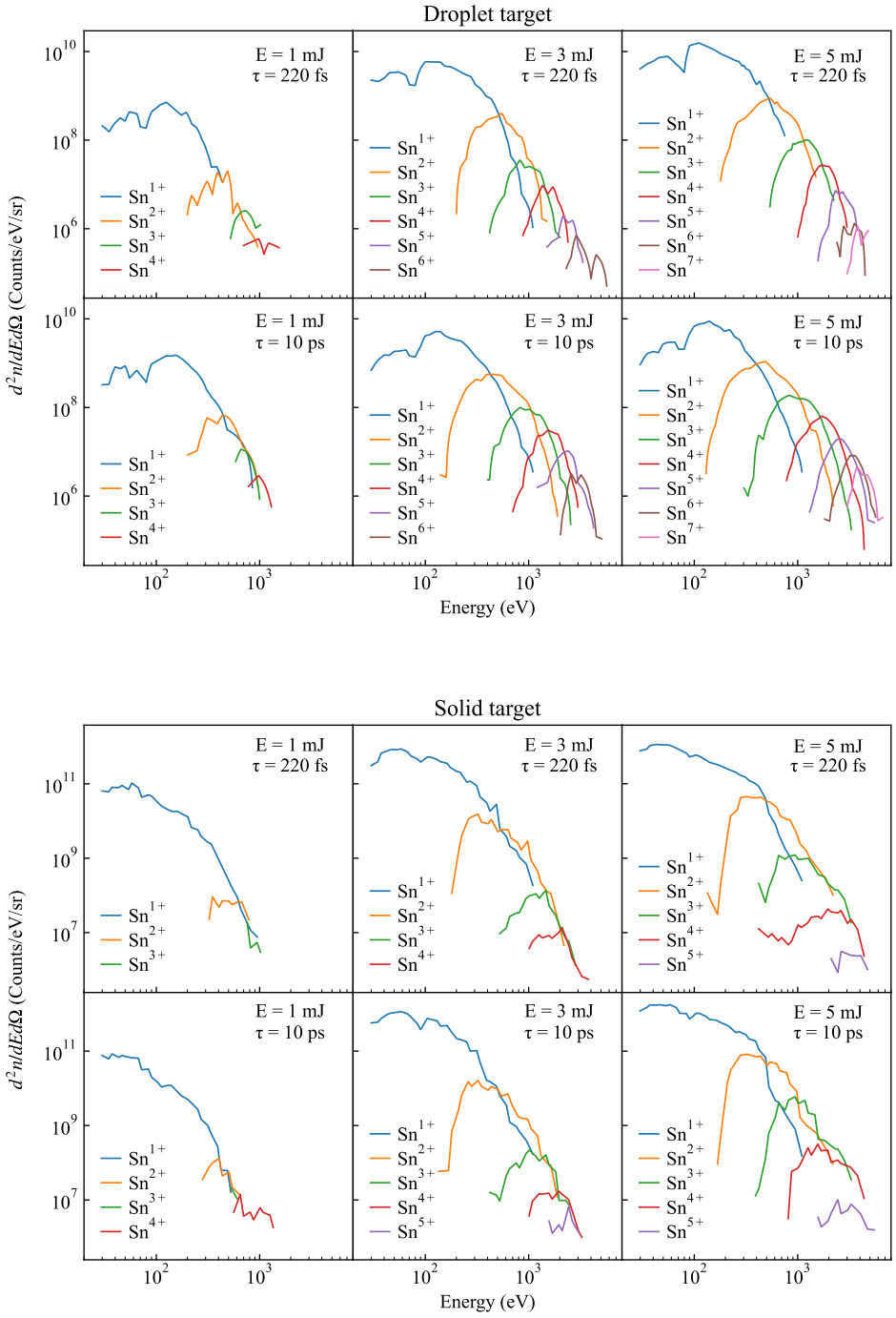

Figure 5.3: Selected overview of the charge-state-resolved kinetic energy distributions obtained from the droplet target (top) and solid target (bottom). The pulse duration (τ) and pulse energy (E) are indicated in each panel.

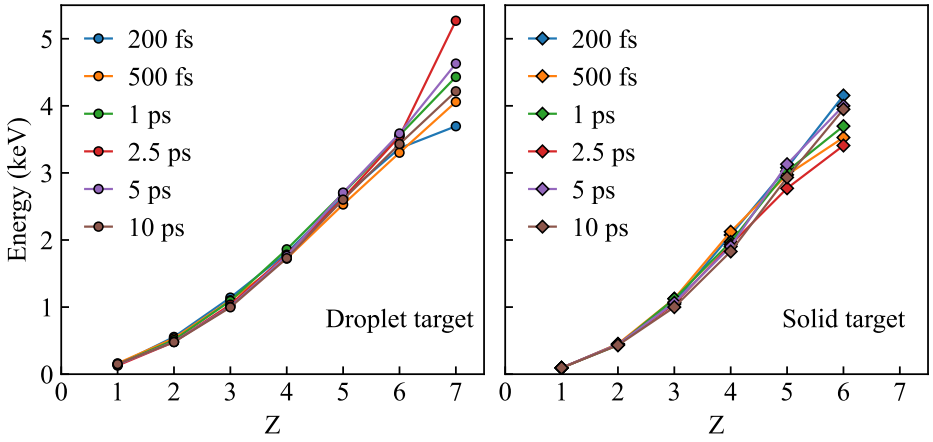

Figure 5.4: Mean ion kinetic energy as a function of charge state (Z), for each pulse duration, for a laser energy of 5 mJ. The energy distribution is not significantly dependent on pulse duration, both for solid and droplet targets. It should be noted that the energy uncertainty increases for higher charge states, as ion yield drops quickly as Z increases. This is noticeable for Sn^{+7} for droplets, and Sn^{+5} and Sn^{+6} for solid targets. Error bars have been omitted as an accurate calculation is not straightforward, but the spread in points gives an indication of the measurement reproducibility.

For the 1 mJ case, we observe a linear relation between mean kinetic energy and charge state. For pulse energies of 3 mJ, the relation becomes nonlinear, and the nonlinearity increases for the highest energy of 5 mJ. It has been derived in [77, 78], based on local characteristic sonic speeds in the plasma, that the ion kinetic energy scales linearly with T and Z:

$$E \propto TZ \tag{5.2}$$

Based on this, a nonlinear relation between mean kinetic energy and charge state indicates that different charges are created in regions of the plasma with different local temperatures.

Table 5.1 shows the coefficients for the 2^{nd} order polynomial fits shown in Fig. 5.5. The transition from a linear trend at 1 mJ to increasingly strong quadratic scaling may indicate the presence of a larger temperature distribution across the plasma for higher pulse energies. In the 1 mJ case, a linear

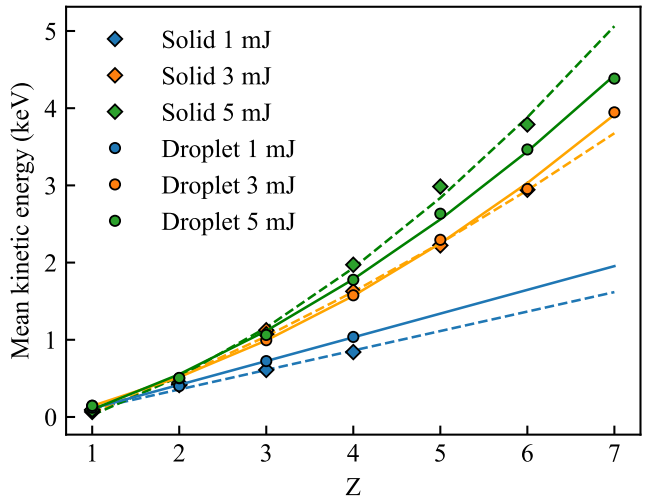

Figure 5.5: Mean ion kinetic energy of each charge state, averaged over all pulse durations. The trend lines (solid for droplet targets, dashed for solid targets) show linear fits to the data for 1 mJ and quadratic fits for 3 mJ and 5 mJ.

Energy	a	b	c	a	b	c
1 mJ	-	307.5	-198.2	-	252.2	-147.8
3 mJ	51.1	220.1	-128.6	27.1	386.8	-360.1
5 mJ	52.9	298.2	-255.2	68.1	295.0	-339.9
	Droplet			Solid		

Table 5.1: Coefficients for the polynomials fits shown in Fig. 5.5 in the form of $E = ax^2 + bx + c$.

trend suggests a constant temperature across the plasma regions where the detected ions are produced, resulting in an ion energy trend which is linearly proportional to charge state. The positive quadratic term suggests that ions with higher ionization states originate from regions of the plasma with higher local temperatures.

Figure 5.6 shows the mean energy of each charge state as a function of incident laser pulse energy. We can see the mean energy of lower-charge-state ions remains nearly constant with increasing laser energy, while the mean energy of the higher-charge-state ions significantly increases towards higher pulse

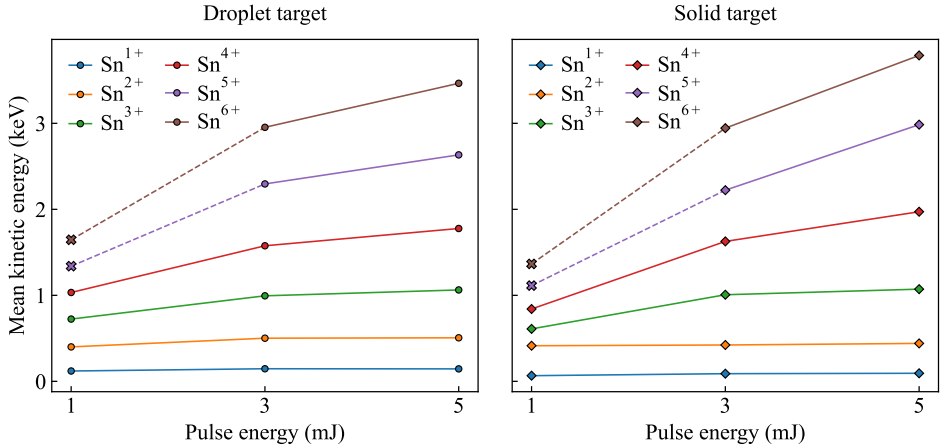

Figure 5.6: Mean energy scaling of each charge state as pulse energy increases. The points marked with a cross and dashed lines assume energies according to the linear fits for the 1 mJ data from Table 5.1, rather than experimentally detected ions.

energy. This trend can be explained by the previous argument that different charge states are created in regions of the plasma with different local temperatures. As laser energy increases, hotter regions within the plasma are created where higher Z ions are produced. With increasing laser energies, the maximum electron temperature will also increase [32], as will the maximum local temperatures where high Z ions are produced, leading to an increase in energy for the ions created within these regions, due to the temperature scaling from eq. 5.2. If lower-charge-state ions are mostly produced in lower temperature regions, which exist within the plasma for all the laser energies reported, one would expect the energy of these ions to be less affected by increases in maximum local temperatures driven by increased laser energy.

5.4.2 *Effects on relative ion abundance and average charge state*

While the ion energy is mostly independent of laser pulse duration, that is not the case for the charge distribution. The relative abundance data shows differences between ions emitted from solid and droplet targets, as seen in Fig. 5.7(a). For droplet targets, longer pulses result in larger amounts of high Z ions. Rather than a gradual change, the relative abundance data changes in steps,

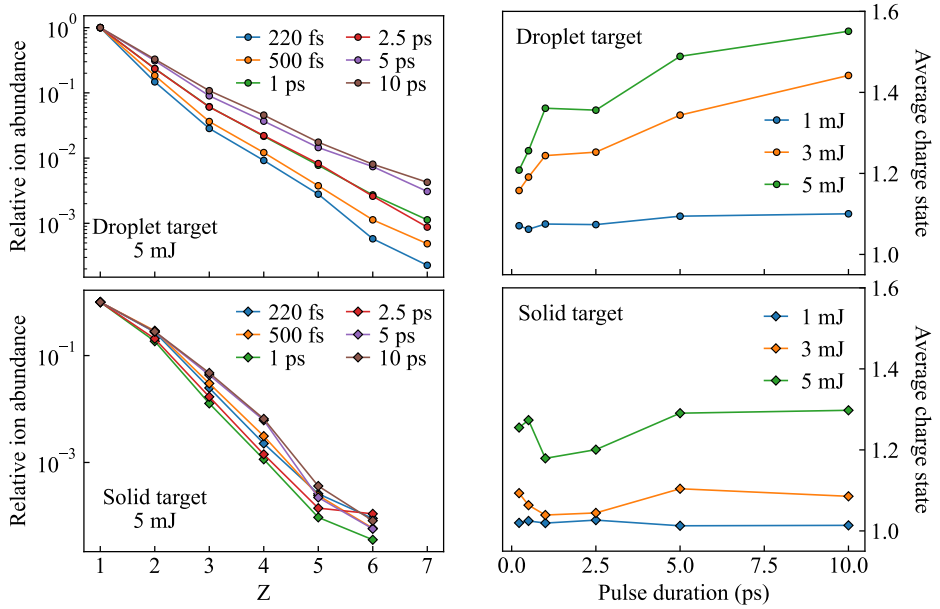

Figure 5.7: **Left:** Relative ion abundance for all pulse durations, for 5 mJ pulses. Relative abundance is not significantly dependent on pulse duration for solid targets. For the droplet targets, high-Z yields increase for longer pulse durations. **Right:** Average charge state as function of pulse duration for all measured laser energies. Z_{avg} is independent of pulse duration for solid targets, but increases with pulse duration for droplet targets for 3 mJ and 5 mJ pulses.

dividing the data into 3 sets of duration pairs: the shorter (220 fs and 500 fs), intermediate (1 ps and 2.5 ps), and longer pulses (5 ps and 10ps). This higher Z for longer pulses trend is also seen in the average charge state (Fig. 5.7 b), though this value is mostly determined by the ratios between Sn^{1+}, Sn^{2+}, and Sn^{3+}.

Data from solid targets, on the other hand, does not show significant dependence on pulse duration. A possible explanation for this discrepancy is a difference in the plasma expansion. As mentioned in Chapter 2, measurements taken using solid flat targets are more representative of 1D plasma expansion into vacuum, while the droplet target features a more complex spherical initial configuration, closer to a 3D expansion. It was observed during the experiments

that the plume is strongly directed orthogonally to the target surface. By contrast, the plasma created from droplet targets, due to the spherical surface, is much less confined as it expanded from the front hemisphere of the droplet. This difference in dimensionality has been predicted to play a key role in the expansion of the plasma into vacuum, according to theoretical models [78, 130].

Another contributing factor could be differences in the matching between the focused beam and the targets. In both cases, the beam is focused to a Gaussian focus with a diameter of 80 μm (FWHM). However, the solid target is much larger than the focus size, while the droplets, with a diameter of 30 μm, are smaller than the focal spot. Although both targets experience the same peak fluence at the center of the focus, the solid target is irradiated by the outer edges of a Gaussian focal spot with lower local fluence, while the droplet is only irradiated by the center portion of the beam and experiences a higher average fluence and a narrower range of local fluences. This is likely to result in different starting conditions for the plasma expansion, which could impact the relative abundance distribution.

5.5 CONCLUSIONS

We have reported the charge-state distributions of ions emitted from tin LPPs created by ultrashort pulses, both in flat solid targets and liquid microdroplets.

For laser energies of 3 mJ and 5 mJ, the nonlinear relation between mean ion kinetic energy and charge state hints at effects beyond a simple model where ions are accelerated by an electrostatic field due to charge separation created by the electrons ejected after laser irradiation.

The energy spectra observed are largely independent of laser pulse duration in the range between 220 fs and 10 ps. This indicates that the timescales of ion acceleration in the observed regime are either shorter than 220 fs or longer than 10 ps. Continuing this work by extending these measurements to even shorter pulses could be an interesting follow-up to learn more about the timescales behind ion acceleration.

We have also found that, for droplet targets, longer pulses lead to higher yields of higher charge-state ions and a higher average charge state. For solid targets, on the other hand, we observed the ion abundance distributions and average charge state to be independent of pulse duration. This may be attributed to differences in the plasma expansion dynamics between the solid and droplet targets, which could be caused by the shape of the target surfaces (flat for solid

targets or spherical for droplet targets) and/or the size of the target compared to the focal spot ("infinite" for solid targets or $\sim$1/3 of FWHM for the droplet target).

6

ION SPECTROMETRY OF PS-PULSE-PAIR-PRODUCED TIN PLASMA

In the work described in this chapter, we create LPPs from solid tin targets using pairs of ps laser pulses, and investigate the influence of laser parameters on ion energy spectra for different charge states. These studies build upon the results from Chapter 4, by adding insight from charge-state-resolved energy measurements with an electrostatic analyzer.

These new charge-resolved measurements show that the introduction of a weaker (tens-of-μJ) pulse preceding a second 5 mJ pulse results in a reduction of ion kinetic energy for every charge state, as well a strong reduction in the yield of higher-charge-state ions, which are the most energetic. For some pulse pair settings, ion yields were reduced to a level where no charge states above Sn^{2+} were detected.

Total ion yield is also shown to decrease for all combinations of first pulse energy and inter-pulse delay, except for the case of $\Delta t = 10$ ns. The reductions in ion yield and energy could be attributed to target ablation caused by the first less energetic pulse, which creates a neutral gas moving away from the target with a thermal velocity of a few eV. The second pulse then interacts with this neutral gas before reaching the target, leading to a more gradual absorption through a longer column of material, resulting in a larger but colder plasma.

6.1 INTRODUCTION

As was shown in Chapter 4, tailored pulse pairs lead to a significant shift of the ion kinetic energy distribution towards lower energies, when compared to plasmas created by a single laser pulse [43]. While these results can be of great practical value when used in conjunction with other ion mitigation techniques such as buffer gases [26, 27, 29], the precise nature of this effect cannot be fully understood without examining the changes in the charge-state-resolved ion energy spectra, as the Faraday cup measurements in Chapter 4 could not discern possible changes in charge state composition. To further explore the underlying effects, these studies were extended to charge-state-resolved measurements on solid targets.

The 33-times reduction of ion most probable kinetic energy (MPKE) reported in Chapter 4 resulted from a combination of a reduction of the yield of ions above 1 keV, and an increased production of low energy ions below 300 eV. The increase in the total amount of charge measured was attributed to a geometric effect due to the mismatch between the laser beam diameter (135 µm) and the tin droplet diameter (30 µm). The first pulse interacts with the droplet and generates a plasma which expands well beyond 30 µm within the time delay between the two pulses, resulting in a larger target interaction area for the second pulse.

The use of solid targets should remove any geometrical effect as conjectured for the droplets, while charge-state-resolved measurements enable the separation of energy reduction and charge state redistribution due to the pulse-pair illumination.

6.2 EXPERIMENTAL SETUP

Fig. 6.1 shows the experimental setup used for the work presented in this chapter. The laser was used in pulse-pair configuration, as described in Chapter 2. As the objective was to build upon the work from Chapter 4 by adding charge-state-resolved measurements, laser parameters were kept very similar. The energy of the first pulse (E_1) was varied between 31 µJ and 500 µJ, with the energy of the second pulse (E_2) being constant at 5 mJ. The delay between the two pulses (Δt) was varied between 10 ns and 500 ns. The duration of both pulses was 50 ps for all measurements, to replicate the laser parameters used to obtain the results in chapter 4.

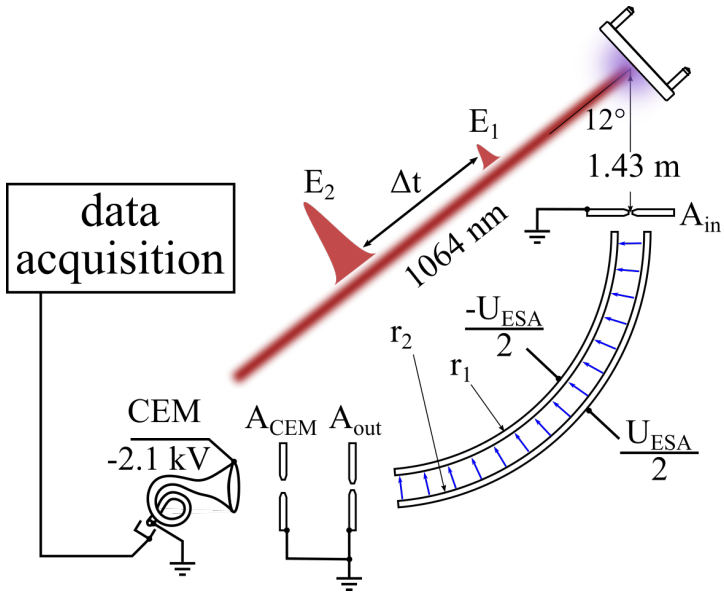

Figure 6.1: Simplified diagram of the experimental setup.

As before, the beam was focused to an 80 µm (FWHM) spot, using a 500 mm-focal-length plano-convex lens. The solid targets and target chamber used have been previously described in Chapter 2 and used in the same configuration as shown in Chapter 5.

The ESA has been previously described in Chapter 5, with the specific geometry shown in Fig. 6.1. As before, care was taken to remove the first shots at each position, because the sample surface is subject to oxidation and contamination, by discarding any shots where carbon and oxygen ions were detected.

6.3 RESULTS AND DISCUSSION

Fig. 6.2 shows a selected overview of the charge-state distributions recorded. For small values of E_1 and Δt, the individual energy distributions for each charge state still resemble the single-pulse case (Fig. 5.3) and can be adequately fitted by shifted Maxwell-Boltzmann distributions (omitted from the figure for clarity of presentation). As E_1 increases, the shape of the peaks for each charge state become increasingly distorted and shifted to lower energies. For larger values

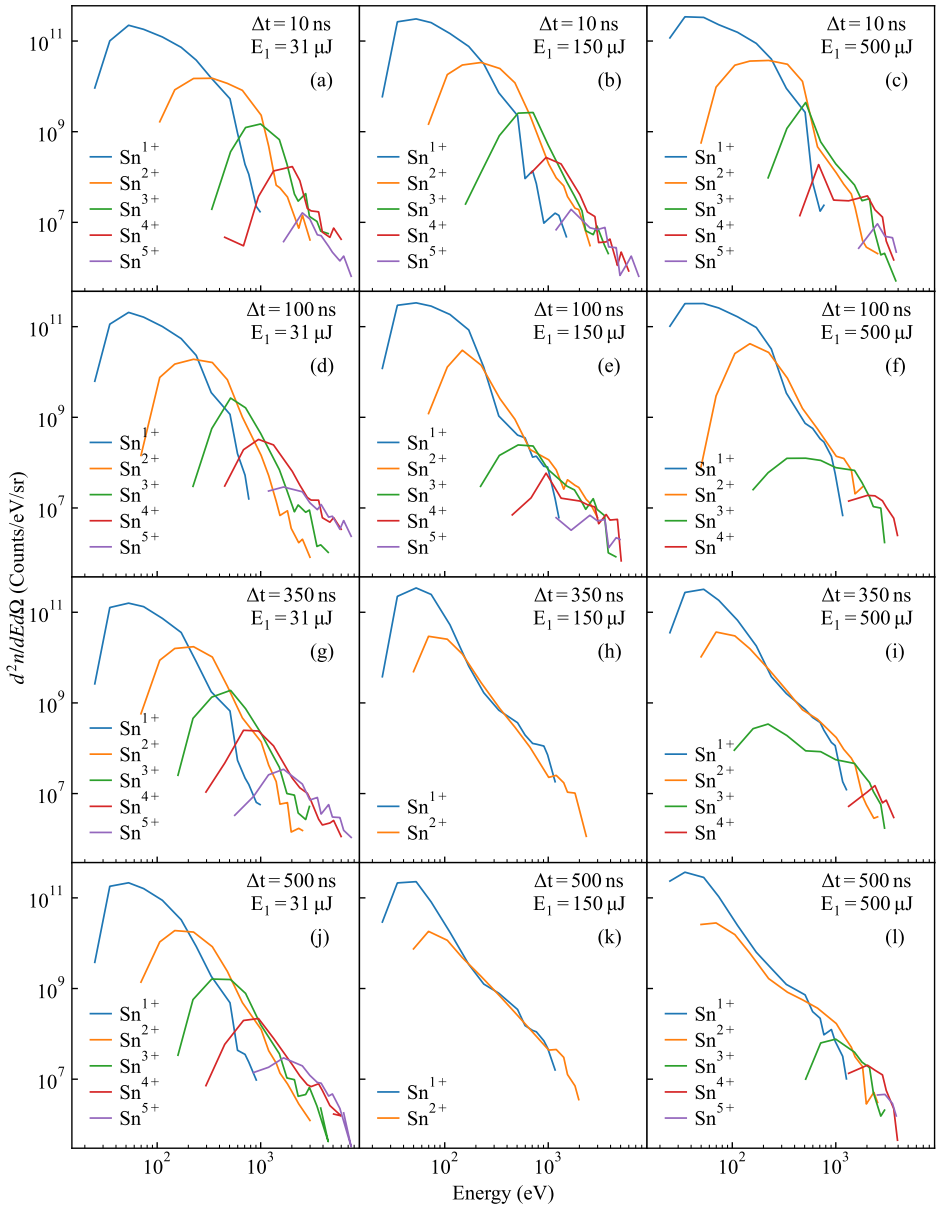

Figure 6.2: Selected overview of the charge-state-resolved energy spectra of ions emitted by LPPs created from laser pulse pairs.

of Δt, the mean energy reduction and distortion of the distribution are further intensified. Furthermore, we find that the relative charge-state distributions change, and that especially higher charge states are increasingly suppressed. Notably, for the case of a 150 μJ pre-pulse at delays above 350 ns (Figs. 6.2(h), 6.2(k)), no ions above Sn^{2+} were detected.

6.4 PULSE PAIR EFFECTS ON ION ENERGY

Although Sn^{5+} is sometimes observed, as seen in Fig. 6.2, it is either detected in minute amounts for some laser parameters, or not at all for others. As such, the uncertainties in the mean kinetic energy, and especially the yield of Sn^{5+} are significant, making it difficult to reliably extract any trends from the data for this charge state. Therefore, we limit the discussion to charge states Sn^{1+} through Sn^{4+}.

For a more systematic overview of the influence of the pre-pulses, in Fig. 6.3 we plot the mean kinetic energy $\bar{E}_k$ (left) and the total ion yield (right) per charge state, as a function of pre-pulse energy. From Figs. 6.3(a) and 6.3(b), we observe that the use of a pulse pair always leads to a reduction in mean energy of Sn^{1+} and Sn^{2+} ions. Increasing E_1 results in further reductions of ion energy. The same trend is observed at each pulse delay, with the reduction effect being stronger for longer delays.

For Sn^{3+} and Sn^{4+} (6.3(c) and 6.3(d)), the behavior is more complex. Some E_1 and Δt combinations result in no ions above Sn^{2+} being detected, as shown in Fig. 6.2(h) and 6.2(k). Increasing E_1 further leads to a reappearance of Sn^{3+} and Sn^{4+}. Notably, for certain values of Δt at $E_1 = 500$ μJ, the energy of Sn^{3+} and Sn^{4+} is again comparable to the single-pulse case.

However, while the mean energy recovers to values comparable to those produced by single pulses, the yield of Sn^{3+} and Sn^{4+} remains much lower, as can be seen in Figs. 6.3(g), 6.3(h), and 6.2(l). As it was seen in Chapter 5 (Fig. 5.5) that ion mean kinetic energy increases with laser energy, one would expect the ions produced by the weaker first pulse to have lower energy. In contrast, we observe the mean energy of Sn^{4+} recovering to values comparable to those of the single-pulse case, which suggests that the resurgent ions are produced by the second, more energetic pulse, rather than the first pulse.

Lastly, from Fig. 6.4 we can see that, compared to the single-pulse case, irradiation with pulse pairs led to a reduction in overall ion energy, i.e. mean

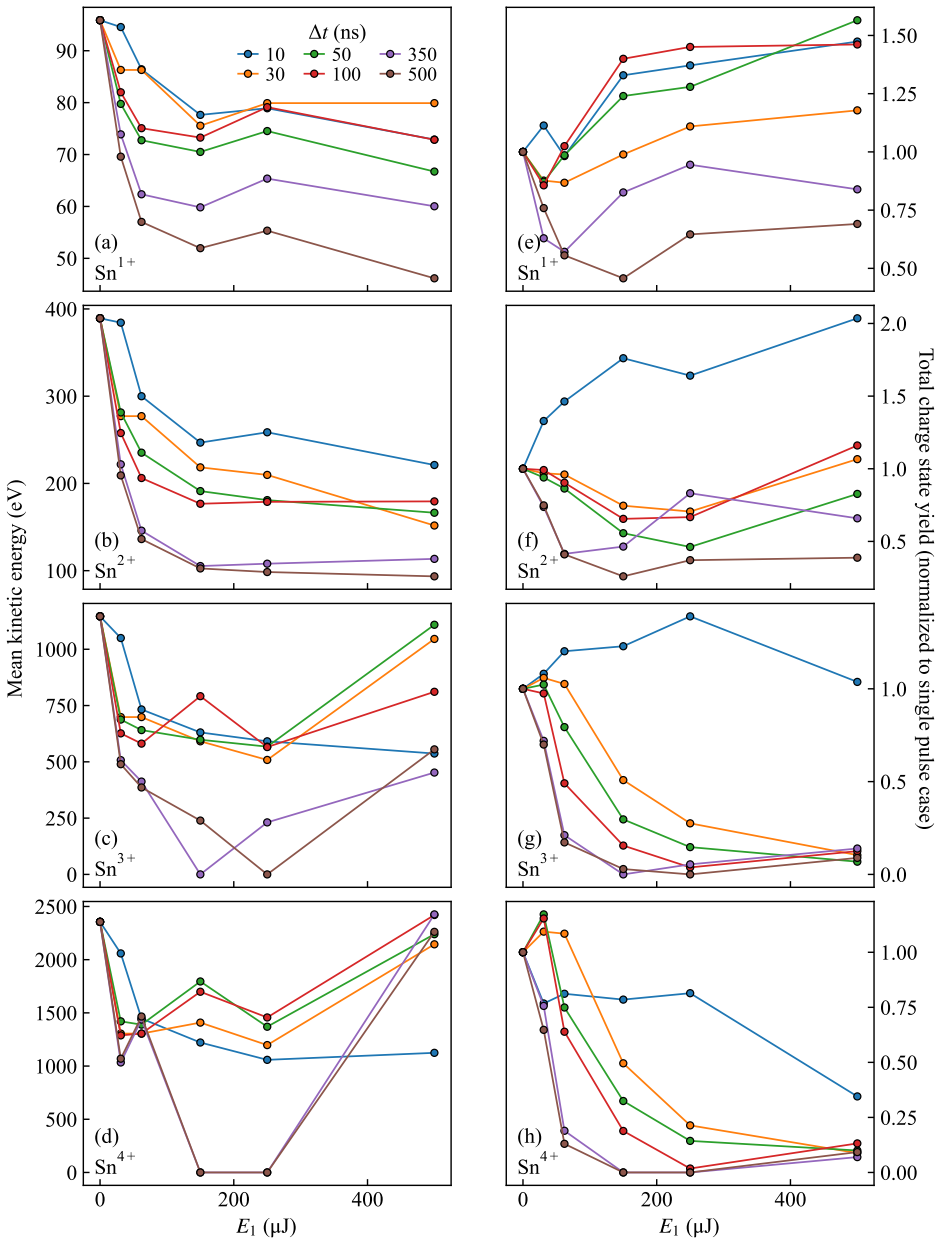

Figure 6.3: Charge-state-resolved mean ion energy (left) and individual charge state yields (right), for all pulse delays Δt and first pulse energies E_1. Note the large differences in vertical scales between the various charge states.

ion kinetic energy across all charge states measured, for all values of E_1 and Δt studied.

A possible explanation for these results is an interaction between the second laser pulse and tin ablated from the sample by the first pulse, as presented in Chapter 4. In the single-pulse case, the laser pulse interacts only with the solid target, where it is absorbed in a thin layer due to the high density of the solid material. This creates a hot plasma, which in turns leads to the creation of energetic ions. For a pulse pair, the first weaker pulse ablates material from the target, creating a small amount of pre-plasma with which the second pulse interacts, in addition with the target. This results in the second pulse being absorbed across a thicker layer, resulting in a colder plasma and lower ion energies than in the single-pulse case, as well as the reduced yield of higher-charge-state ions.

On the other hand, the increase of lower charge state ion yields at short time delays may result from the interaction of the second pulse with the relatively dense vapor, which may be stronger than the absorption at the solid target interface. An increase in ion yield has been observed for pairs of fs-duration pulses with ps pulse-to-pulse delays, attributed to an increased coupling between the second pulse and the target, due to a favorable density gradient created by the first pulse interacting with the target [131].

6.5 PULSE-PAIR EFFECTS ON CHARGE-STATE YIELD

From Fig. 6.3, we see a rapid decrease in the yield of Sn^{3+} and Sn^{4+} with increasing E_1. This behavior is seen for all values of Δt except for 10 ns, with the decrease being more rapid for larger delays. To compare the total ion yield for pulse-pair irradiation to the single-pulse case, we plot the ratio of these yields in Fig. 6.4. From this data, we see that the total charge detected is higher than that of the single-pulse case only for $\Delta t = 10$ ns. For all other delays and first pulse energies, the total charge yield is lower or comparable to that of the single-pulse case.

Notably, the case of ($E_1 = 150$ μJ, $\Delta t = 500$ ns) is the minimum of both total charge as well as mean ion energy. This is in contrast with the droplet case presented in Chapter 4, where a decrease in ion energy is the result of a decrease in the amount of high energy ions as well as an increase in lower energy ions, resulting in an increase of total charge. This difference between solid and droplet targets suggests that the increased yield observed in the droplet

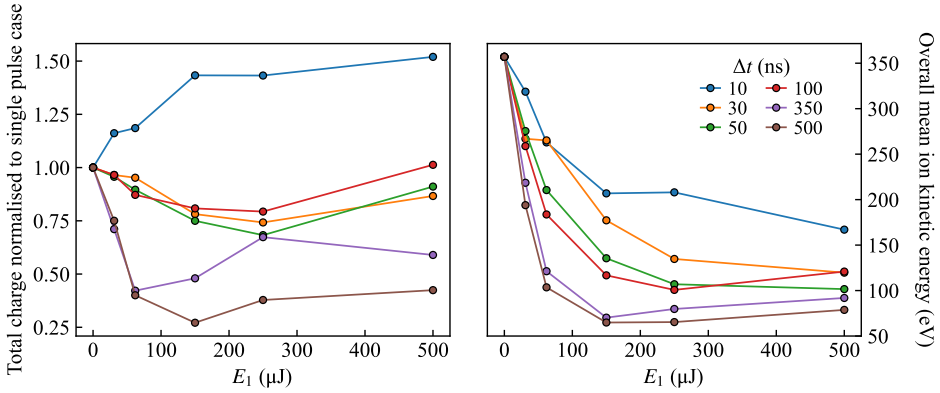

Figure 6.4: Left: Effects of pulse delay Δt and first pulse energy E_1 on the total collected charge. Right: Overall mean ion kinetic energy (i.e. aggregated across all charge states) for all values Δt and E_1 studied.

target experiments indeed resulted from geometrical effects, where the first pulse creates a small amount of plasma which quickly expands resulting in better coupling between the now-larger target and the second pulse.

6.6 CONCLUSIONS

These new charge-resolved measurements show that the introduction of a weaker (tens-of-μJ) pulse preceding a second 5 mJ pulse results in a reduction of ion kinetic energy for every charge state, as well a strong reduction in the yield of higher-charge-state ions, which are the most energetic. Notably, for some pulse-pair settings, it was possible to suppress higher charge states above Sn^{2+}. This suppression is of practical interest to increase the lifetime of optical components inside EUV sources, especially when paired with ion mitigation techniques which are most effective for lower-energy ions below 1 keV.

Furthermore, for all pulse-to-pulse delays except $\Delta t = 10$ ns, total ion yield was lower than in the single-pulse case. This is in contrast with the data obtained in Chapter 4, indicating that the increased ion yield observed for droplet targets for longer pulse-to-pulse delays was due to geometrical effects caused by droplet expansion driven by the first pulse, i.e. increased overlap between the laser and target.

In future experiments, the addition of measurement methods to characterize neutrals ejected from the target, such as transverse optical probing, would provide valuable information on the density and velocity distributions of the neutrals created by the first pulse. A better understanding of the temporal evolution of the density profile in front of the initial target surface will be key to explain some of the more complex behavior observed, such as the suppression and resurgence of Sn^{3+} and Sn^{4+} for larger values of Δt. Additionally, correlating experimentally-measured target density distributions with ion yield will shed light on the relation between laser coupling and target density profile, a problem which has been extensively studied in a theoretical framework related to plasma expansion into vacuum.

Lastly, recent work at ARCNL on development of calibrated retarding-field analyzers (RFA) [34] could also be used to provide a clearer picture of the double-pulse dynamics. Since RFAs are more compact than ESAs, it is possible for multiple devices to be mounted at different angles with respect to the target surface, to evaluate the effects of the double-pulse configuration in the angular distribution of ion energy [33].

BIBLIOGRAPHY

[1] I. M. Ross, "The foundation of the silicon age," Bell Labs Technical Journal **2**, 3–14 (2002).

[2] G. E. Moore, "Cramming more components onto integrated circuits," Proceedings of the IEEE **86**, 82–85 (1965).

[3] G. E. Moore, "Progress In Digital Integrated Electronics," IEEE Solid-State Circuits Society Newsletter **11**, 36–37 (1975).

[4] A. J. den Boef, "Optical wafer metrology sensors for process-robust CD and overlay control in semiconductor device manufacturing," Surface Topography: Metrology and Properties **4**, 023001 (2016).

[5] P. Van Zant, *Microchip fabrication: a practical guide to semiconductor processing*, Sixth edition (McGraw-Hill Professional, New York, 2014).

[6] B. Wu and A. Kumar, "Extreme ultraviolet lithography: A review," Journal of Vacuum Science & Technology B: Microelectronics and Nanometer Structures **25**, 1743 (2007).

[7] C. Wagner and N. Harned, "Lithography gets extreme," Nature Photonics **4**, 24–26 (2010).

[8] T. W. Barbee, S. Mrowka, and M. C. Hettrick, "Molybdenum-silicon multilayer mirrors for the extreme ultraviolet," Applied Optics **24**, 883 (1985).

[9] V. Bakshi, ed., *EUV sources for lithography* (SPIE Press, 2006).

[10] G. O'Sullivan, B. Li, R. D'Arcy, P. Dunne, P. Hayden, D. Kilbane, T. McCormack, H. Ohashi, F. O'Reilly, P. Sheridan, E. Sokell, C. Suzuki, and T. Higashiguchi, "Spectroscopy of highly charged ions and its relevance to EUV and soft x-ray source development," Journal of Physics B: Atomic, Molecular and Optical Physics **48**, 144025 (2015).

[11] Y. Kawasuji, K. M. Nowak, T. Hori, T. Okamoto, H. Tanaka, Y. Watanabe, T. Abe, T. Kodama, Y. Shiraishi, H. Nakarai, T. Yamazaki, S. Okazaki, T. Saitou, and H. Mizoguchi, "Key components technology update of the 250W high-power LPP-EUV light source," Proc. SPIE, 101432G (2017).

[12]I. Fomenkov, D. Brandt, A. Ershov, A. Schafgans, Y. Tao, G. Vaschenko, S. Rokitski, M. Kats, M. Vargas, M. Purvis, R. Rafac, B. La Fontaine, S. De Dea, A. LaForge, J. Stewart, S. Chang, M. Graham, D. Riggs, T. Taylor, M. Abraham, and D. Brown, "Light sources for high-volume manufacturing EUV lithography: technology, performance, and power scaling," Advanced Optical Technologies **6**, 173–186 (2017).

[13]I. Fomenkov, A. Schafgans, and D. Brandt, "Laser-Produced Plasma Sources for High-Volume-Manufacturing EUV Lithography," Synchrotron Radiation News **32**, 3–8 (2019).

[14]K. Nishihara, A. Sunahara, A. Sasaki, M. Nunami, H. Tanuma, S. Fujioka, Y. Shimada, K. Fujima, H. Furukawa, T. Kato, F. Koike, R. More, M. Murakami, T. Nishikawa, V. Zhakhovskii, K. Gamata, A. Takata, H. Ueda, H. Nishimura, Y. Izawa, N. Miyanaga, and K. Mima, "Plasma physics and radiation hydrodynamics in developing an extreme ultraviolet light source for lithography," Physics of Plasmas **15**, 056708 (2008).

[15]H. Tanaka, A. Matsumoto, K. Akinaga, A. Takahashi, and T. Okada, "Comparative study on emission characteristics of extreme ultraviolet radiation from CO2 and Nd:YAG laser-produced tin plasmas," Applied Physics Letters **87**, 041503 (2005).

[16]R. Schupp, F. Torretti, R. Meijer, M. Bayraktar, J. Scheers, D. Kurilovich, A. Bayerle, K. Eikema, S. Witte, W. Ubachs, R. Hoekstra, and O. Versolato, "Efficient Generation of Extreme Ultraviolet Light From Nd :YAG-Driven Microdroplet-Tin Plasma," Physical Review Applied **12**, 014010 (2019).

[17]V. Y. Banine, K. N. Koshelev, and G. H. P. M. Swinkels, "Physical processes in EUV sources for microlithography," Journal of Physics D: Applied Physics **44**, 253001 (2011).

[18]Y. Ueno, G. Soumagne, A. Sumitani, A. Endo, and T. Higashiguchi, "Enhancement of extreme ultraviolet emission from a CO2 laser-produced Sn plasma using a cavity target," Applied Physics Letters **91**, 231501 (2007).

[19]R. Meijer, *Tailored laser-droplet interaction: for target formation in extreme ultraviolet sources* (Ph.D. thesis, Vrije Universiteit Amsterdam, 2021).

[20]M. van de Kerkhof, H. Jasper, L. Levasier, R. Peeters, R. van Es, J.-W. Bosker, A. Zdravkov, E. Lenderink, F. Evangelista, P. Broman, B. Bilski, and T. Last, "Enabling sub-10nm node lithography: presenting the

NXE:3400B EUV scanner," Extreme Ultraviolet (EUV) Lithography VIII **10143**, 101430D (2017).

[21]D. Kurilovich, M. M. Basko, D. A. Kim, F. Torretti, R. Schupp, J. C. Visschers, J. Scheers, R. Hoekstra, W. Ubachs, and O. O. Versolato, "Power-law scaling of plasma pressure on laser-ablated tin microdroplets," Physics of Plasmas **25**, 012709 (2018).

[22]D. Kurilovich, A. L. Klein, F. Torretti, A. Lassise, R. Hoekstra, W. Ubachs, H. Gelderblom, and O. O. Versolato, "Plasma Propulsion of a Metallic Microdroplet and its Deformation upon Laser Impact," Physical Review Applied **6**, 014018 (2016).

[23]H. Gelderblom, H. Lhuissier, A. L. Klein, W. Bouwhuis, D. Lohse, E. Villermaux, and J. H. Snoeijer, "Drop deformation by laser-pulse impact," Journal of Fluid Mechanics **794**, 676–699 (2016).

[24]D. Kurilovich, T. de Faria Pinto, F. Torretti, R. Schupp, J. Scheers, A. S. Stodolna, H. Gelderblom, K. S. Eikema, S. Witte, W. Ubachs, R. Hoekstra, and O. O. Versolato, "Expansion dynamics after laser-induced cavitation in liquid tin microdroplets," Phys. Rev. Appl. **10**, 054005 (2018).

[25]M. S. Krivokorytov, A. Y. Vinokhodov, Y. V. Sidelnikov, V. M. Krivtsun, V. O. Kompanets, A. A. Lash, K. N. Koshelev, and V. V. Medvedev, "Cavitation and spallation in liquid metal droplets produced by subpicosecond pulsed laser radiation," Physical Review E **95**, 031101 (2017).

[26]D. Nakamura, K. Tamaru, Y. Hashimoto, T. Okada, H. Tanaka, and A. Takahashi, "Mitigation of fast ions generated from laser-produced Sn plasma for extreme ultraviolet light source by H2 gas," Journal of Applied Physics **102**, 123310 (2007).

[27]Y. Sun, J. Lin, X. Gao, and Z. Zhao, "Characteristics of ion debris from laser-produced tin plasma and mitigation of energetic ions by ambient gas," Science China Physics, Mechanics and Astronomy **55**, 392–395 (2012).

[28]H. Komori, Y. Imai, G. Soumagne, T. Abe, T. Suganuma, and A. Endo, "Magnetic field ion mitigation for EUV light sources," Proc. SPIE **5751**, 859–866 (2005).

[29]S. Harilal, B. O'Shay, Y. Tao, and M. Tillack, "Ion debris mitigation from tin plasma using ambient gas, magnetic field and combined effects," Applied Physics B **86**, 547–553 (2007).

[30]Z. Zhang, P. A. VanRompay, J. A. Nees, and P. P. Pronko, "Multi-diagnostic comparison of femtosecond and nanosecond pulsed laser plasmas," Journal of Applied Physics **92**, 2867–2874 (2002).

[31]X. Wang, S. Zhang, X. Cheng, E. Zhu, W. Hang, and B. Huang, "Ion kinetic energy distributions in laser-induced plasma," Spectrochimica Acta Part B: Atomic Spectroscopy **99**, 101–114 (2014).

[32]E. Gamaly, "The physics of ultra-short laser interaction with solids at non-relativistic intensities," Physics Reports **508**, 91–243 (2011).

[33]L. Poirier, D. J. Hemminga, A. Lassise, L. Assink, R. Hoekstra, J. Sheil, and O. O. Versolato, "Strongly anisotropic ion emission in the expansion of Nd:YAG-laser-produced plasma," Physics of Plasmas **29**, 123102 (2022).

[34]L. Poirier, A. Lassise, Y. Mostafa, L. Behnke, N. Braaksma, L. Assink, R. Hoekstra, and O. O. Versolato, "Energy- and charge-state-resolved spectrometry of tin laser-produced plasma using a retarding field energy analyzer," Applied Physics B **128**, 135 (2022).

[35]R. Dinger, K. Rohr, and H. Weber, "Plasma ion spectra from laser produced plasmas at λ = 1·06 μm and λ =0·53 μm," Laser and Particle Beams **4**, 239–247 (1986).

[36]L. Torrisi, F. Caridi, A. Picciotto, and A. Borrielli, "Energy distribution of particles ejected by laser-generated aluminium plasma," Nuclear Instruments and Methods in Physics Research Section B: Beam Interactions with Materials and Atoms **252**, 183–189 (2006).

[37]L. Torrisi, F. Caridi, A. Picciotto, D. Margarone, and A. Borrielli, "Particle emission from tantalum plasma produced by 532nm laser pulse ablation," Journal of Applied Physics **100**, 093306 (2006).

[38]L. Torrisi, S. Gammino, L. Andò, and L. Làska, "Tantalum ions produced by 1064 nm pulsed laser irradiation," Journal of Applied Physics **91**, 4685–4692 (2002).

[39]D. Wu, X. Mao, G. C.-Y. Chan, R. E. Russo, V. Zorba, and H. Ding, "Dynamic characteristics of multi-charged ions emitted from nanosecond laser produced molybdenum plasmas," Journal of Analytical Atomic Spectrometry **35**, 767–775 (2020).

[40]P. Écija, M. N. Sánchez Rayo, R. Martínez, B. Sierra, C. Redondo, F. J. Basterretxea, and F. Castaño, "Fundamental processes in nanosecond pulsed laser ablation of metals in vacuum," Physical Review A **77**, 032904 (2008).

[41]M. H. A. Shaim, F. G. Wilson, and H. E. Elsayed-Ali, "Aluminum multi-charged ion generation from femtosecond laser plasma," Journal of Applied Physics **121**, 185901 (2017).

[42]L. Torrisi, M. Rosinski, D. Terwinska, P. Tchorz, M. Cutroneo, and A. Torrisi, "Ion acceleration from aluminium plasma generated by a femtosecond laser in different conditions," Contributions to Plasma Physics **60**, e201900187 (2020).

[43]A. S. Stodolna, T. de Faria Pinto, F. Ali, A. Bayerle, D. Kurilovich, J. Mathijssen, R. Hoekstra, O. O. Versolato, K. S. E. Eikema, and S. Witte, "Controlling ion kinetic energy distributions in laser produced plasma sources by means of a picosecond pulse pair," Journal of Applied Physics **124**, 053303 (2018).

[44]R. A. Meijer, A. S. Stodolna, K. S. E. Eikema, and S. Witte, "High-energy Nd:YAG laser system with arbitrary sub-nanosecond pulse shaping capability," Optics Letters **42**, 2758 (2017).

[45]T. de Faria Pinto, J. Mathijssen, K. S. E. Eikema, and S. Witte, "Optical parametric chirped pulse amplifier producing ultrashort 10.5 mJ pulses at 1.55 µm," Optics Express **27**, 29829 (2019).

[46]M. M. Basko, M. S. Krivokorytov, A. Yu Vinokhodov, Y. V. Sidelnikov, V. M. Krivtsun, V. V. Medvedev, D. A. Kim, V. O. Kompanets, A. A. Lash, and K. N. Koshelev, "Fragmentation dynamics of liquid-metal droplets under ultra-short laser pulses," Laser Physics Letters **14**, 036001 (2017).

[47]L. Torrisi, "Ion charge state distributions in plasma produced by pulsed laser irradiations," Radiation Effects and Defects in Solids **159**, 249–258 (2004).

[48]L. Torrisi, F. Caridi, D. Margarone, and A. Borrielli, "Characterization of laser-generated silicon plasma," Applied Surface Science **254**, 2090–2095 (2008).

[49]F. Caridi, L. Torrisi, D. Margarone, A. Picciotto, A. M. Mezzasalma, and S. Gammino, "Energy distributions of particles ejected from laser-generated pulsed plasmas," Czechoslovak Journal of Physics **56**, B449–B456 (2006).

[50]A. Bayerle, M. J. Deuzeman, S. v. d. Heijden, D. Kurilovich, T. de Faria Pinto, A. Stodolna, S. Witte, K. S. E. Eikema, W. Ubachs, R. Hoekstra, and O. O. Versolato, "Sn ion energy distributions of ns- and ps-laser produced plasmas," Plasma Sources Science and Technology **27**, 045001 (2018).

[51]S. Witte, R. T. Zinkstok, W. Hogervorst, and K. S. E. Eikema, "Generation of few-cycle terawatt light pulses using optical parametric chirped pulse amplification," Optics Express **13**, 4903 (2005).

[52]S. Witte, R. T. Zinkstok, A. L. Wolf, W. Hogervorst, W. Ubachs, and K. S. E. Eikema, "A source of 2 terawatt, 2.7 cycle laser pulses based on noncollinear optical parametric chirped pulse amplification," Optics Express **14**, 8168–8177 (2006).

[53]S. Witte, R. T. Zinkstok, W. Hogervorst, and K. S. E. Eikema, "Numerical simulations for performance optimization of a few-cycle terawatt NOPCPA system," Applied Physics B **87**, 677–684 (2007).

[54]F. Tavella, A. Marcinkevicius, and F. Krausz, "90 mJ parametric chirped pulse amplification of 10 fs pulses," Optics Express **14**, 12822–12827 (2006).

[55]M. Schultze, T. Binhammer, A. Steinmann, G. Palmer, M. Emons, and U. Morgner, "Few-cycle OPCPA system at 143 kHz with more than 1 μJ of pulse energy," Optics Express **18**, 2836–2841 (2010).

[56]S. Prinz, M. Haefner, C. Y. Teisset, R. Bessing, K. Michel, Y. Lee, X. T. Geng, S. Kim, D. E. Kim, T. Metzger, and M. Schultze, "CEP-stable, sub-6 fs, 300-kHz OPCPA system with more than 15 W of average power," Optics Express **23**, 1388–1394 (2015).

[57]R. Budriunas, T. Stanislauskas, J. Adamonis, A. Aleknaviçius, G. Veitas, D. Gadonas, S. Balickas, A. Michailovas, and A. Varanaviçius, "53 W average power CEP-stabilized OPCPA system delivering 5.5 TW few cycle pulses at 1 kHz repetition rate," Optics Express **25**, 5797–5806 (2017).

[58]B. W. Mayer, C. R. Phillips, L. Gallmann, M. M. Fejer, and U. Keller, "Sub-four-cycle laser pulses directly from a high-repetition-rate optical parametric chirped-pulse amplifier at 3.4 μm," Optics Letters **38**, 4265–4268 (2013).

[59]G. Andriukaitis, T. Balčiūnas, S. Ališauskas, A. Pugžlys, A. Baltuška, T. Popmintchev, M.-C. Chen, M. M. Murnane, and H. C. Kapteyn, "90 GW peak power few-cycle mid-infrared pulses from an optical parametric amplifier," Optics Letters **36**, 2755 (2011).

[60]O. Chalus, P. K. Bates, M. Smolarski, and J. Biegert, "Mid-IR short-pulse OPCPA with micro-Joule energy at 100kHz," Optics Express **17**, 3587 (2009).

[61]C. Erny, C. Heese, M. Haag, L. Gallmann, and U. Keller, "High-repetition-rate optical parametric chirped-pulse amplifier producing 1-μJ, sub-100-fs pulses in the mid-infrared," Optics Express **17**, 1340 (2009).

[62]C. Heese, C. R. Phillips, L. Gallmann, M. M. Fejer, and U. Keller, "Ultra-broadband, highly flexible amplifier for ultrashort midinfrared laser pulses based on aperiodically poled Mg:$LiNbO_3$," Optics Letters **35**, 2340 (2010).

[63]C. Heese, C. R. Phillips, B. W. Mayer, L. Gallmann, M. M. Fejer, and U. Keller, "75 MW few-cycle mid-infrared pulses from a collinear apodized APPLN-based OPCPA," Optics Express **20**, 26888 (2012).

[64]D. Kraemer, R. Hua, M. L. Cowan, K. Franjic, and R. J. D. Miller, "Ultrafast noncollinear optical parametric chirped pulse amplification in $KTiOAsO_4$," Optics Letters **31**, 981 (2006).

[65]D. Kraemer, M. L. Cowan, R. Hua, K. Franjic, and R. J. Dwayne Miller, "High-power femtosecond infrared laser source based on noncollinear optical parametric chirped pulse amplification," Journal of the Optical Society of America B **24**, 813 (2007).

[66]D. Brida, G. Cirmi, C. Manzoni, S. Bonora, P. Villoresi, S. D. Silvestri, and G. Cerullo, "Sub-two-cycle light pulses at 1.6 μm from an optical parametric amplifier," Optics Letters **33**, 741–743 (2008).

[67]D. Brida, G. Krauss, A. Sell, and A. Leitenstorfer, "Ultrabroadband Er:fiber lasers," Laser & Photonics Reviews **8**, 409–428 (2014).

[68]J. Morgenweg and K. S. E. Eikema, "A 1.8 mJ, picosecond Nd:YVO_4 bounce amplifier pump front-end system for high-accuracy XUV-frequency comb spectroscopy," Laser Physics Letters **9**, 781–785 (2012).

[69]D. W. E. Noom, S. Witte, J. Morgenweg, R. K. Altmann, and K. S. E. Eikema, "High-energy, high-repetition-rate picosecond pulses from a quasi-CW diode-pumped Nd:YAG system," Optics Letters **38**, 3021 (2013).

[70]L. Sun, L. Zhang, H. J. Yu, L. Guo, J. L. Ma, J. Zhang, W. Hou, X. C. Lin, and J. M. Li, "880 nm LD pumped passive mode-locked TEM00 Nd:YVO_4 laser based on SESAM," Laser Physics Letters **7**, 711 (2010).

[71]J. Morgenweg, *Ramsey-comb spectroscopy* (Ph.D. Thesis, Vrije Universiteit Amsterdam, 2014).

[72]Q. Lü, N. Kugler, H. Weber, S. Dong, N. Müller, and U. Wittrock, "A novel approach for compensation of birefringence in cylindrical Nd:YAG rods," Optical and Quantum Electronics **28**, 57–69 (1996).

[73]J. Sherman, "Thermal compensation of a cw-pumped Nd:YAG laser," Applied Optics **37**, 7789 (1998).

[74]S. Witte and K. S. E. Eikema, "Ultrafast Optical Parametric Chirped-Pulse Amplification," IEEE Journal of Selected Topics in Quantum Electronics **18**, 296–307 (2012).

[75]D. Kurilovich, *Laser-induced dynamics of liquid tin microdroplets* (Ph.D. Thesis, Vrije Universiteit Amsterdam, 2019).

[76]Y. Kishimoto, K. Mima, T. Watanabe, and K. Nishikawa, "Analysis of fast-ion velocity distributions in laser plasmas with a truncated Maxwellian velocity distribution of hot electrons," The Physics of Fluids **26**, 2308–2315 (1983).

[77]P. Mora, "Plasma Expansion into a Vacuum," Physical Review Letters **90**, 185002 (2003).

[78]M. Murakami, Y.-G. Kang, K. Nishihara, S. Fujioka, and H. Nishimura, "Ion energy spectrum of expanding laser-plasma with limited mass," Physics of Plasmas **12**, 062706 (2005).

[79]T. de Faria Pinto, J. Mathijssen, R. Meijer, H. Zhang, A. Bayerle, D. Kurilovich, O. O. Versolato, K. S. E. Eikema, and S. Witte, "Cylindrically and non-cylindrically symmetric expansion dynamics of tin microdroplets after ultrashort laser pulse impact," Applied Physics A **127**, 93 (2021).

[80]J. Benschop, V. Banine, S. Lok, and E. Loopstra, "Extreme ultraviolet lithography: Status and prospects," Journal of Vacuum Science & Technology B: Microelectronics and Nanometer Structures **26**, 2204–2207 (2008).

[81]H. Mizoguchi, T. Abe, Y. Watanabe, T. Ishihara, T. Ohta, T. Hori, A. Kurosu, H. Komori, K. Kakizaki, A. Sumitani, O. Wakabayashi, H. Nakarai, J. Fujimoto, and A. Endo, "First generation laser-produced plasma source system for HVM EUV lithography," Proc. of SPIE **7636**, 763608 (2010).

[82]O. O. Versolato, "Physics of laser-driven tin plasma sources of euv radiation for nanolithography," Plasma Sources Science and Technology **28**, 083001 (2019).

[83]S. K. Moore, "EUV lithography finally ready for fabs," IEEE Spectrum **55**, 46–48 (2018).

[84]M. Purvis, I. V. Fomenkov, A. A. Schafgans, M. Vargas, S. Rich, Y. Tao, S. I. Rokitski, M. Mulder, E. Buurman, M. Kats, J. Stewart, A. D. LaForge, C. Rajyaguru, G. Vaschenko, A. I. Ershov, R. J. Rafac, M. Abraham, D. C. Bandt, and D. J. Brown, "Industrialization of a robust EUV source for high-volume manufacturing and power scaling beyond 250W," Proc. of SPIE **10583**, 1058327 (2018).

[85]A. Pirati, R. Peeters, D. Smith, S. Lok, A. W. E. Minnaert, M. van Noordenburg, J. Mallmann, N. Harned, J. Stoeldraijer, C. Wagner, C. Zoldesi, E. van Setten, J. Finders, K. de Peuter, C. de Ruijter, M. Popadic, R. Huang, M. Lin, F. Chuang, R. van Es, M. Beckers, D. Brandt, N. Farrar, A. Schafgans, D. Brown, H. Boom, H. Meiling, and R. Kool, "Performance overview and outlook of EUV lithography systems," Proc. of SPIE **9422**, 94221P (2015).

[86]S. Y. Grigoryev, B. V. Lakatosh, M. S. Krivokorytov, V. V. Zhakhovsky, S. A. Dyachkov, D. K. Ilnitsky, K. P. Migdal, N. A. Inogamov, A. Y. Vinokhodov, V. O. Kompanets, Y. V. Sidelnikov, V. M. Krivtsun, K. N. Koshelev, and V. V. Medvedev, "Expansion and fragmentation of a liquid-metal droplet by a short laser pulse," Phys. Rev. Applied **10**, 064009 (2018).

[87]M. S. Krivokorytov, Q. Zeng, B. V. Lakatosh, A. Y. Vinokhodov, Y. V. Sidelnikov, V. O. Kompanets, V. M. Krivtsun, K. N. Koshelev, C. D. Ohl, and V. V. Medvedev, "Shaping and Controlled Fragmentation of Liquid Metal Droplets through Cavitation," Scientific Reports **8**, 597 (2018).

[88]S. A. Reijers, J. H. Snoeijer, and H. Gelderblom, "Droplet deformation by short laser-induced pressure pulses," Journal of Fluid Mechanics **828**, 374–394 (2017).

[89]K. Sokolowski-Tinten, J. Bialkowski, A. Cavalleri, D. von der Linde, A. Oparin, J. Meyer-ter-Vehn, and S. I. Anisimov, "Transient States of Matter during Short Pulse Laser Ablation," Physical Review Letters **81**, 224–227 (1998).

[90]D. von der Linde and K. Sokolowski-Tinten, "The physical mechanisms of short-pulse laser ablation," Applied Surface Science **154-155**, 1–10 (2000).

[91]S. Amoruso, G. Ausanio, R. Bruzzese, L. Gragnaniello, L. Lanotte, M. Vitiello, and X. Wang, "Characterization of laser ablation of solid targets with near-infrared laser pulses of 100fs and 1ps duration," Applied Surface Science **252**, 4863–4870 (2006).

[92]O. Albert, S. Roger, Y. Glinec, J. Loulergue, J. Etchepare, C. Boulmer-Leborgne, J. Perrire, and E. Millon, "Time-resolved spectroscopy measurements of a titanium plasma induced by nanosecond and femtosecond lasers," Applied Physics A: Materials Science & Processing **76**, 319–323 (2003).

[93]K. R. Manes, V. C. Rupert, J. M. Auerbach, P. Lee, and J. E. Swain, "Polarization and Angular Dependence of 1.06-μm Laser-Light Absorption by Planar Plasmas," Physical Review Letters **39**, 281–284 (1977).

[94]R. Fedosejevs, R. Ottmann, R. Sigel, G. Kühnle, S. Szatmari, and F. P. Schäfer, "Absorption of femtosecond laser pulses in high-density plasma," Physical Review Letters **64**, 1250–1253 (1990).

[95]J. J. Monahan, "Smoothed particle hydrodynamics," Annu. Rev. Astron. Astrophys **30**, 543 (1992).

[96]P. J. Cossins, "Smoothed particle hydrodynamics," arXiv:1007.1245 (2010).

[97]S. I. Anisimov, B. L. Kapeliovich, and T. L. Perelman, "Electron emission from metal surfaces exposed to ultrashort laser pulses," Sov. Phys. JETP **39**, 375 (1974).

[98]H. Zhang, A. Antoncecchi, S. Edward, I. Setija, P. Planken, and S. Witte, "Unraveling phononic, optoacoustic, and mechanical properties of metals with light-driven hypersound," Phys. Rev. Applied **13**, 014010 (2020).

[99]K. Deguchi, K. Miyoshi, T. Ishii, and T. Matsuda, "Patterning Characteristics of a Chemically-Amplified Negative Resist in Synchrotron Radiation Lithography," Japanese Journal of Applied Physics **31**, 2954–2958 (1992).

[100]G. Dattoli, A. Doria, G. P. Gallerano, L. Giannessi, K. Hesch, H. O. Moser, P. L. Ottaviani, E. Pellegrin, R. Rossmanith, R. Steininger, V. Saile, and J. Wüst, "Extreme ultraviolet (EUV) sources for lithography based on synchrotron radiation," Nuclear Instruments and Methods in Physics Research Section A: Accelerators, Spectrometers, Detectors and Associated Equipment **474**, 259–272 (2001).

[101] Y. Socol, G. N. Kulipanov, A. N. Matveenko, O. A. Shevchenko, and N. A. Vinokurov, "Compact 13.5-nm free-electron laser for extreme ultraviolet lithography," Physical Review Special Topics - Accelerators and Beams **14**, 040702 (2011).

[102] E. R. Hosler, O. R. W. II, W. A. Barletta, P. J. S. Mangat, and M. E. Preil, "Considerations for a free-electron laser-based extreme-ultraviolet lithography program," Proc. SPIE **9422**, 94220D (2015).

[103] G. D. Kubiak, L. J. B. II, and K. D. Krenz, "High-power extreme-ultraviolet source based on gas jets," Proc. SPIEC **3331**, 81–89 (1998).

[104] R. H. Moyer, H. Shields, A. Martos, S. W. Fornaca, R. J. S. Pierre, and M. B. Petach, "Laser-produced plasma (LPP) scale-up and commercialization," Proc. SPIE **4343**, 249–254 (2001).

[105] H. Shields, S. W. Fornaca, M. B. Petach, M. Michaelian, R. D. McGregor, R. H. Moyer, and R. J. St. Pierre, "Xenon target performance characteristics for laser-produced plasma EUV sources," Proc. SPIE **4688**, 94 (2002).

[106] V. Banine and R. Moors, "Plasma sources for EUV lithography exposure tools," Journal of Physics D: Applied Physics **37**, 3207–3212 (2004).

[107] M. Yoshioka, Y. Teramoto, J. Jonkers, M. C. Schürmann, R. Apetz, V. Kilian, and M. Corthout, "Tin DPP source collector module (SoCoMo) ready for integration into Beta scanner," Proc. SPIE **7969**, 79691G (2011).

[108] A. Takahashi, D. Nakamura, K. Tamaru, T. Akiyama, and T. Okada, "Emission characteristics of debris from CO_2 and Nd:YAG laser-produced tin plasmas for extreme ultraviolet lithography light source," Applied Physics B **92**, 73–77 (2008).

[109] H. Mizoguchi, T. Abe, Y. Watanabe, T. Ishihara, T. Ohta, T. Hori, T. Yanagida, H. Nagano, T. Yabu, S. Nagai, G. Soumagne, A. Kurosu, K. M. Nowak, T. Suganuma, M. Moriya, K. Kakizaki, A. Sumitani, H. Kameda, H. Nakarai, and J. Fujimoto, "100W 1st generation laser-produced plasma light source system for HVM EUV lithography," Proc. SPIE **7969**, 796908 (2011).

[110] I. V. Fomenkov, A. I. Ershov, W. N. Partlo, D. W. Myers, D. Brown, R. L. Sandstrom, B. La Fontaine, A. N. Bykanov, G. O. Vaschenko, O. V. Khodykin, N. R. Böwering, P. Das, V. B. Fleurov, K. Zhang, S. N. Srivastava, I. Ahmad, C. Rajyaguru, S. De Dea, R. R. Hou, W. J. Dunstan, P. Baumgart, T. Ishihara, R. D. Simmons, R. N. Jacques, R. A. Bergstedt, and D. C. Brandt,

"Laser produced plasma light source for EUVL," Proc. SPIE **7969**, 796933 (2011).

[111]G. O'Sullivan and P. K. Carroll, "4d–4f emission resonances in laser-produced plasmas," Journal of the Optical Society of America **71**, 227 (1981).

[112]F. Torretti, A. Windberger, A. Ryabtsev, S. Dobrodey, H. Bekker, W. Ubachs, R. Hoekstra, E. V. Kahl, J. C. Berengut, J. R. C. López-Urrutia, and O. O. Versolato, "Optical spectroscopy of complex open-4d-shell ions Sn^{7+} - Sn^{10+}," Physical Review A **95**, 042503 (2017).

[113]T. Donnelly, T. Cummins, C. O' Gorman, B. Li, C. S. Harte, F. O'Reilly, E. Sokell, P. Dunne, and G. O'Sullivan, "Laser produced plasma for efficient extreme ultraviolet light sources," AIP Conference Proceedings, 155–160 (2012).

[114]S. Fujioka, M. Shimomura, Y. Shimada, S. Maeda, H. Sakaguchi, Y. Nakai, T. Aota, H. Nishimura, N. Ozaki, A. Sunahara, K. Nishihara, N. Miyanaga, Y. Izawa, and K. Mima, "Pure-tin microdroplets irradiated with double laser pulses for efficient and minimum-mass extreme-ultraviolet light source production," Applied Physics Letters **92**, 241502 (2008).

[115]D. Hudgins, N. Gambino, B. Rollinger, and R. Abhari, "Neutral cluster debris dynamics in droplet-based laser-produced plasma sources," Journal of Physics D: Applied Physics **49**, 185205 (2016).

[116]A. Y. Vinokhodov, K. N. Koshelev, V. M. Krivtsun, M. S. Krivokorytov, Y. V. Sidelnikov, V. V. Medvedev, V. O. Kompanets, A. A. Melnikov, and S. V. Chekalin, "Formation of a fine-dispersed liquid-metal target under the action of femto- and picosecond laser pulses for a laser-plasma radiation source in the extreme ultraviolet range," Quantum Electronics **46**, 23–28 (2016).

[117]J. Fujimoto, T. Hori, T. Yanagida, and H. Mizoguchi, "Development of Laser-Produced Tin Plasma-Based EUV Light Source Technology for HVM EUV Lithography," Physics Research International **2012**, 1–11 (2012).

[118]K. Tomita, Y. Sato, S. Tsukiyama, T. Eguchi, K. Uchino, K. Kouge, H. Tomuro, T. Yanagida, Y. Wada, M. Kunishima, G. Soumagne, T. Kodama, H. Mizoguchi, A. Sunahara, and K. Nishihara, "Time-resolved two-dimensional profiles of electron density and temperature of laser-produced tin plasmas for extreme-ultraviolet lithography light sources," Scientific Reports **7**, 12328 (2017).

[119]B. Verhoff, S. S. Harilal, and A. Hassanein, "Angular emission of ions and mass deposition from femtosecond and nanosecond laser-produced plasmas," Journal of Applied Physics **111**, 123304 (2012).

[120]Y. Tao, M. S. Tillack, S. S. Harilal, K. L. Sequoia, and F. Najmabadi, "Investigation of the interaction of a laser pulse with a preformed Gaussian Sn plume for an extreme ultraviolet lithography source," Journal of Applied Physics **101**, 023305 (2007).

[121]Y. P. Dou, C. K. Sun, C. Z. Liu, J. Gao, Z. Q. Hao, and J. Q. Lin, "Mitigation of energetic ion debris from Gd plasma using dual laser pulses and the combined effect with ambient gas," Chinese Physics B **23**, 075202 (2014).

[122]Z. Chen, X. Wang, D. Zuo, and J. Wang, "Investigation of ion characteristics in CO $_2$ laser irradiating preformed tin-droplet plasma," Laser and Particle Beams **34**, 552–561 (2016).

[123]M. J. Deuzeman, A. S. Stodolna, E. E. B. Leerssen, A. Antoncecchi, N. Spook, T. Kleijntjens, J. Versluis, S. Witte, K. S. E. Eikema, W. Ubachs, R. Hoekstra, and O. O. Versolato, "Ion distribution and ablation depth measurements of a fs-ps laser-irradiated solid tin target," Journal of Applied Physics **121**, 103301 (2017).

[124]A. V. Gurevich, L. V. Pariiskaya, and L. P. Pitaevskii, "Self-similar motion in rarefied plasma," Soviet Journal of Experimental and Theoretical Physics **42**, 449 (1966).

[125]D. B. Abramenko, M. V. Spiridonov, P. V. Krainov, V. M. Krivtsun, D. I. Astakhov, V. V. Medvedev, M. van Kampen, D. Smeets, and K. N. Koshelev, "Measurements of hydrogen gas stopping efficiency for tin ions from laser-produced plasma," Applied Physics Letters **112**, 164102 (2018).

[126]T. Higashiguchi, M. Kaku, M. Katto, and S. Kubodera, "Suppression of suprathermal ions from a colloidal microjet target containing SnO_2 nanoparticles by using double laser pulses," Applied Physics Letters **91**, 151503 (2007).

[127]J. F. Ziegler, "Stopping of energetic light ions in elemental matter," Journal of Applied Physics **85**, 1249–1272 (1999).

[128]L. Torrisi, F. Caridi, D. Margarone, and A. Borrielli, "Plasma–laser characterization by electrostatic mass quadrupole analyzer," Nuclear Instruments and Methods in Physics Research Section B: Beam Interactions with Materials and Atoms **266**, 308–315 (2008).

[129]L. Poirier, A. Bayerle, A. Lassise, F. Torretti, R. Schupp, L. Behnke, Y. Mostafa, W. Ubachs, O. O. Versolato, and R. Hoekstra, "Cross-calibration of a combined electrostatic and time-of-flight analyzer for energy- and charge-state-resolved spectrometry of tin laser-produced plasma," Applied Physics B **128**, 39 (2022).

[130]M. Murakami and M. M. Basko, "Self-similar expansion of finite-size non-quasi-neutral plasmas into vacuum: Relation to the problem of ion acceleration," Physics of Plasmas **13**, 012105 (2006).

[131]Z. Zhang, P. A. Van Rompay, and P. P. Pronko, "Ion characteristics of laser-produced plasma using a pair of collinear femtosecond laser pulses," Applied Physics Letters **83**, 431–433 (2003).

LIST OF PUBLICATIONS

Chapter 2
T. de Faria Pinto, J. Mathijssen, K. S. E. Eikema, and S. Witte, "Optical parametric chirped pulse amplifier producing ultrashort 10.5 mJ pulses at 1.55 µm," Optics Express 27, 29829 (2019).

Chapter 3
T. de Faria Pinto, J. Mathijssen, R. Meijer, H. Zhang, A. Bayerle, D. Kurilovich, O. O. Versolato, K. S. E. Eikema, and S. Witte, "Cylindrically and non-cylindrically symmetric expansion dynamics of tin microdroplets after ultrashort laser pulse impact," Applied Physics A 127, 93 (2021).

Chapter 4
A. S. Stodolna, T. de Faria Pinto, F. Ali, A. Bayerle, D. Kurilovich, J. Mathijssen, R. Hoekstra, O. O. Versolato, K. S. E. Eikema, and S. Witte, "Controlling ion kinetic energy distributions in laser produced plasma sources by means of a picosecond pulse pair," Journal of Applied Physics 124, 053303 (2018).

The author also contributed to the following publications:

[1] A. Bayerle, M. J. Deuzeman, S. v. d. Heijden, D. Kurilovich, T. de Faria Pinto, A. Stodolna, S. Witte, K. S. E. Eikema, W. Ubachs, R. Hoekstra, and O. O. Versolato, "Sn ion energy distributions of ns- and ps-laser produced plasmas," Plasma Sources Science and Technology **27**, 045001 (2018).

[2] D. Kurilovich, T. de Faria Pinto, F. Torretti, R. Schupp, J. Scheers, A. S. Stodolna, H. Gelderblom, K. S. Eikema, S. Witte, W. Ubachs, R. Hoekstra, and O. O. Versolato, "Expansion dynamics after laser-induced cavitation in liquid tin microdroplets," Phys. Rev. Appl. **10**, 054005 (2018).

Patent applications:
D. Kurilovich, O. O. Versolato, T. de Faria Pinto, S. Witte, "Radiation Source," ASML, Feb. 2018.

SUMMARY

To produce the increasingly more powerful computers that power our daily lives, smaller and smaller transistors need to be printed and crammed into ever more densely packed chips. A constant obstacle to this miniaturization trend and to the long life of Moore's law is the diffraction limit of light, which states that smaller features can only be printed using light with shorter wavelengths. Even as this fundamental limit is stretched to its extremes by clever engineering, the semiconductor industry has continuously pushed the technological envelope in search of light sources with shorter and shorter wavelengths, eventually reaching the current nanolithography machines which use extreme ultraviolet light (EUV), with a wavelength of 13.5 nm. Inside current commercial EUV sources, micrometer-sized droplets of liquid tin are irradiated by a high-power CO_2 laser, creating a plasma which emits the desired 13.5 nm photons. However, small dense liquid spheres are a rather inefficient target shape for EUV production. To solve this, each droplet is irradiated by two laser pulses. A first low-energy pre-pulse irradiates the initially-spherical droplet, deforming it via hydrodynamic expansion into a shape more favourable for EUV production. Afterwards, a time-delayed high-energy main pulse irradiates this deformed droplet. As the EUV generation efficiency is strongly dependent on the shape of the target, the process of deforming a spherical droplet into a more favorable shape is a topic of intense study.

Typically, pre-pulses have durations in the nanoseconds and effectively "push" the droplet to hydrodynamically deform from a sphere into a thin disk. Another approach that has been shown to produce promising targets is to irradiate the droplet with shorter pre-pulses with durations of picoseconds or even femtoseconds. Rather than pushing the droplet like nanosecond pulses, these shorter pulses create an intense shock wave on the droplet surface. This shock wave propagates through the spherical droplet and focuses at its center, where a bubble is formed through a process called cavitation. Once formed, this bubble rapidly expands, turning the droplet into a bubble, which later ruptures and breaks up into fine particles. These targets, sometimes referred to as "cloud" or "dome" targets, have in some cases shown higher conversion efficiencies

compared to disk targets, with the drawback of additional debris created by the violent transformation process.

To study the dynamics of these cloud targets, we designed and built a laser system capable of producing laser pulses with durations ranging from 220 fs to 100 ps, described in Chapter 2. The system can be broadly divided into two parts. The first is a 1064 nm-based system, seeded by a home-built Nd:YVO_4 oscillator whose output is passed through a tuneable stretcher which allows pulse durations between 15 and 100 ps. The stretched output then passes a pulse picking stage, which enables us to operate the system in single pulse mode or produce sequences of pulses with adjustable energy and pulse-to-pulse separation. This output is then amplified by a high-gain grazing-incidence Nd:YVO_4 pre-amplifier followed by a Nd:YAG rod amplifier, with a final output energy of up to 180 mJ. This system can be used as a standalone laser source, but it is also used to pump an optical parametric chirped pulse amplifier (OPCPA). The OPCPA is seeded by a commercial Erbium-doped fs fibre amplifier with a central wavelength of 1550 nm which is stretched to 30 ps and, after 3 amplification stages using non-linear KTA crystals and compression using transmission dielectric gratings, produces pulses with durations ranging from 220 fs to 10 ps, with energies up to 10.5 mJ.

In Chapter 3, using the OPCPA to irradiate microdroplets with initial radii of 15 μm and 23 μm, we study the effects of pulse energy and duration for pulse durations ranging from 220 fs to 10 ps, with energies ranging from 1 mJ to 5 mJ. The initial cavitation expansion velocity as well the velocity of the ablated material are found to decrease as a function of pulse durations, indicating how shorter pulses lead to faster, more violent dynamics. Additionally, using linearly polarized laser pulses, cylindrically-asymmetric shock waves were produced, leading to novel non-symmetric target shapes. A good qualitative agreement was obtained between smoothed-particle hydrodynamics simulations and high-resolution shadowgraphy images of the droplet deformation dynamics, highlighting the role of shock waves in the laser-driven deformation dynamics, and indicating that the non-cylindrically-symmetric pressure wave launched from the surface is the main factor for the observed behaviour.

In Chapter 4, we use the pulse picking capabilities of the 1064 nm amplifier to irradiate droplet targets with a pair of laser pulses, composed of a weaker first pulse with variable energy in the μJ range, followed by a more energetic 5 mJ pulse. In this configuration, we produced novel target shapes which were keenly dependent on the energy of the first pulse and the time delay between

the pulses. Furthermore, the addition of a small first pulse led to a significant reduction in the kinetic energy of the ions emitted by the plasma, with a 30-fold reduction in the most extreme case.

Chapter 5 introduces an electrostatic analyzer, which can measure the energy distribution of each detected charge state separately, offering additional insight on the processes that dictate the energy of the emitted ions. The typical picture assumes that ion acceleration driven solely by an electrostatic field created by electrons ejected by the laser pulse. This leads to a linear relation between the mean energy of each charge state and its ionization number, which we observe for laser energies of 1 mJ. However, for higher laser energies of 3 mJ and 5 mJ, we observe a nonlinear relation between mean ion kinetic energy and charge state, which hints at effects beyond the simple electrostatic acceleration model. Additionally, the energy spectra observed are largely independent of laser pulse duration in the range between 220 fs and 10 ps. This indicates that the timescales of ion acceleration in the observed regime are either shorter than 220 fs or longer than 10 ps.

Lastly, Chapter 6 builds upon all the previous work shown by using charge-state-resolved measurements to gain further understanding of the ion-slowing effects reported in Chapter 4. These new charge-resolved measurements show that the introduction of a weaker (tens-of-μJ) pulse preceding a second 5 mJ pulse results in a reduction of ion kinetic energy for every charge state, as well a strong reduction in the yield of higher-charge-state ions, which are the most energetic. Notably, for some pulse-pair settings, it was possible to completely suppress higher charge states above Sn^{2+}. This suppression of the faster ions is of practical interest to increase the lifetime of optical components inside EUV sources, especially when paired with ion mitigation techniques which are most effective for lower-energy ions below 1 keV.

ACKNOWLEDGMENTS

Now that this chapter in my life is coming to a conclusion (after a longer than anticipated time), I would like to start by thanking everyone at ARCNL for making my time in Amsterdam so memorable. ARCNL set a bar that will be very hard for any future workplace to beat, both in the quality of the science produced there and the people producing it, and I will forever look back to my 5 years in Amsterdam with incredible fondness.

I would also like to extend a special thank you to all the amazing people who helped and supported me during this project, starting with my supervisors Stefan Witte and Kjeld Eikema.

Stefan, thank you for your guidance and support throughout the years, and for pushing me across the finishing line to submit this thesis. You always encouraged your students to be independent and explore interesting data with a patient and positive attitude. Most notably for me with the pulse pair experiments, which started mysterious effect on some data sets but turned out to be some of the most interesting, albeit complex and enigmatic, results in this book.

Kjeld, your help during the lab setup was invaluable. I learned many laser tips and tricks (always accompanied by a tongue-in-cheek anecdote) that I still use today and I imagine I will be using and passing down to others for many years. Thank you for the advice in out and of the lab, which was instrumental in me *getting on with it*.

Jan, I'm really happy my grumpy supervision during your master's project didn't put you off continuing your studies at ARCNL, especially after seeing how much you improved the setup and hearing about the new experiments. Thank you for your friendship and your countless contributions to the OPA and the experiments we did together. None of it would have come together if it wasn't for your help.

Ale, I've never known someone more "work hard, play hard". I really admire how you always have a positive attitude, words of encouragement, and friendship to share with all those around you, even if you're having an awful week yourself. You always tried your hardest to drag me away from my video games and into social events and, looking back now, I regret not joining more often. Thank you for the life advice and in-flight emotional support.

Randy, sharing the lab with you was a pleasure. Glancing across the lab to see the results of your attention to detail and the excellent quality of your work was constant motivation for me to try my best. And while I'm still fond of quick and ugly prototypes followed by rapid iteration, I still often stop to think about how you would tackle a problem to balance my own approach. We shared many great moments over the years, from poorly timed country music in the lab, to a great stay in Boston, to sheer panic after being abandoned by someone who needed to work early the next day. But more than anything, it was great to have someone that shares my passion for complaining about anything and everything. And of course, I'll fondly remember our many *many* breaks spent sharing our complaints about Maisie over coffee.

Maisie, our friendship mostly composed of humorous bullying and annoyed eye rolling must have looked very dysfunctional to an external observer, but I've always cherished our ability to engage in the most animated discussions and always remain friends afterwards. Thank you for inviting to your home so many times to share in great company and great food. My apologies for regularly (and usually unintentionally) startling you in the lab. And of course, I'll fondly remember our many *many* breaks spent sharing our complaints about Randy over coffee.

Aneta, having started off my project in a big room with empty optical tables, I'm very grateful for your crash course on PhD project management. You showed me around AMOLF, introduced me to so many people that greatly contributed to our various experiments, helped me a great deal with the first beamtimes and especially with the pulse pair experiments, and taught me a lot on how to get things moving in general.

From complex machined parts to cardboard maquettes, none of the setups in the lab would have been practical or possible without the many contributions of Nik Noest, our brave group technician. Thank you for sharing so many of your quirky projects with us and always making sure your lab kids had all the kit they needed to stay safe and productive.

The EUV Plasma Processes group, as the plasma-half of laser-plasma interactions, were vital in the success of the work presented in this thesis. I kindly thank everyone in the group, but especially Oscar, Dmitry, and Lucas for many years of collaboration in the lab and the many scientific discussions over coffee. I would also like to thank Alex Bayerle for his friendship, tireless help with the ESA measurements, and for keeping lab morale high during long experiments

with unhealthy amounts of metal and 90s Japanese dance music. Your code is eXtremely sketchy, though...

I would also like to thank the AMOLF mechanical and electrical workshops staff for bringing many napkin drawings to life. And of course the software development group, in particular Marco Seynen, who made *Spanish Inquisition* possible, a very dubious endorsement without the proper context.

Sara, being away for nearly 5 years was the hardest part of this whole adventure. You were always there cheering me on when things went well and cheering me up when I felt discouraged or stressed. Thank you so much for your endless love and support, near and far.

Lastly, my most heartfelt thanks to my mom, who did a two-person job all by herself and gave me every opportunity to chase my passion for science and music, knowing this would likely lead me to move far away.

I would also like to thank Daisy, who wasn't helpful at all, but is an overall great cat.